1-1-2019

THREE-DIMENSIONAL (3D) IMAGE FORMATION AND RECONSTRUCTION FOR STRUCTURED ILLUMINATION MICROSCOPY USING A 3D TUNABLE PATTERN

Hasti Shabani

THREE-DIMENSIONAL (3D) IMAGE FORMATION AND RECONSTRUCTION FOR STRUCTURED ILLUMINATION MICROSCOPY USING A 3D TUNABLE PATTERN

by

Hasti Shabani

A Dissertation

Submitted in Partial Fulfillment of the

Requirement for the Degree of

Doctor of Philosophy

Major: Electrical and Computer Engineering

Supervisor: Dr. Chrysanthe Preza

The University of Memphis

February 2019

to my husband Siamak, to my son Samyar, and to my daughter Hannah

ACKNOWLEDGEMENT

First, I would like to thank Dr. Chrysanthe Preza, my PhD advisor, for her constant support, patience, motivation, enthusiasm and help during this doctoral accomplishment.

Also, I would like to thank Dr. Ana Doblas, my PhD committee member, for her constant help, useful discussions, and keeping me motivated during this doctoral accomplishment.

Additionally, I would like to thank Dr. Genaro Saavedra, professor in the department of Optics at University of Valencia, Spain, whose technical advice has helped me a lot to perform my research work.

I am grateful to Dr. Sharon V. King, Dr. Eddie Jacobs, and Dr. Omar Skalli who have devoted their precious time for being in my dissertation committee and for the valuable suggestions.

Finally, I would like to thank my former and current colleagues at the Computational Imaging Research Laboratory (CIRL) for their suggestions and inspiration during my research: Dr. Sreya Ghosh, Dr. Nurmohammed Patwary, Christopher A. Taylor, Anaya Dutta, Hanieh Shabanian, Jorge Sola Picabea, Sebastian Beyoda Lopez, and Bhuvaneshwari Bhaskaran.

PREFACE

This dissertation is written in the three-journal format. Chapters 2 and 3 are based on published papers: 1) H. Shabani, A. Doblas, G. Saavedra, E. Sanchez-Ortiga, and C. Preza, "Improvement of two-dimensional structured illumination microscopy with an incoherent illumination pattern of tunable frequency," Appl. Opt.57(7), B92–B101 (2018).; and 2) A. Doblas, H. Shabani, G. Saavedra, and C. Preza, "Tunable-frequency three-dimensional structured illumination microscopy with reduced data-acquisition," Opt. Express 26(23), 30476–30491 (2018), respectively. Chapter 4 is based on a paper in press, H. Shabani, A. Doblas, G. Saavedra, and C. Preza, "Optical transfer function engineering for a novel structured illumination microscope," Optics Letter (2019). Chapter 5 is based in part on a peer-reviewed conference paper, H. Shabani, S. Labouesse, A. Sentenac, and C. Preza, "Deconvolution based on axial-scanning model for three-dimensional structured illumination microscopy", IEEE 16th International Symposium on Biomedical Imaging (ISBI 2019), Venice, Italy, 2019 that has been accepted and some unpublished results.

This work was supported by the National Science Foundation (DBI award 1353904, PI: C. Preza) and the University of Memphis through the Herff Graduate Fellowship awarded to H. Shabani.

ABSTRACT

Shabani, Hasti. PhD. The University of Memphis. 02/2019. Three-dimensional (3D) image reconstruction for structured illumination microscopy using a 3D tunable pattern. Supervisor: Dr. Chrysanthe Preza.

Specific needs in live-cell microscopy necessitate moving fluorescence microscopy toward 3D imaging with enhanced spatial and temporal resolution. Exciting the sample by non-uniform illumination instead of uniform illumination is the main idea of developing techniques to address Abbe's diffraction limit in the conventional widefield fluorescence microscopy. In this dissertation, we characterized a novel tunable structured illumination microscopy (SIM) system using a Fresnel biprism illuminated by multiple linear incoherent sources (slits), in which the lateral and axial modulation frequencies of the 3D structured illumination (SI) pattern can be tuned separately. This is a unique feature, which is not the case of the conventional SIM systems. First, in order to take advantage of the tunable-frequency 2D-SIM system (using a single slit), we present a computational approach to reconstruct optical-sectioned images with super-resolution enhancement (OS-SR) by combining data from two lateral modulation frequencies. Moreover, a computational approach to reduce residual fringes evident in the restored images from the Fresnel biprism-based incoherent tunable SIM system is proposed. Second, the 3D SI pattern and the forward imaging model for the tunable-frequency 3D-SIM system (using multiple slits) are verified experimentally and two reconstruction methods have been used to evaluate the achieved OS and SR capabilities. Third, we presented the design of the 3D SI system used in a tunable 3D-SIM setup and discussed its performance in terms of synthetic optical transfer function (OTF). By designing the slit element, we can engineer the frequency

response of our 3D-SIM system to always operate at the highest OS and SR performance for a given imaging application. This is the first 3D-SIM setup that enables independent control of the achieved OS and SR capabilities. Finally, we proposed and implemented a new 3D iterative deconvolution approach based on a model that takes into account the axial scanning of the specimen during the data acquisition as in commercial microscopes. The method minimizes the mean squared error using the conjugate gradient descent optimization method. To our knowledge, such a restoration method has not been published to date.

TABLE OF CONTENT

LIST OF FIGURES

LSIT OF ABBREVIATION

LSIT OF MATHEMATICAL SYMBOLS

1. INTRODUCTION 1

1.1. Widefield Fluorescence Microscopy 1

1.1.1. Principle 1

1.1.2. Performance 4

1.2. Super-resolution Fluorescence Microscopy 8

1.3. Structured illumination Microscopy (SIM) 8

1.3.1. Two-dimensional SIM (2D-SIM) 11

1.3.2. Three-dimensional SIM (3D-SIM) 14

1.4. Contributions of the dissertation 20

1.5. Novelty of the work 23

2. 2D-SIM WITH AN INCOHERENT ILLUMINATION PATTERN OF TUNABLE FREQUENCY 26

2.1. Introduction 27

2.2. Tradeoffs in 2D-SIM performance 31

2.2.1. Background 31

2.2.2. Proposed computational approach 33

2.3. Incoherent tunable-frequency 2D-SIM based on Fresnel biprism 38

2.4. Experimental verification 44

2.4.1. Experimental setup 44

2.4.2. Experimental results 47

2.5. Conclusion 52

Funding 53

Acknowledgments 54

3. TUNABLE-FREQUENCY 3D-SIM WITH REDUCED DATA-ACQUISISTION 55

3.1. Introduction 56

3.2. Fundamentals of tunable-frequency 3D-SIM based on a Fresnel biprism . 58
3.2.1. Implementation of the tunable-frequency 3D-SIM system 58
3.2.2. Experimental validation of 3D structured illumination (SI) design 62
3.2.3. Experimental validation of 3D image formation 66
3.2.4. Data Processing 69
3.3. Proof-of-concept experimental results 75
3.4. Conclusion 82
Funding 83
Acknowledgement 84
4. OPTICAL TRANSFER FUNCTION ENGINEERING FOR A TUNABLE 3D STRUCTURED ILLUMINATION MICROSCOPE 85
Funding 99
5. THREE-DIMENSIONAL DECONVOLUTION BASED ON AXIAL-SCANNING MODEL FOR STRUCTURED ILLUMINATION MICROSCOPY 100
5.1. Forward imaging model 100
5.2. Current methods 104
5.3. Proposed deconvolution method 105
5.3.1. Proposed method with positivity constraint 108
5.4. Results 109
5.4.1. Criteria 110
5.4.2. Noiseless results 110
5.4.3. Noisy results 117
5.4.1. Data redundancy 122
5.5. Summary and Conclusion 131
6. CONCLUSION AND FUTURE DIRECTION 133
References and Links 137
Appendix A: Removing residual fringes in 2D-SIM 153
Appendix B: Details of noise investigation in synthetic OTF 160
Appendix C: Generalized Weiner filter approach in 3D-SIM 162
Appendix D: Mathematical derivation of cost function gradient and gradient decent step used in the proposed method 166

LIST OF FIGURES

Fig. 1. Jablonski diagram explanation to show fluorescence principle [2]. 2

Fig. 2. Basic widefield fluorescence microscope [https://ibidi.com/content/215-widefield-fluorescence]..... 4

Fig. 3. Widefield point spread function (PSF). (a) *xy*-section; (b) *xz*-section (c) lateral profile (d) axial profile. Lens: 63×/1.4 NA oil immersion objective lens; Emission wavelength of 515 nm..... 5

Fig. 4. Widefield optical transfer function (OTF): (a) *uv*-section; (b) *uw*-section. Lens: 63×/1.4 NA oil immersion objective lens; Emission wavelength of 515 nm. 7

Fig. 5. The SI pattern in 2D-SIM. Space representation: (a) *xy*-section and (b) *xz*-section (c). Frequency representation: *uv*-section; (d) *uw*-section..... 13

Fig. 6. The frequency support of the synthetic 2D-SIM OTF depends on the modulation frequency (u_m) of the SI pattern. *uv*-section and *uw*-section of the 3D synthetic OTF obtained from a SI pattern with: (a) $u_m = 0.5u_c$ and (b) $u_m = u_c$. Note that either the missing cone is completely filled providing OS (a) or the effective cutoff frequency is doubled providing SR (b). 14

Fig. 7. The SI pattern in 3W-SIM. Space representation: (a) *xy*-section and (b) *xz*-section (c). Frequency representation: *uv*-section; (d) *uw*-section..... 17

Fig. 8. The SI pattern in tunable 3D-SIM. Space representation: (a) *xy*-section and (b) *xz*-section (c). Frequency representation: *uv*-section; (d) *uw*-section..... 19

Fig. 9. The frequency support of the synthetic 2D-SIM OTF depends on the modulation frequency (u_m) of the SI pattern. *uw*-section of the 3D synthetic OTF obtained from Eq. (4) with M = 1 and a SI pattern with: (a) $u_m = 0.5u_c$ and (b) $u_m = u_c$. Note that either the missing cone is completely filled providing OS (a) or the effective cutoff frequency is doubled providing SR (b)..... 33

Fig. 10. Qualitative evaluation of the proposed method. Lateral view (top row), axial view (middle row) and zoomed view of the cropped square marked with a dashed pink line in the top left image (bottom row) of the 3D: (a) true object; (b) deconvolved widefield image using a Wiener filter; (c) reconstructed 2D-SIM image for $u_m = 0.5u_c = 2.7$ μm^{-1} (d) reconstructed 2D-SIM image for $u_m = 0.9u_c = 4.8$ μm^{-1}; (e) combined 2D-SIM reconstructed image with proposed method (Eqs. 5 & 6); and (f) reconstructed image from 3D-SIM raw data using the method in Ref. [14]. Scale bars: 1 μm (top and middle row) and 0.3 μm (bottom row). The cutoff frequency (u_c) is 5.4 μm^{-1} (the emission wavelength at λ = 515 nm and the imaging len's NA = 1.4). 35

Fig. 11. Quantitative comparison of the proposed method and 3W interference SIM using the results shown in Fig. 10. Normalized intensity profiles from the: (a) axial view; and (b) lateral view of cropped image along *x* axis. 37

Fig. 12. (a) Illustration of the tunable-frequency 2D-SIM using a Fresnel biprism, which is illuminated by the diffracted light emerging from an incoherent linear source. (b)

Tunable capability of our 2D SIM system. The lateral modulation frequency of the structured pattern (u_m) is changed by the axial displacement of the Fresnel biprism (η). Illustration for two modulation frequencies: half (top) or equal to (bottom) the cutoff frequency of the objective lens. 38

Fig. 13. Qualitative evaluation of the proposed envelope correction method to address the real SI pattern in tunable 2D-SIM based on the Fresnel biprism. (a) Real pattern generated by the biprism and the corresponding lower and upper envelope. Lateral view from the 3D: (b) forward image (top row) and reconstructed image (bottom row) with ideal sinusoidal pattern; (c) forward image with real pattern (top row) and its reconstruction with ideal sinusoidal pattern (bottom row); (d) reconstructed image after envelope correction applied to (c). (e) Quantitative comparison of images restored from ideal and real pattern SIM data assuming an ideal sinusoidal pattern, with and without envelope correction. 43

Fig. 14. Experimental verification of the frequency tunability capability of our SIM system. Fluorescent USAF target images acquired at four different axial positions of the Fresnel biprism in our open setup implementation. The cutoff frequency (u_c) is 1.9 μm^{-1} (the emission wavelength at λ = 515 nm and the imaging len's NA = 0.5). 45

Fig. 15. Achieved SR verified in experimental images of the fluorescent USAF target: (a) & (d) Widefield restoration; (b) & (e) Reconstructed SIM image for $u_m = 0.5u_c = 0.95$ μm^{-1} (OS); (c) & (f) Reconstructed SIM image for $u_m = 0.9u_c = 1.7$ μm^{-1} (SR); (g) Intensity profile through the horizontal elements of group 10 along the direction marked by the arrows in panel (d). Images in (d)-(f) are zoomed versions of the areas indicated by the yellow squares in images (a)-(c), correspondingly. The groups marked with the pink dashed line in (d)-(e) indicated the achieved resolution in each case. 48

Fig. 16. Simultaneous OS and SR achieved and verified with experimental images of a tilted fluorescent USAF target: (a) Reconstructed SIM image for $u_m = 0.5u_c = 0.95$ μm^{-1} (OS); (b) Reconstructed SIM image for $u_m = 0.9u_c = 1.7$ μm^{-1} (SR); (c) Reconstructed 2D-SIM image with proposed method (OS-SR combination). 49

Fig. 17. Experimental validation of improved optical sectioning achieved with our approach. Experimental images of a 6-μm spherical shells cluster from different systems: (a) Zeiss AxioImager.Z2 Widefield; (b) Zeiss ApoTome.2®; (c) our tunable 2D-SIM. The reconstructed images of panels (a) and (b) are obtained using the Zeiss ZEN.2 software. The arrows illustrated that our system has better optical-sectioning capability over ApoTome.2®. Lens: 20×/0.5 NA; Emission wavelength: 515 nm. 52

Fig. 18. Tunable-frequency 3D-SIM system based on a Fresnel biprism illuminated by a set of equidistant incoherent slits (N). (a) Illustration of the system. (b) 3D SI pattern with periodic visibility variation [Eq. (2)] created by the system in the sample space (z_{obj}). High-contrast fringes are located at a set of discrete axial planes. The 3D pattern exhibits a periodic axial contrast and its characteristics are controlled by three system parameters: N, x_0 and η. (c) Illustration demonstrating that improper imaging of the slits in the back focal-plane of the objective lens can lead to clipping of the slits and consequently, to a

reduction in the contrast of the fringes. z_{ill} refers to axial coordinates located after L1 lens. 60

Fig. 19. Experimental and numerical *xz*-section images of the 3D SI pattern generated using a different number of slits N. The lateral (u_m) modulation frequency for both numerical and experimental results is $\sim 0.8u_c$ and for $u_c = 1.9\ \mu m^{-1}$. The axial modulation frequency of the 3D SI pattern is $w_m = 0.0156u_m$. 63

Fig. 20. Numerical and experimental *xz*-section images of the 3D SI pattern generated using a different lateral modulation frequency (u_m). The axial modulation frequency of the 3D SI pattern is $w_m = 0.0156u_m$. The cutoff frequency of the system is $u_c = 1.9\ \mu m^{-1}$. The number of slits used was $N = 9$. For the experimental data we report the mean and the standard deviation of the measured axial extent of the fringes computed from 12 axial profiles through the maxima of four different resonant planes..... 65

Fig. 21. Evaluation of the experimental 3D-SIM system ($N = 9$ slits) through comparison of experimental and numerical [Eq. (3)] 3D forward images of a fluorescent uniform layer (Case 1) and a 6-μm spherical shell (Case 2). Case 1: *xy* and *xz* views of the numerical (a) and experimental (b) 3D image; normalized lateral (c) and axial (d) intensity profile through the center (marked by the red arrows) of the *xy* and *xz* sections in (a) and (b), respectively. The experimental lateral profile was obtained from the average of 6 central rows while the axial profile was obtained from the average of 16 axial profiles through the maxima. Intensity profiles were obtained after background subtraction followed by normalization. Case 2: *xy* and *xz* views of the numerical (e) and experimental (f) 3D image; lateral (g, h) and axial (i) intensity profiles obtained from the center (marked by the red arrows) of the *xy* and *xz* sections in (e) and (f), respectively. The cutoff frequency $u_c = 1.9\ \mu m^{-1}$. Lateral and axial modulation frequencies: $u_m = 0.44u_c = 0.85\ \mu m^{-1}$ and $w_m = 0.0135\ \mu m^{-1}$ for Case 1; and $u_m = 0.7u_c = 1.33\ \mu m^{-1}$ and $w_m = 0.021\ \mu m^{-1}$ for Case 2. 67

Fig. 22. Meridional section (*uw*) of the 3D synthetic MTF (absolute value of the synthetic OTF) for: (a) our 3D-SIM system with $N = 9$ slits; and (b) the conventional three-wave 3D-SIM system [14]. In both systems, we have considered the maximum lateral SR capability ($u_m = 0.8u_c$). Our synthetic OTF is composed of the 3 terms in Eq. (7). The pink and white dashed lines mark the compact support of the widefield and the 3D-SIM synthetic OTFs, respectively. The pink arrows highlight the extension of the lateral and axial cut-off frequencies achieved in both 3D-SIM synthetic OTFs. 71

Fig. 23. Qualitative and quantitative evaluation of the proposed 3D-SIM system performance using simulated data. Lateral view (top row), axial view (middle row) and zoomed view of the cropped square marked with a pink line in the top left image (bottom row) of the 3D: (a) true object; (b) reconstructed image from three-wave interference 3D SIM; (c) reconstructed image from our 3D-SIM system; (d) reconstructed 3D image with proposed 2D processing method. Lateral (e) and Axial (f) views of normalized intensity profiles. For both 3D-SIM systems, the lateral modulation frequency was set at $u_m = 0.8u_c = 4.35\ \mu m^{-1}$. 73

Fig. 24. Achieved OS capability verified with experimental images of an axially-thin fluorescent layer: *xz*-sections of the raw (a and d) and restored SIM image (b and c) from the tunable 3D-SIM ($u_m = 0.8u_c$) and the ApoTome-SIM ($u_m = 0.14u_c$) systems. Because ApoTome processing does not consider the widefield component, which is equivalent to the $\hat{D}_0(\cdot)$ component [Eq. (8)], we neglected this term when computing the restored image in the case of our system (b) for a fair comparison. In panels (a) and (d), the pink arrows indicate the axial extent of the SI pattern, quantified by the value shown on each image. The pink arrows in panels (b) and (c) quantify the FWHM of the integrated intensity, obtained by averaging the intensity values along its lateral coordinate for each restored image. 76

Fig. 25. Achieved SR verified in experimental images of the fluorescent USAF target: (a) Reconstructed SIM image for $u_m = 0.8u_c$ and (b) Synthetic deconvolved widefield image. (c) and (d) Normalized intensity profiles through the center of the vertical elements 10-2 and 10-6, marked by the dashed rectangles in (a) and (b), from both images..... 77

Fig. 26. Experimental raw images of a titled fluorescent USAF target at three different axial positions (z_i). Note that the fringes are visible only in the region of the FoV where the target is in-focus, marked by the pink double arrow in the zoomed versions of the areas marked by the yellow rectangles in the images shown on the left..... 79

Fig. 27. Experimental verification of simultaneous OS and SR achieved with our tunable 3D-SIM system by imaging a tilted fluorescent USAF target. *xy*-sections images obtained at three different axial locations of the target: (a) Synthetic raw widefield images; (b) Reconstructed SIM images from our systems using 2D processing (Sect. 3.2.4); (c) Reconstructed ApoTome-SIM images using the Zeiss ZEN.2 software. The corresponding magenta rectangles in (a) and (b) highlight the reduction of out-of-focus light achieved in the tunable 3D-SIM system image (b) compared to the conventional widefield image (a). The rectangles highlight different regions of the FoV in which in-focus information is not expected in each axial location of the tilted target. The yellow arrows indicate the lateral extent of the FoV reconstructed in the final image. The images in each case (a), (b) and (c) are displayed using a separate color scale. However, the group of three images in (a), (b), and (c), respectively, are displayed using a global minimum and maximum intensity mapped to the same color scale to show relative intensities in different axial planes. Lens: 20×/0.5 NA dry lens; Emission wavelength: 515 nm. Lateral modulation frequency: $u_m = 0.8u_c = 1.552$ μm^{-1} for the tunable 3D-SIM system and $u_m = 0.14u_c = 0.27$ μm^{-1} for the commercial ApoTome-SIM system. 80

Fig. 28. Verification of the lateral SR capability in the experimental image of the tilted fluorescent USAF target: (a) zoomed version of the groups 10 and 11 in the reconstructed SIM image obtained at the axial location z_2 in Fig. 27(b). (b) Normalized intensity profiles through the center of the vertical elements 10-4 and 10-5, marked by light blue and red dashed rectangles, along the horizontal direction. 81

Fig. 29. Relation of the SI design and synthetic OTF of the tunable-SIM system. (a) *xz*-section of 3D SI pattern and $|\mathcal{V}(z)|$ (blue curve) of Eq. (3). (b) Schematic of the slits-element image at the back focal plane of the objective lens. (c) *uw*-section of the 3D

pattern's FT. (d) *uw*-section of the synthetic MTF for $u_m = u_{c-eff} = 0.8u_c$. OTF compact support for WFM and tunable-SIM shown by black and white dashed lines, respectively. 90

Fig. 30. The impact of slits' parameters (N and x_0) on the synthetic OTF's compact support and OS capability of the tunable-SIM system. (a-c) *uw*-section of the synthetic MTF for different designs; (d) Integrated intensity profiles of (a-c), experimental (exp) and numerical (num) results. Legends: 'dem' and 'dec' stand for demodulation and deconvolution, respectively. For this study we used $u_m = u_{c-eff} = 0.8u_c$. 92

Fig. 31. Comparison of different systems' performance. (a-e) *uw*-section of the synthetic MTF for tunable-SIM and 3W-SIM systems at different designs. (f) Integrated intensity profiles obtained from the MTF of systems: (a)-(e); OS-SIM ($u_m = 0.5u_c$); confocal microscope; and WFM. (g) HWHM and σ_2 values computed from integrated intensity curve. 96

Fig. 32. Performance of two 3D-SIM systems under noisy conditions. *uw*-section of the synthetic MTF for tunable-SIM and 3W-SIM systems for (a-b) SNR = 20 dB and (c-d) SNR = 15 dB. Effective lateral (e) and axial (f) cutoff frequencies for different SNR levels. 98

Fig. 33. Forward images of 3W-SIM system based on two different imaging model: one that does not account for axial scanning of the sample [Eq. (1)] and one that does [Eq. (7)]. Lateral view (top row), axial view (middle row) of the 3D: (a) true object; forward image using (b) Eq. (1) , (c) Eq. (7). For the 3D-SIM system, the lateral modulation frequency was set at $u_m = 0.8u_c = 4.35\ \mu\text{m}^{-1}$ where $u_c = 5.44\ \mu\text{m}^{-1}$. Images are displayed using a different intensity scale mapped to the grayscale to facilitate visualization of details in each image. 103

Fig. 34. Qualitative and quantitative evaluation of the proposed model-based approach (3D-MB) for 3W-SIM using simulated noiseless data. Lateral view (top row), axial view (middle row) and zoomed view of the cropped square marked with a pink line in the top left image (bottom row) of the 3D: (a) true object; reconstructed image using (b) GWF, (c) proposed 3D-MB when the model matches, (d) proposed 3D-MB when the model does not match the data. Lateral (e) and axial (f) intensity profiles taken along the green dashed lines shown in the bottom and middle rows of (a-c), respectively. For the 3D-SIM system, the lateral modulation frequency was set at $u_m = 0.8u_c = 4.35\ \mu\text{m}^{-1}$ where $u_c = 5.44\ \mu\text{m}^{-1}$. The 3D-MB method results are shown after 400 iterations with the initial guess set equal to WF image provided by averaging 15 forward SIM images. The regularization parameter in the GWF method was empirically determined and it is equal to 10e-6. Negative values in the restored images were set to zero. Images are displayed using a different intensity scale mapped to the grayscale to facilitate visualization of details in each image. 113

Fig. 35. Qualitative and quantitative evaluation of the proposed model-based approach (3D-MB) for 3W-SIM and Tunable 3D-SIM using simulated noiseless data. Lateral view (top row), axial view (middle row) and zoomed view of the cropped square marked with a pink line in the top left image (bottom row) of the 3D: (a) true object; reconstructed image

for 3W-SIM system using (b) GWF, (c) 3D-MB; reconstructed image for Tunable 3D-SIM system using (d) GWF, (e) 3D-MB. Lateral (f) and axial (g) intensity profiles taken along the green dashed lines shown in the bottom and middle rows of (a-e), respectively. For the 3D-SIM system, the lateral modulation frequency was set at $u_m = 0.8u_c = 4.35\ \mu\text{m}^{-1}$ where $u_c = 5.44\ \mu\text{m}^{-1}$. The 3D-MB method results are shown after 400 iterations with the initial guess set equal to WF image provided by averaging the 9 forward images for tunable 3D-SIM and 15 forward images for 3W-SIM. The regularization parameter in the GWF method was empirically determined and it is equal to 10e-6 for (b) and (d), respectively. Negative values in the restored images were set to zero. Images are displayed using a different intensity scale mapped to the grayscale to facilitate visualization of details in each image. 115

Fig. 36. The effect of the number of iteration on the performance of the proposed model-based approach (3D-MB) for tunable 3D-SIM using simulated noiseless data. Lateral view (top row), axial view (middle row) and zoomed view of the cropped square marked with a pink line in the top left image (bottom row) of the 3D: (a) true object; reconstructed image for tunable 3D-SIM system using (b) 10 iterations, (c) 50 iterations, (d) 100 iterations, (e) 200 iterations, (f) 400 iterations. Quantitative comparison using MSE and SSIM (g). Monotonically decreasing cost function [Eq. (8)] (h). For the 3D-SIM system, the lateral modulation frequency was set at $u_m = 0.8u_c = 4.35\ \mu\text{m}^{-1}$ where $u_c = 5.44\ \mu\text{m}^{-1}$. The initial guess set equal to WF image provided by averaging 9 forward SIM images. Negative values in the restored images were set to zero. Images are displayed using a different intensity scale mapped to the grayscale to facilitate visualization of details in each image. 116

Fig. 37. Qualitative evaluation of the proposed model-based approach (3D-MB) applied to 3W-SIM and Tunable 3D-SIM using simulated noisy data. Lateral view (top row), axial view (middle row) and zoomed view of the cropped square marked with a pink line in the top left image (bottom row) of the 3D: (a) true object; (b) reconstructed image for tunable 3DSIM system for different SNR values with 3D-MB method; (c) reconstructed image for 3W-SIM system for different SNR values with 3D-MB method; (d) reconstructed image for tunable 3D-SIM system for different SNR values with GWF method; (e) reconstructed image for 3W-SIM system for different SNR values with GWF method. For both 3D-SIM system, the lateral modulation frequency was set at $u_m = 0.8u_c = 4.35\ \mu\text{m}^{-1}$. The 3D-MB method results are shown after 200 iterations with the initial guess set equal to WF image provided by averaging the 9 forward images for tunable 3D-SIM and 15 forward images for 3W-SIM. The regularization parameter in the GWF method was empirically determined and it is equal to 5e-3, 1e-2, 5e-2, and 9e-2, for 20dB, 15 dB, 10 dB, and 5 dB, respectively, for both (d) and (e). Images are displayed using a different intensity scale mapped to the grayscale to facilitate visualization of details in each image. 118

Fig. 38. Qualitative and quantitative evaluation of the proposed model-based approach (3D-MB) applied to 3W-SIM and tunable 3D-SIM using simulated noisy data (SNR = 10 dB). Lateral view (top row), axial view (middle row) and zoomed view of the cropped square marked with a pink line in the top left image (bottom row) of the 3D: (a) true object; (b) reconstructed image for tunable 3D-SIM system; (c) reconstructed image for 3W-SIM system. Effective (d) lateral and (e) axial cutoff frequencies for different SNR levels. The

lateral modulation frequency was set at $u_m = 0.8u_c = 4.35\ \mu\text{m}^{-1}$. The 3D-MB method results are shown after 200 iterations with the initial guess set equal to WF image provided by averaging the 9 and 15 forward images for tunable 3D-SIM and 3W-SIM systems, respectively. Images are displayed using a different intensity scale mapped to the grayscale to facilitate visualization of details in each image. 120

Fig. 39. Qualitative and quantitative evaluation of the proposed model-based (3D-MB) approach applied to 3W-SIM and tunable 3D-SIM using simulated noisy data (SNR = 5 dB). Lateral view (top row), axial view (middle row) and zoomed view of the cropped square marked with a pink line in the top left image (bottom row) of the 3D: (a) true object; (b) reconstructed image for tunable 3D-SIM system; (c) reconstructed image for 3W-SIM system. Effective (d) lateral and (e) axial cutoff frequencies of the two systems for different SNR levels. For both 3D-SIM systems, the lateral modulation frequency was set at $u_m = 0.5u_c = 2.72\ \mu\text{m}^{-1}$. The 3D-MB method results are shown after 100 iterations with the initial guess set equal to the WF image computed by averaging the 9 forward images in the case of the tunable 3D-SIM system and the15 forward images in the case of the 3W-SIM system. Images are displayed using a different intensity scale mapped to the grayscale to facilitate visualization of details in each image. 122

Fig. 40. Effect of data reduction (7 out of 15 raw 3W-SIM images used) and number of iterations used on the restoration obtained with the proposed model-based approach (3D-MB) for 3W-SIM using simulated noiseless data. Lateral view (top row), axial view (middle row) and zoomed view of the cropped square marked with a pink line in the top left image (bottom row) of the 3D: (a) true object; reconstructed image using 7 out of 15 raw 3W-SIM images with (b) 200 iterations, (c) 400 iterations, (d) 600 iterations, (e) 800 iterations, (f) 1000 iterations. Quantitative comparison using MSE and SSIM (g). Monotonically decreasing cost function [Eq. (8)] (h). The initial guess set equal to WF image provided by averaging 7 forward SIM images. Reconstructed image using 15 raw 3W-SIM images with 400 iterations (i) and corresponding MSE and SSIM (j). The initial guess set equal to WF image provided by averaging 15 forward SIM images. For the 3D-SIM system, the lateral modulation frequency was set at $u_m = 0.8u_c = 4.35\ \mu\text{m}^{-1}$ where $u_c = 5.44\ \mu\text{m}^{-1}$. Negative values in the restored images were set to zero. Images are displayed using a different intensity scale mapped to the grayscale to facilitate visualization of details in each image..... 123

Fig. 41. Effect of data reduction on the restoration obtained with the proposed model-based approach (3D-MB) for 3W-SIM using simulated noiseless data. Lateral view (top row), axial view (middle row) and zoomed view of the cropped square marked with a pink line in the top left image (bottom row) of the 3D: (a) true object; reconstructed image using (b) 15 out of 15 raw 3W-SIM images with 400 iterations, (c) 7 out of 15 raw 3W-SIM images with 1000 iterations, (d) 5 out of 15 raw 3W-SIM images with 1000 iterations, (e) 4 out of 15 raw 3W-SIM images with 1000 iterations and corresponding quantitative comparison using MSE and SSIM. The initial guess set equal to WF image provided by averaging the number of forward SIM images used. For the 3D-SIM system, the lateral modulation frequency was set at $u_m = 0.8u_c = 4.35\ \mu\text{m}^{-1}$ where $u_c = 5.44\ \mu\text{m}^{-1}$. Negative values in the restored images were set to zero. Images are displayed using a different

intensity scale mapped to the grayscale to facilitate visualization of details in each image. 125

Fig. 42. Effect of data reduction (7 out of 15 raw 3W-SIM images used) and number of iterations used on the restoration obtained with the proposed model-based approach (3D-MB) for 3W-SIM using simulated noisy data (SNR = 15dB). Lateral view (top row), axial view (middle row) and zoomed view of the cropped square marked with a pink line in the top left image (bottom row) of the 3D: (a) true object; reconstructed image using 7 out of 15 raw 3W-SIM images with (b) 100 iterations, (c) 200 iterations, (d) 300 iterations, (e) 400 iterations, (f) 500 iterations, (g) 600 iterations and corresponding quantitative comparison using MSE and SSIM. The initial guess set equal to WF image provided by averaging 7 forward SIM images. Reconstructed image using 15 raw 3W-SIM images with 200 iterations (h) and corresponding MSE and SSIM. The initial guess set equal to WF image provided by averaging 15 forward SIM images. For the 3D-SIM system, the lateral modulation frequency was set at $u_m = 0.8u_c = 4.35\ \mu\text{m}^{-1}$ where $u_c = 5.44\ \mu\text{m}^{-1}$. Negative values in the restored images were set to zero. Images are displayed using a different intensity scale mapped to the grayscale to facilitate visualization of details in each image. 126

Fig. 43. Effect of data reduction (5 out of 15 raw 3W-SIM images used) and number of iterations used on the restoration obtained with the proposed model-based approach (3D-MB) for 3W-SIM using simulated noisy data (SNR = 15dB). Lateral view (top row), axial view (middle row) and zoomed view of the cropped square marked with a pink line in the top left image (bottom row) of the 3D: (a) true object; reconstructed image using 5 out of 15 raw 3W-SIM images with (b) 100 iterations, (c) 200 iterations, (d) 300 iterations, (e) 400 iterations, (f) 500 iterations, (g) 600 iterations and corresponding quantitative comparison using MSE and SSIM. The initial guess set equal to WF image provided by averaging 5 forward SIM images. Reconstructed image using 15 raw 3W-SIM images with 200 iterations (h) and corresponding MSE and SSIM. The initial guess set equal to WF image provided by averaging 15 forward SIM images. For the 3D-SIM system, the lateral modulation frequency was set at $u_m = 0.8u_c = 4.35\ \mu\text{m}^{-1}$ where $u_c = 5.44\ \mu\text{m}^{-1}$. Negative values in the restored images were set to zero. Images are displayed using a different intensity scale mapped to the grayscale to facilitate visualization of details in each image. 127

Fig. 44. Effect of data reduction in the presence of noise (SNR = 15 dB) on the restoration obtained with the proposed model-based approach (3D-MB) for 3W-SIM. Lateral view (top row), axial view (middle row) and zoomed view of the cropped square marked with a pink line in the top left image (bottom row) of the 3D: (a) true object; reconstructed image using (b) 15 out of 15 raw 3W-SIM images with 400 iterations for noiseless case, (c) 15 out of 15 raw 3W-SIM images with 200 iterations for SNR = 15 dB case, (d) 7 out of 15 raw 3W-SIM images with 1000 iterations for noiseless case, (e) 7 out of 15 raw 3W-SIM images with 400 iterations for SNR = 15 dB case, (f) 5 out of 15 raw 3W-SIM images with 1000 iterations for noiseless case, (g) 5 out of 15 raw 3W-SIM images with 500 iterations for SNR = 15 dB case and corresponding quantitative comparison using MSE and SSIM. The initial guess set equal to WF image provided by averaging the number of forward SIM images used. For the 3D-SIM system, the lateral modulation frequency was set at

$u_m = 0.8u_c = 4.35\ \mu\text{m}^{-1}$ where $u_c = 5.44\ \mu\text{m}^{-1}$. Negative values in the restored images were set to zero. Images are displayed using a different intensity scale mapped to the grayscale to facilitate visualization of details in each image. 128

Fig. 45. Effect of data reduction and number of iterations used on the restoration obtained with the proposed model-based approach (3D-MB) using simulated noiseless data from a tunable 3D-SIM system. Lateral view (top row), axial view (middle row) and zoomed view of the cropped square marked with a pink line in the top left image (bottom row) of the 3D: (a) true object; reconstructed image using 4 out of 9 raw 3W-SIM images with (b) 200 iterations, (c) 400 iterations, (d) 600 iterations, (e) 800 iterations, (f) 1000 iterations. Quantitative comparison using MSE and SSIM (g). Monotonically decreasing cost function [Eq. (8)] (h). The initial guess set equal to WF image provided by averaging 4 forward SIM images. Reconstructed image using 15 raw 3W-SIM images with 400 iterations (i) and corresponding MSE and SSIM (j). The initial guess set equal to WF image provided by averaging 9 forward SIM images. For the 3D-SIM system, the lateral modulation frequency was set at $u_m = 0.8u_c = 4.35\ \mu\text{m}^{-1}$ where $u_c = 5.44\ \mu\text{m}^{-1}$. Negative values in the restored images were set to zero. Images are displayed using a different intensity scale mapped to the grayscale to facilitate visualization of details in each image. 129

Fig. 46. Effect of data reduction and number of iterations used on the restoration obtained with the proposed model-based approach (3D-MB) using simulated noiseless data from a tunable 3D-SIM system. Lateral view (top row), axial view (middle row) and zoomed view of the cropped square marked with a pink line in the top left image (bottom row) of the 3D: (a) true object; reconstructed image using (b) 4 out of 9 raw tunable 3D-SIM images with 1000 iterations, (c) 4 out of 9 raw 3W-SIM images with 2000 iterations, (d) 4 out of 9 raw 3W-SIM images with 4000 iterations, (e) 5 out of 9 raw 3W-SIM images with 1000 iterations, (f) 5 out of 9 raw 3W-SIM images with 2000 iterations, (g) 9 out of 9 raw 3W-SIM images with 400 iterations and corresponding quantitative comparison using MSE and SSIM. The initial guess set equal to WF image provided by averaging the number of forward SIM images used. For the 3D-SIM system, the lateral modulation frequency was set at $u_m = 0.8u_c = 4.35\ \mu\text{m}^{-1}$ where $u_c = 5.44\ \mu\text{m}^{-1}$. Negative values in the restored images were set to zero. Images are displayed using a different intensity scale mapped to the grayscale to facilitate visualization of details in each image. 131

Fig. 47. Illumination pattern generated by the Fresnel biprism for a modulation frequency equal to $u_m = 0.9u_c$: (a) pattern and the corresponding lower and upper envelopes in space domain (top panel), and pattern in the frequency domain compared with the ideal sinusoidal pattern (bottom panel), where the inset shows a zoomed version of the frequency content of the envelopes marked with the dashed rectangle. (b) Lateral profile of the function in Eq. (2); (c) lateral profile of the function in Eq. (3); (d) and (e) Evaluations of Eq. (1) with and without the third term, respectively. The cutoff frequency (u_c) is 5.4 μm^{-1} with the emission wavelength at λ = 515 nm and the imaging lens' numerical aperture (NA) equal to 1.4. 154

Fig. 48. Block diagram describing the envelope correction method proposed to reduce the residual fringes in tunable SIM based on the Fresnel biprism. 156

Fig. 49. Qualitative evaluation of the proposed envelope correction method to address the real SI pattern in tunable 2D-SIM based on the Fresnel biprism for simulated object (6-μm spherical bead). Lateral view from the 3D: (a) forward image (top row) and reconstructed image (bottom row) with ideal sinusoidal pattern; (b) forward image with real pattern (top row) and its reconstruction with ideal sinusoidal pattern (bottom row); (c) reconstructed image after envelope correction applied to (b). (d) Quantitative comparison of images restored from ideal and real pattern SIM data assuming an ideal sinusoidal pattern, with and without envelope correction. 157

Fig. 50. Qualitative evaluation of the proposed envelope correction method to address the real SI pattern in tunable 2D-SIM based on the Fresnel biprism for the experimental data of a pollen grain for two different modulation frequencies: $u_m = 0.1u_c$ (top row) and $u_m = 0.3u_c$ (bottom row). (a) Raw experimental images with the real SI pattern. Reconstructed images: (b) before envelope correction; (c) after applying the first step of the proposed approach for the envelope correction to (b); (d) after applying the first and second steps of the proposed approach for the envelope correction to (b). 158

Fig. 51. Zeroth order moment of two 3D-SIM systems under noisy conditions. 161

LIST OF ABBREVIATION

2D: Two Dimensional

3D: Three Dimensional

3W-SIM: Three-Wave Interference 3D-SIM

a. u.: arbitrary unit

bf: best focus

CCD: Charged Coupled Device

CGD: Conjugate Gradient Descent

CIRL: Computational Imaging Research Laboratory

DoF: Depth of Field

FT: Fourier Transform

FWHM: Full Width at Half Max

GWF: Generalized Wiener Filter

HWHM: Half Width at Half Max

NA: Numerical Aperture

MSE: Mean Squared Error

OS: Optical Sectioning

OSA: Optical Society of America

OTF: Optical Transfer Function

PALM: Photo Activated and Localization Microscopy

PSF: Point Spread Function

RI: Refractive Index

RLS: Regularized Least Squares

ROI: Region of Interest

SA: Spherical Aberration

SIM: Structured Illumination Microscopy

SLM: Spatial Light Modulator

SNR: Signal to Noise Ratio

SSIM: Structural Similarity Index Measure

STED: Stimulated Emission Depletion

STORM: Stochastic Optical Reconstruction Microscopy

WF: widefield

LIST OF MATHEMATICAL SYMBOLS

d_{xy} : Resolution limit in the *xy*-plane

λ : Excitation wavelength

θ_a : The half of the aperture angle of the objective

n_i : The refractive index of the lens' immersion medium

d_z : Resolution limit in the *z*-plane

u_c : Lateral cutoff frequency

w_c : Lateral cutoff frequency

u_m : Lateral modulation frequency

w_m : Lateral modulation frequency

(x, y, z) : Lateral and axial space coordinate

(u, v, w) : Lateral and axial spatial frequency coordinate

$i(\boldsymbol{x}, z)$: Intensity of a 3D SI pattern in the space domain

$I(\boldsymbol{u}, w)$: Intensity of a 3D SI pattern in the spatial frequency domain

φ : Phase of the SI pattern

θ : Angle (orientation) of the SI pattern

N : Number of slits

x_0 : Distance between two neighboring slits

η : biprism position

δ : Refringence angle of the Fresnel biprism

$h(\boldsymbol{x}, z)$: 3D WF PSF in the space domain

$H(\boldsymbol{u}, w)$: 3D WF OTF in the spatial frequency domain

$h_{SIM}(\boldsymbol{x}, z)$: 3D synthetic SIM PSF in the space domain

$H_{SIM}(\boldsymbol{u}, w)$: 3D synthetic SIM OTF in the spatial frequency domain

$\mathcal{V}(z)$: Visibility function of tunable 3D SI pattern in the space domain

$V(w)$: Visibility function of tunable 3D SI pattern in the spatial frequency domain

$o(\boldsymbol{x}, z)$: 3D distribution emitted from the object in the space domain

$g(\boldsymbol{x}, z)$: 3D forward (observed/recorded) image in the space domain

$j_k(\boldsymbol{x})$: k^{th} lateral function of a 3D SI pattern in the space domain

$J_k(\boldsymbol{u})$: k^{th} lateral function of a 3D SI pattern in the spatial frequency domain

$i_k(z)$: k^{th} axial function of a 3D SI pattern in the space domain

$I_k(w)$: k^{th} axial function of a 3D SI pattern in the spatial frequency domain

1. INTRODUCTION

To observe objects smaller than 100 µm, which cannot be seen with naked eyes, we use either the optical or the electron microscope. In conventional widefield (WF) microscopy, the spatial resolution is fundamentally limited by the diffraction of the light known as Abbe's diffraction limit to about 200 nm in the lateral direction and about 400 nm in the axial direction [1]. Although electron microscopy can be used to observe nano-particles, it cannot be used for live cell imaging as the high energy electron beam will damage the sample. Moreover, for 3D volumetric imaging, the sample needs to be physically sliced in the case of electron microscopy, which restricts its use for in-vivo imaging. However, light microscopy is inherently non-invasive and the sample can be optically sliced for volumetric imaging without physically slicing it; that's why light microscopy plays an invaluable role in the investigation of 3D cellular interactions between living organisms.

1.1. Widefield Fluorescence Microscopy

1.1.1. Principle

Fluorescence microscopy is a special form of light microscopy. It uses fluorescence to mark structures in fixed and living biological specimens instead of using absorption, phase or interference effects, which allows investigating cellular structures and micro-organisms in three dimensions under non-invasive conditions. Fluorescence is a phenomenon that involves absorbance and emission of a small range of the light wavelengths by a fluorescent

molecule known as a fluorophore. When the sample labeled with fluorophores is illuminated with an appropriate light, the fluorophores absorb light and re-emit it at a longer wavelength. The fluorescence process can be explained using a simple Jablonski diagram [2] as shown in Fig. 1. When fluorophore labeled proteins are excited with enough energy they absorb the energy and transit to the excited electronic state. The molecules in the excited state then relax either to the lower excited state or to the ground state. Fluorescence is the process, which occurs when the excited molecules emit light in nanoseconds of time at the longer wavelength during relaxation to the ground state. Some of the molecules also non-radioactively relax to the lowest excited state, which is known as the internal conversion. Different tissue components can be stained with different fluorescent molecule that emits visible light, when excited with different wavelengths. This provides specificity and enables multi-spectral imaging, which provides information from different sample proteins/structures.

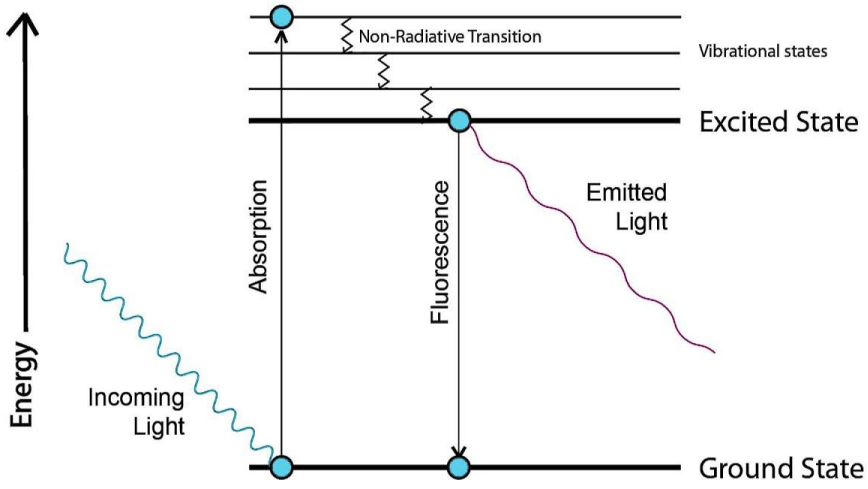

Fig. 1. Jablonski diagram explanation to show fluorescence principle [2].

The invention of green fluorescent protein (GFP) was a huge contribution that resulted in the Nobel Prize in chemistry awarded in 2008 to Japanese scientist, Osamu Shimomura, and two American scientists, Martin Chalfie and Robert Y. Tsien [3]. In addition to GFP, a large number of different dyes are available ranging from UV to near infrared region. The introduction of varieties of specific markers has brought about unprecedented advances in biological applications of fluorescence microscopy. The fluorophores, however, need special precautions in preparation and usage. They have limited stability and they bleach with excessive illumination and produce chemical photo-toxicity.

The schematic diagram of an epi-illumination fluorescence microscope is shown in Fig. 2, where the sample is illuminated from the top (upright configuration) using the microscope objective lens. In a standard fluorescence microscope, the sample is illuminated by a homogeneous (e.g. uniform) light at the excitation wavelength. Excitation light generated from a signal generator (i.e. mercury arc lamp or LED) is passed through an excitation filter, which allows the light with a specific wavelength to pass. A dichroic mirror, which is positioned at 45° angle reflects photons at the excitation wavelength but allows the fluorescence light to pass through. The remaining excitation light is filtered out by the emission filter so that only the fluorescence intensity is captured by the camera. The emitted fluorescence intensity is proportional to the excitation intensity. The light emitted by each fluorophore passes first through the objective lens and then dichroic mirror. Finally, the emitted light (which is incoherent) is collected by a detector (commonly a CCD camera) placed at the image plane, meaning that intensity adds up on the detector. The CCD camera detects the emitted wavefront intensity, which represents the image of the

specimen. The image detected by the CCD camera is stored in the computer's memory for visualization and further processing.

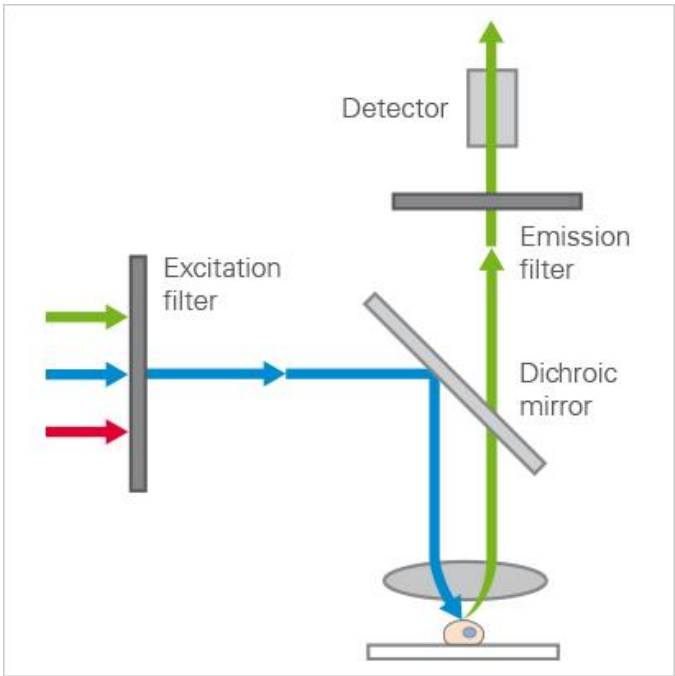

Fig. 2. Basic widefield fluorescence microscope [https://ibidi.com/content/215-widefield-fluorescence].

1.1.2. Performance

Due to the linearity of the microscope image formation and the incoherence of the fluorophores, the intensity recorded by the camera can be modeled as the convolution of the fluorescence distribution with a point spread function (PSF) which corresponds to the image of a point light source. Fig. 3(a) and (b) show respectively the *xy*-section and *xz*-section of the unaberrated PSF of a 63×/1.4 NA oil immersion objective lens, where the RI of the immersion medium is 1.515, and the emission wavelength is 515 nm.

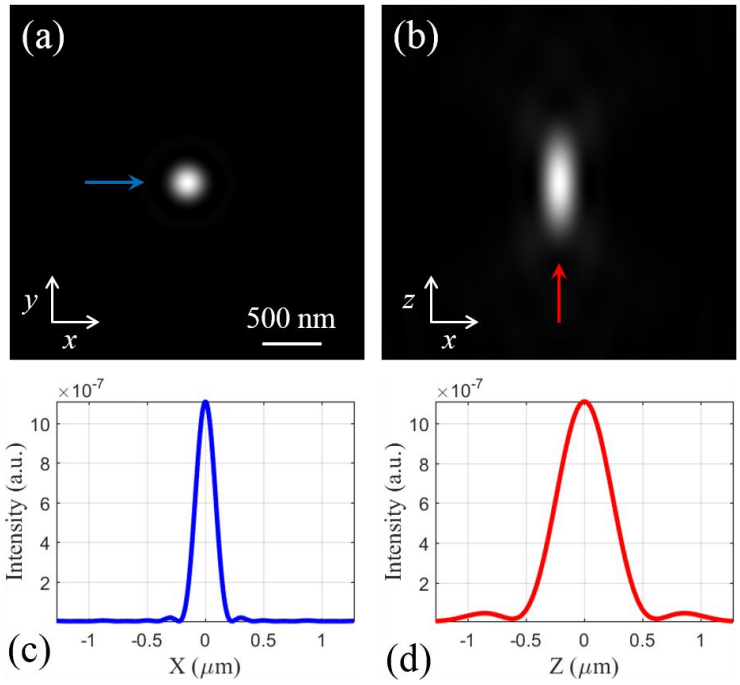

Fig. 3. Widefield point spread function (PSF). (a) *xy*-section; (b) *xz*-section (c) lateral profile (d) axial profile. Lens: 63×/1.4 NA oil immersion objective lens; Emission wavelength of 515 nm.

In term of the lateral resolution, the radius of the diffraction Airy disk in the image plane is defined by the following [1]:

$$d_{xy} = 0.61\frac{\lambda}{n_i \sin(\theta_a)} = 0.61\frac{\lambda}{\mathrm{NA}}, \tag{1}$$

where θ_a is the half of the aperture angle of the objective, n_i is the refractive index of the lens' immersion medium, λ is the emission wavelength and NA is the numerical aperture of the objective lens. The resolution along the optical axis, *z*, is determined in a similar way using the width of the diffraction in the *z*-axis [the PSF along the optical axis, Fig. 3(d)] commonly estimated using the full width half maximum (FWHM) given by [1]:

$$d_z = \frac{n_i \lambda}{\mathrm{NA}^2}. \quad (2)$$

High numerical apertures shrink the depth-of-field (DoF) and dramatically improve the axial resolution. It is worth mentioning here that increasing the refractive index of the immersion medium of the objective lens does not improve the axial resolution. This is because the numerical aperture is also dependent on the same refractive index.

Therefore, the resolution of the conventional imaging system varies between 160 nm to 270 nm depending on the objective lens and the wavelength of light emitted from the sample. In the unaberrated PSF of a 63x/1.4 NA oil immersion objective lens shown in Fig. 3 for $\lambda = 515$ nm, the lateral (d_{xy}) and axial (d_z) resolution limits are 224 nm and 398 nm, respectively. In fluorescence microscopy, improving the resolution and the contrast of images is a strong challenge. Resolution and contrast are inseparable concepts as low contrast usually deteriorates the ability to distinguish two point objects, a metric often used to quantify resolution. Contrast is the difference between the brightness of various details in the object, and the difference as compared with the background. Resolution is the finest detail actually visible in the image.

Another way of determining the resolution is based on the accessible sample spatial frequencies in the Fourier space. The spatial frequency support of the conventional WF fluorescence microscopy is limited by the optical transfer function (OTF), which is the Fourier transform of the point spread function of the microscope. The three-dimensional OTF of the conventional microscope is a torus-like region, as shown in Fig. 4(b). Fig. 4(a) and (b) show the 2D cross-sections of the OTF's compact support. The low-resolution

information resides close to the origin (low frequencies), while higher resolution information resides further away at high frequencies. The origin of the torus has a "hole" which is the missing cone of frequencies. The maximum sample spatial frequency accessible in the conventional WF microscope image is therefore limited by the compact support of the OTF, which is expressed by the lateral cutoff frequency (u_c) and the axial cutoff frequency (w_c) given below [1]:

$$u_c = \frac{2\mathrm{NA}}{\lambda}, \qquad w_c = \frac{\mathrm{NA}^2}{n_i \lambda}. \tag{3}$$

This means a conventional microscope transfers the sample's frequencies that reside within the OTF's compact support.

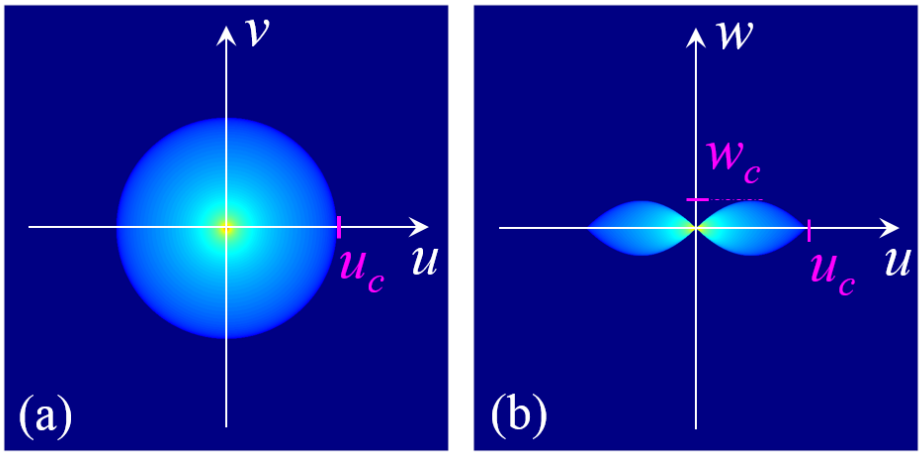

Fig. 4. Widefield optical transfer function (OTF): (a) *uv*-section; (b) *uw*-section. Lens: 63×/1.4 NA oil immersion objective lens; Emission wavelength of 515 nm.

1.2. Super-resolution Fluorescence Microscopy

The conventional standard WF fluorescence microscope enables to achieve a spatial resolution of 200 nm lateral and 400 nm axial. A microscopic technique that improves the resolution by at least a factor of 2 is classified as a super-resolution technique [4]. Recently many super-resolution fluorescence microscopy techniques have been developed, which vary in their principle, application, and implementation such as: photo activated and localization microscopy (PALM) [5], 4pi [6,7], stochastic optical reconstruction microscopy (STORM) [8], stimulated emission depletion (STED) [9], and structured illumination microscopy (SIM) [10–16]. In addition to these super-resolution microscopy modalities, which improve the lateral (and possibly axial) resolution beyond the diffraction limit, there are several other techniques that improve axial resolution (also known as optical sectioning) such as confocal microscopy [17] and light sheet microscopy techniques. Among these techniques, all of which extend the frequency support of the optical transfer function (OTF) of a conventional WF microscope, structured illumination microscopy (SIM) is an attractive method for a broad range of studies in cell biology as it offers high photon efficiency, potentially high imaging rates, relatively low hardware requirements, and compatibility with most dyes and fluorescent proteins [14].

1.3. Structured illumination Microscopy (SIM)

In SIM, the sample is illuminated by a sinusoidal patterned light, which modulates the fluorescence intensity emitted by the sample. The modulation process brings the out-of-band frequency content into the microscope objective passband; and the modulated information can be reassigned computationally to the correct locations of the object

spectrum, which results in the high resolution images. The introduction of structured illumination (SI) in fluorescence microscopy to improve resolution and optical sectioning goes back to the late 1990s. The first SIM approach proposed by Neil and Wilson [10,18], in which the illumination is incoherent, is based on the generation of the SI pattern via projecting single spatial frequency grid pattern onto the sample plane. It means that the SI pattern is imaged on the sample space, therefore only the in-focus section of the plane is modulated. Thanks to this axial confinement of the SI pattern, this SIM system has optical sectioning (OS) capability, contrary to WF fluorescence microscope. However, it is not possible to achieve the highest modulation frequency since the contrast of the fringes for this frequency is significantly attenuated. This happens due to fact that the SI pattern are doubly penalized by the incoherent OTF (illumination and detection OTFs). This limits the capability of incoherent illumination SIM from obtaining super-resolution image, and this type of SIM can only be used for OS. Images were taken at three spatial positions of the grid and processed to produce optically sectioned images that are substantially similar to those obtained with confocal microscopes. The theoretical analysis of the image formation in structured illumination microscopy and demonstration that the transfer function behavior is comparable to the confocal instrument can be found in [19].

The second SIM approach was developed to enhance the resolution by using coherent illumination. In 1999, R. Heintzmann and C. Cremer introduced a simple method of generating laterally modulated illumination using a diffraction grating [20]. The full capability of the technique for doubling the lateral resolution is demonstrated by Gustafsson [12] by illuminating the sample using a sinusoidal pattern created by the interference of two light beams emerging from a diffraction grating (2D-SIM). This

technique helps to maintain the contrast of the SI pattern projected onto the sample even in the case of modulation frequency (u_m) is close to the cutoff frequency (u_c) of the microscope objective lens. Therefore, it is possible to obtain super-resolution (SR) in the case of coherent illumination SIM, and the optical resolution becomes double compared to the Abbe resolution limit when $u_m = u_c$, the cutoff frequency of the WF. However, to obtain the best possible optical sectioning (OS) capability (by filling the frequency information in the WF OTF's missing-cone), the modulation frequency, u_m, needs to be half of the cutoff frequency, u_c, which limits the resolution improvement to 1.5 times. Therefore, to have the best OS and SR simultaneously, multiple images need to be captured both at $u_m = u_c$, and $u_m = 0.5u_c$ [15,21].

With this implementation (2D-SIM), there is a tradeoff between OS and SR capabilities. To overcome this tradeoff, the SIM method was modified and developed for doubling three-dimensional resolution (3D-SIM). Gustafsson *et al.* [14] proposed illuminating the fluorescent sample with three mutually coherent beams from a diffraction grating and therefore the structured pattern varied in both the lateral and axial directions. The second approach to generate the 3D tunable-frequency SI pattern is based on a Fresnel biprism illuminated by multiple linear sources (slits) [16,22].

Since SIM is based on a computational sensing paradigm, computational methods are an integral part of the imaging system modification and have a direct impact on the improved performance. There are two main computational approaches in solving the inverse imaging problem in SIM. The first approach is based on a set of steps involving demodulation using a matrix inversion followed by deconvolution using a non-iterative

generalized Wiener filter [14,16,20].The detail of this approach for 3D-SIM is in Appendix C. Because of its simplicity and speed, this direct method is currently the most used in practice, especially on commercial systems. The second approach is non-direct, iterative model-based optimization algorithms that have the potential to significantly improve the reconstruction quality and robustness of direct approach, which are discussed in detail in Chapter 5.

1.3.1. Two-dimensional SIM (2D-SIM)

In two-dimensional structured illumination microscopy (2D-SIM), the SI pattern varies only laterally and it is usually created by interfering two coherent plane waves at the sample plane using either a diffraction grating [12] or a Fresnel biprism and a single slit [15] The intensity of the 3D SI pattern can be derived by the time average of the modulus squared of the total complex amplitude of the two beams (by illuminating coherently a diffraction grating and blocking orders except the ±1 terms) [14]:

$$i(\boldsymbol{x},z)=\left\langle\left|\sum_{j=1}^{2}E_j\left(\boldsymbol{x},z,t\right)\right|^2\right\rangle=\left|\sum_{j=1}^{2}E_j\left(\boldsymbol{x},z\right)\right|^2, \tag{4}$$

where, $\boldsymbol{x}=(x,y)$ and z denote the lateral and axial coordinates and E_j is the complex amplitude of each beam (plane wave) and the two beams can be assumed to have equal amplitude distributions given by $E_j\left(\boldsymbol{x},z\right)=E_0\exp\left[i\frac{2\pi}{\lambda}(\boldsymbol{x}\sin\beta,z\cos\beta)\right]$, where β is the angle between each beam direction and the optic axis. Therefore, the 3D SI pattern in two-wave interference SIM is expressed by [14]:

$$
\begin{aligned}
i(\boldsymbol{x},z) &= \left(E_1+E_2\right)\left(E_1+E_2\right)^* \\
&= 2E_0\left[1+\cos\left(\frac{2\pi}{\lambda}\boldsymbol{x}(\sin\beta_1-\sin\beta_2)+\frac{2\pi}{\lambda}z(\cos\beta_1-\cos\beta_2)\right)\right]
\end{aligned} \tag{5}
$$

where $\beta_1=\beta$ and $\beta_2=-\beta$. Therefore,

$$
i(\boldsymbol{x},z)=2E_0\left[1+\cos\left(2\pi u_m\boldsymbol{x}\right)\right] \tag{6}
$$

where $u_m=\frac{2\sin\beta}{\lambda}$ is the lateral modulation frequency. In a generalized form, we can rewrite Eq. (6) as follows:

$$
i(\boldsymbol{x},z)=1+\cos\left[2\pi u_m\left(\cos\theta x+\sin\theta y\right)+\varphi\right] \tag{7}
$$

where φ is the phase of the pattern and θ defines the orientation of the SI pattern with respect to the *x* axis. As it is clear from Eq. (7), there is no axial variation in 2D-SIM [see Fig. 5(b)]. Assuming $\varphi=0,\ \theta=0$ for simplicity (without loss of generality) and taking the Fourier transform (FT) of Eq. (7) results in Eq. (8) below, which shows that the SI pattern of 2D-SIM system has three unique delta functions:

$$
I(\boldsymbol{u},w)=\delta(\boldsymbol{u},w)+\frac{1}{2}\delta(u-u_m,v,w)+\frac{1}{2}\delta(u+u_m,v,w) \tag{8}
$$

where, $\boldsymbol{u}=\left(u,v\right)$ and w denotes the lateral and axial spatial frequency coordinates. Fig. 5(c) and (d) shows the frequency representation of the SI pattern in 2D-SIM, which confirms that there is only lateral modulation.

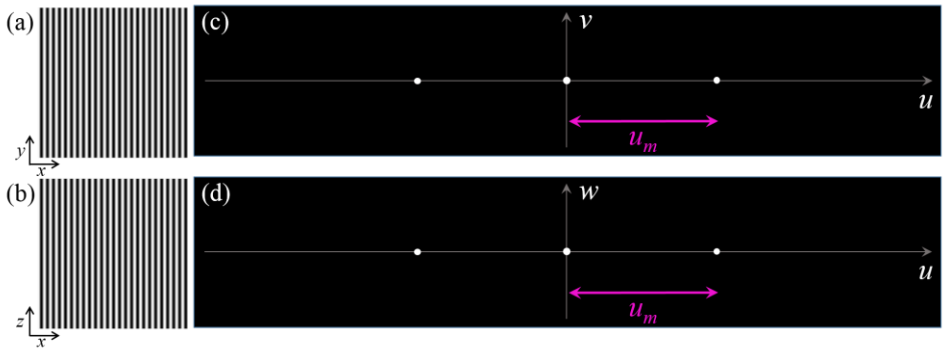

Fig. 5. The SI pattern in 2D-SIM. Space representation: (a) *xy*-section and (b) *xz*-section (c). Frequency representation: *uv*-section; (d) *uw*-section.

Similar to the conventional WF system, it is more illustrative to analyze the SIM imaging process in the spatial frequency domain. The 2D-SIM system is characterized by a synthetic OTF function, $H_{2D-SIM}(\boldsymbol{u}, w)$, expressed as follows [15,23]:

$$H_{2D-SIM}(\boldsymbol{u}, w) = H(\boldsymbol{u}, w) + \frac{1}{2} H(u - u_m, v, w) + \frac{1}{2} H(u + u_m, v, w) \tag{9}$$

where $H(\boldsymbol{u}, w)$ is the conventional WF OTF. Fig. 6 shows the synthetic OTF of the 2D-SIM system for two different modulation frequencies ($u_m = 0.5u_c$ and $u_m = u_c$, where u_c is the cutoff frequency of the imaging system). From this figure, it is clear that there is a tradeoff between the OS and SR capabilities of the 2D-SIM system depending on the lateral modulation frequency. The best OS capability by filling the missing cone [Fig. 6(a)] does not have double lateral resolution, and the highest improvement of lateral resolution [Fig. 6(b)] is not accompanied by any improvement of the OS capability. Therefore, the conventional 2D-SIM systems are not able to provide simultaneously the highest improvement in lateral resolution and optical-sectioning.

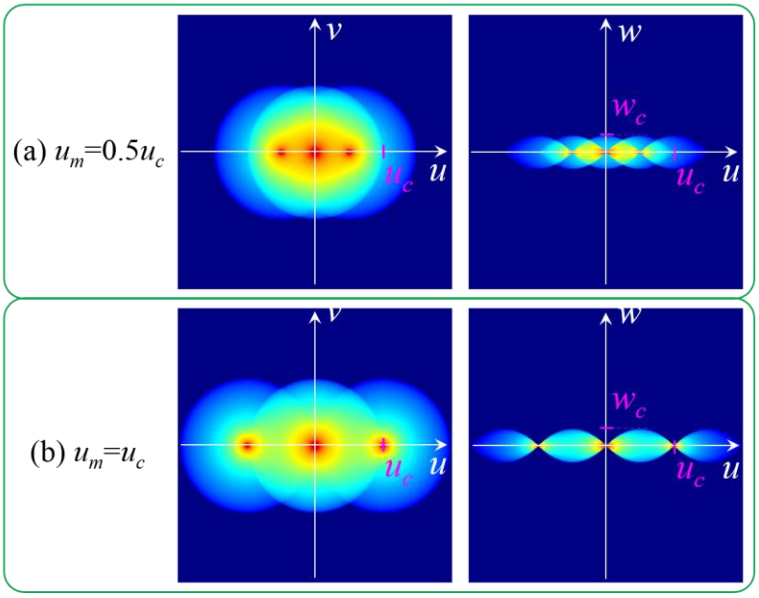

Fig. 6. The frequency support of the synthetic 2D-SIM OTF depends on the modulation frequency (u_m) of the SI pattern. *uv*-section and *uw*-section of the 3D synthetic OTF obtained from a SI pattern with: (a) $u_m = 0.5u_c$ and (b) $u_m = u_c$. Note that either the missing cone is completely filled providing OS (a) or the effective cutoff frequency is doubled providing SR (b).

1.3.2. Three-dimensional SIM (3D-SIM)

Three-dimensional structured illumination microscopy (3D-SIM), in which the structured illumination (SI) pattern varies laterally and axially, can be implemented traditionally by interfering three coherent waves (3W-SIM) [14] and recently by using a tunable-frequency incoherent illumination based on a Fresnel biprism and multiple linear sources (tunable 3D-SIM) [16].

The intensity of the 3D SI pattern in 3W-SIM system can be derived by the time average of the modulus squared of the total complex amplitude of the three beams (by illuminating coherently a diffraction grating and blocking orders except the zero and ±1 terms) [14]:

$$i(\boldsymbol{x},z)=\left\langle\left|\sum_{j=1}^{3}E_j\left(\boldsymbol{x},z,t\right)\right|^2\right\rangle=\left|\sum_{j=1}^{3}E_j\left(\boldsymbol{x},z\right)\right|^2, \tag{10}$$

where, $\boldsymbol{x}=(x,y)$ and z denotes the lateral and axial coordinates and E_j is the complex amplitude of each beam (plane wave) and the three beams can be assumed to have equal amplitude distributions given by $E_j\left(\boldsymbol{x},z\right)=E_0\exp\left[i\frac{2\pi}{\lambda}(\boldsymbol{x}\sin\beta,z\cos\beta)\right]$, where β is the angle between each side beam direction and the optical axis. Therefore, the 3D SI pattern in three-wave interference SIM, can be expressed by:

$$\begin{aligned}i(\boldsymbol{x},z)&=\left(E_1+E_2+E_3\right)\left(E_1+E_2+E_3\right)^*\\&=3E_0+2E_0\cos\left(\frac{2\pi}{\lambda}\boldsymbol{x}(\sin\beta_1-\sin\beta_2)+\frac{2\pi}{\lambda}z(\cos\beta_1-\cos\beta_2)\right)\\&\quad+2E_0\cos\left(\frac{2\pi}{\lambda}\boldsymbol{x}(\sin\beta_1-\sin\beta_3)+\frac{2\pi}{\lambda}z(\cos\beta_1-\cos\beta_3)\right)\\&\quad+2E_0\cos\left(\frac{2\pi}{\lambda}\boldsymbol{x}(\sin\beta_2-\sin\beta_3)+\frac{2\pi}{\lambda}z(\cos\beta_2-\cos\beta_3)\right)\end{aligned} \tag{11}$$

where $\beta_1=\beta$, $\beta_2=0$ and $\beta_3=-\beta$. Therefore,

$$i(\boldsymbol{x},z)=3E_0\left[1+\frac{2}{3}\cos\left(2\pi u_m\boldsymbol{x}\right)+\frac{4}{3}\cos\left(2\pi w_m z\right)\cos\left(2\pi\frac{u_m}{2}\boldsymbol{x}\right)\right] \tag{12}$$

where

$$\begin{aligned}u_m&=\frac{2\sin\beta}{\lambda}\\w_m&=\frac{1\text{-}\cos\beta}{\lambda}\end{aligned} \tag{13}$$

are the lateral and axial modulation frequencies, respectively. It is important to mention that the lateral and axial modulation frequencies of the SI pattern of 3W-SIM system are related and they exclusively depend on the period of the grating used. The change of the grating changes both lateral and axial frequencies and there is no way to tune the axial frequency while keeping the lateral frequency invariant. In general, we can rewrite Eq. (12) as follows:

$$\begin{aligned} i(\boldsymbol{x},z) = 1 + \frac{2}{3}\cos\left[2\pi u_m\left(\cos\theta x + \sin\theta y\right) + \varphi\right] \\ + \frac{4}{3}\cos\left(2\pi w_m z\right)\cos\left[2\pi\frac{u_m}{2}\left(\cos\theta x + \sin\theta y\right) + \frac{\varphi}{2}\right] \end{aligned} \tag{14}$$

where φ and θ are the phase and the orientation of the SI pattern, respectively. As it is clear from Eq. (14), there is an axial variation in 3D-SIM [see Fig. 7(b)]. The FT of Eq. (14) assuming $\varphi = 0,\ \theta = 0$ for simplicity (without loss of generality) shows that the SI pattern of the 3W-SIM system has five unique delta functions in the frequency domain located at the following frequencies:

$$\begin{aligned} I(\boldsymbol{u},w) = \delta(\boldsymbol{u},w) + \frac{1}{3}\delta(u - \frac{u_m}{2}, v, w \pm w_m) + \frac{1}{3}\delta(u + \frac{u_m}{2}, v, w \pm w_m) + \\ \frac{1}{3}\delta(u - u_m, v, w) + \frac{1}{3}\delta(u + u_m, v, w). \end{aligned} \tag{15}$$

Fig. 7(c) and (d) show the frequency representation of the SI pattern in 3W-SIM, which confirm that there are five unique delta functions.

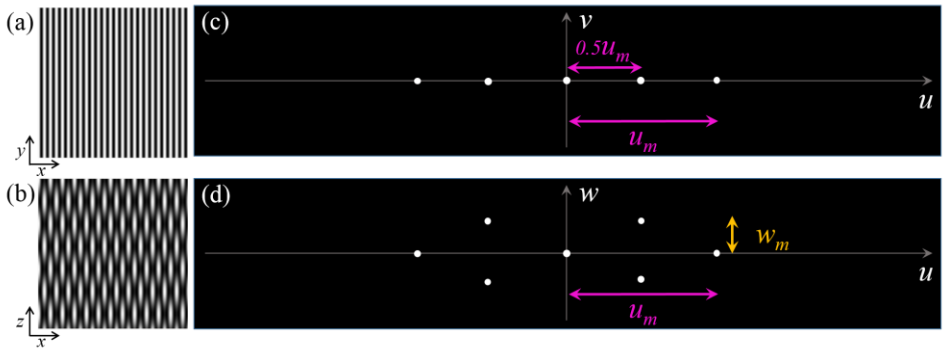

Fig. 7. The SI pattern in 3W-SIM. Space representation: (a) *xy*-section and (b) *xz*-section (c). Frequency representation: *uv*-section; (d) *uw*-section.

As mentioned earlier, the second approach to generate the 3D SI pattern is based on a Fresnel biprism illuminated by multiple linear sources (slits). In our tunable 3D-SIM system, axially-localized high-contrast sinusoidal patterns are generated by incoherent overlapping of axially-extended interference patterns produced by a set of equidistant parallel incoherent linear sources (slits) and a Fresnel biprism [16,22]. The incoherent superposition of these interference patterns produces a 3D SI pattern that is axially periodic. The irradiance distribution of the 3D SI pattern in the sample volume is given by:

$$i(\mathbf{x},z)\approx 1+\mathcal{V}(z)\cos(2\pi u_m\left(\cos\theta x+\sin\theta y\right)+\varphi), \tag{16}$$

where φ and θ are the phase and the orientation of the SI pattern, respectively, and

$$\mathcal{V}(z)=\frac{\sin(2\pi N w_m z)}{N\sin(2\pi w_m z)}, \tag{17}$$

defined as the visibility function [16], depends on the number of slits N, and on the lateral and axial modulation frequencies, respectively, as follows:

$$u_m = \frac{2\eta(n_F - 1)\tan\delta}{\lambda f_{L1} M_{ill}}$$
$$w_m = \frac{x_0 u_m}{2 f_{L1} M_{ill}}, \tag{18}$$

which are determined by the following system parameters: excitation wavelength (λ), biprism position (η), focal length of the first converging lens (f_{L1}), lateral magnification of the illumination system (M_{ill}), the refringence angle of the biprism (δ), the refractive index of the biprism (n_F), and the distance between two neighboring slits (x_0).

It is worth mentioning that the lateral and axial modulation frequencies of the tunable-frequency 3D pattern [Eq. (18)] can be controlled separately by system parameters, which is not the case in the 3W-SIM system. The lateral modulation frequency (u_m) can be tuned, up to the cutoff frequency of the system (u_c), by axially changing the position of the Fresnel biprism (η) w.r.t. the slits' plane. Although the axial modulation frequency (w_m) depends on u_m, it can be tuned independently by selecting x_0 in the design of the slits element while keeping u_m constant. We observe that the fringes' visibility is a periodic function that takes its maximum value [$\mathcal{V}(z) = 1$] at a discrete set of axial planes, referred to as the resonant planes.

As it is clear from Eq. (16), there is an axial variation in the 3D SI pattern of the tunable 3D-SIM system [see Fig. 8(b)]. The FT of Eq. (16) assuming $\varphi = 0,\ \theta = 0$ for simplicity (without loss of generality) shows that the SI pattern of the tunable 3D-SIM system has three unique delta functions in the frequency domain:

$$I(\boldsymbol{u},w)=\delta(\boldsymbol{u},w)+\frac{1}{2N}\sum_{n=0}^{N-1}\delta\left[u-u_m,v,w-\left(2n-N+1\right)w_m\right]+\frac{1}{2N}\sum_{n=0}^{N-1}\delta\left[u+u_m,v,w-\left(2n-N+1\right)w_m\right]. \tag{19}$$

Fig. 8(c) and (d) show the frequency representation of the SI pattern in tunable 3D-SIM, which confirms that there is three unique delta functions.

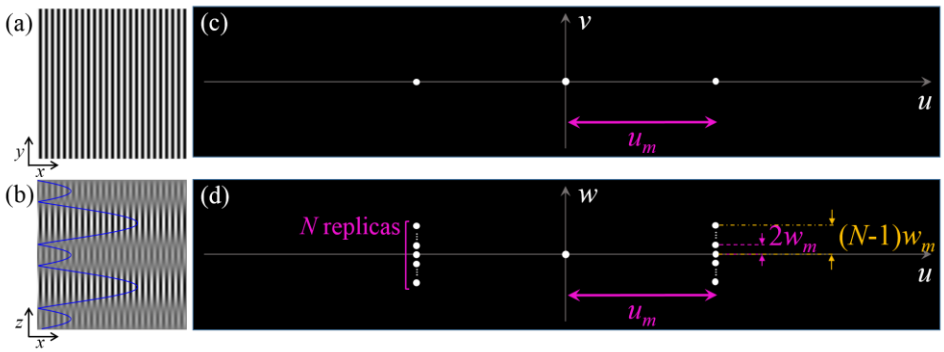

Fig. 8. The SI pattern in tunable 3D-SIM. Space representation: (a) *xy*-section and (b) *xz*-section (c). Frequency representation: *uv*-section; (d) *uw*-section.

A tunable-frequency 3D-SIM has been implemented in the Computational Imaging Research Laboratory (CIRL) of the department of Electrical and Computer Engineering, at the University of Memphis (Memphis, TN) in collaboration with the 3D Imaging and Display Laboratory, department of Optics at the University of Valencia (Valencia, Spain). Proof-of-concept results from this open set-up implementation, show that the contrast of the SI pattern is not affected by the illumination system and it can be tuned up to cutoff frequency. This is because of the tunable 3D-SIM has the advantages of both coherent and incoherent illumination SIM systems since the SI pattern is created by the incoherent superposition of interference patterns generated by mutually-coherent point sources. Moreover, our system offers two significant advantages over conventional 3D-SIM

systems. First, the reduction in data acquisition (Chapters 3 and 5) and second, the decoupled tunability of the lateral and axial modulation frequencies (Chapters 3 and 4).

1.4. Contributions of the dissertation

As discussed in Section 1.3, the SI pattern plays the main role in the performance of SIM systems. The values of the modulation frequency, the axial and lateral variation of the pattern, and the axial confinement of the pattern determine the OS and SR capabilities of the final restored SIM images.

The traditional 2D-SIM systems have been developed to provide either the OS or the lateral SR by using appropriate modulation frequency as they can operate only in a single modulation frequency mode [12]. This tradeoff can be overcome by using a tunable-frequency 2D-SIM system and a proper reconstruction method [15]. The tunability of the modulation frequency can be solved by the use of electro-optical devices (e.g., reflective and transmissive spatial light modulators (SLMs) [24,25,34,35,26–33], which allow rapid generation of multiple SI patterns in a controlled way using either coherent or incoherent illumination. However, these devices are costly. We present an alternative cost-effective approach for a compact 2D-SIM system with tunable frequency SI pattern implemented using a Fresnel biprism and a single spatially-incoherent linear source. To take advantage of the tunability of our proposed SIM system, we also present a computational method that provides optical-sectioned images with super-resolution (OS-SR algorithm). Our computational approach can be applied to any tunable-frequency 2D-SIM by recording phase-shifted images from two independent modulation frequencies. The lower spatial modulation frequency provides OS capability by filling the missing cone and the other one

produces SR performance by almost doubling the cutoff frequency of the conventional WF system. These two datasets are properly combined to provide simultaneous OS and SR in the reconstructed image. Although, in the last decade, other computational methods have been proposed to enhance the resolution in WF imaging based in part on a 2D-SIM approach [36–41], to our knowledge, this is the first time that two data sets from a tunable-frequency 2D-SIM system are used to enhance both OS and SR capabilities. We have also investigated a computational approach to reduce residual fringes evident in the restored images from the Fresnel biprism-based incoherent tunable 2D-SIM system. This method can be applied to any SIM system with non-ideal sinusoidal pattern.

In addition to the tunable-frequency 2D-SIM system [15], a novel tunable-frequency 3D-SIM system, introduced in Section 1.3.2, has been implemented in an open setup and investigated numerically and experimentally [15,42]. The forward imaging model for the system is verified experimentally and two reconstruction methods have been used to evaluate the final images. In the investigated studies, the proposed tunable 3D-SIM system is shown to provide an increase in the lateral resolution limit by a factor of 1.8× compared to the native system and improved OS capability by a factor of 1.6× compared to the commercial ApoTome-SIM system by using $u_m = 0.8u_c$. Nonetheless, the main hallmark of the proposed 3D-SIM system is that it requires fewer images for the final restoration than the 3W-SIM (which is the standard 3D-SIM system that has been commercialized by Zeiss in Zeiss Elyra), while the performance of both systems appears to be comparable based on the compact support of the synthetic OTF comparison and numerical results from reconstruction of simulated data.

One of the advantage of this tunable-frequency 3D-SIM system is that both lateral and axial periodicity of the 3D fringes can be tuned independently, which is not the case of 3W-SIM system. This unique property allows us to engineer the synthetic OTF of the system for a desired imaging application. This is the first 3D-SIM setup that enables independent control of the achieved OS and SR capabilities. Although it is clear that the highest the u_m, the highest performance in lateral SR, we have verified that one can always design the slit-element, so that the 3D-SIM system operates at the highest axial SR and OS capability. We believe that our system will have a high impact in biological imaging applications where the highest lateral modulation frequency cannot be used due to a reduction in the SI pattern's contrast. This reduction can be caused by spherical aberration due to the refractive index mismatch between the immersion medium and the sample's medium and the sample depth. In those cases, our system enables the possibility to operate with the highest axial SR and OS capabilities even though the lateral SR has been reduced.

Current iterative deconvolution methods in SIM assume that the observed image can be modeled simply as the convolution of the fluorescence emission with the detection PSF. However, this model is not always true for 3D data depending on how the 3D data is acquired and how the SI pattern is changing axially. Here, we propose and implement a new 3D iterative deconvolution approach based on a model that takes into account the axial scanning of the specimen during the data acquisition as in commercial microscopes. The method minimizes the mean squared error using the conjugate gradient descent optimization method. This method is applicable for 2D-SIM and 3D-SIM systems, where the SI pattern is separable into axial and lateral functions. The effect of noise on the reconstructed results is also studied.

The research contributions can be summarized as follows:

1. Development of an image restoration method for tunable-frequency 2D-SIM to provide simultaneous OS and SR and assisting implementation of tunable-frequency 2D-SIM in an open setup [15,21,43].
2. Numerical and experimental verification of: i) the 3D SI pattern and the forward imaging model; ii) the achieved OS and SR capabilities of the system through the reconstructed images; and iii) assisting in the implementation of a tunable-frequency 3D-SIM in an open setup [16,42,44].
3. Engineering the illumination system design of the tunable 3D-SIM system based on the synthetic OTF's compact support, so that the overall system can operate with the highest OS and SR capabilities [45].
4. Development of a 3D model-based deconvolution method for SIM systems, in which the SI pattern is separable into axial and lateral functions, taking into account the axial scanning of the specimen during the data acquisition as in commercial microscopes [46,47].

1.5. Novelty of the work

The proof-of-concept results from the OS-SR algorithm show that the method reconstructs optical-sectioned images with double lateral resolution obtained from a tunable-frequency 2D-SIM system. Although our OS-SR method is based on a 2D-SIM system, it provides superior performance over single modulation-frequency 2D-SIM by providing simultaneous OS and SR information, which is the hallmark of 3D-SIM. This is the first time that two data sets from a tunable-frequency 2D-SIM system are used to

enhance both OS and SR capabilities, in which the proposed computational approach can be applied to any tunable-frequency 2D-SIM.

We have investigated the forward imaging model and the achieved OS and SR capabilities in a novel tunable 3D-SIM system implemented in an open setup. Moreover, we have investigated different SI designs in terms of the OS and SR capabilities of the tunable 3D-SIM system and show that the lateral and axial modulation frequencies of this SI pattern can be controlled separately by system parameters. This unique property allows us to engineer the synthetic OTF of the system for a desired imaging application. While both the lateral and axial modulation frequencies of the pattern can be continuously tuned by axially changing the position of the Fresnel biprism, we have demonstrated that the slit-element can always be designed so that our 3D-SIM system operates at the highest axial SR and OS capabilities even though the lateral SR must be reduced due to the depth. We believe that our system will have a high impact in those biological imaging applications where the highest lateral modulation frequency cannot be used due to a reduction in the SI pattern's contrast. This reduction can be caused by spherical aberration due to the refractive index mismatch between the immersion medium and the sample's medium and the sample depth.

The 3D model-based image restoration approach presented in Chapter 5 is novel in the sense that it addresses the axial scanning of the specimen during the 3D data acquisition as in commercial microscopes, and thereby improving the quality of the restored images based on the archived resolution and artifacts. The crucial point demonstrated here is the use of the correct 3D imaging model to compute the 3D reconstruction. To our knowledge, such

a restoration method has not been published to date. As expected, any model mismatch in a model-based reconstruction approach can cause artifacts in the restored images.

2. 2D-SIM WITH AN INCOHERENT ILLUMINATION PATTERN OF TUNABLE FREQUENCY

This chapter is a paper by H. Shabani, A. Doblas, G. Saavedra, Emilio Sanchez-Ortiga, and C. Preza published in Applied Optics, Volume 57(7), B92-B101 (2018).

Improvement of two-dimensional structured illumination microscopy with an incoherent illumination pattern of tunable frequency

Hasti Shabani,[1,*] Ana Doblas,[1,*] Genaro Saavedra,[2] Emilio Sanchez-Ortiga,[2] and Chrysanthe Preza[1,#]

[1]*Department of Electrical and Computer Engineering, The University of Memphis, Memphis, TN 38152, USA*

[2]*3D Imaging and Display Laboratory, Department of Optics, University of Valencia, Burjassot, E-46199, Spain*

*#Corresponding author: cpreza@memphis.edu; *First two co-authors have contributed equally to this work.*

Abstract: In two-dimensional structured illumination microscopy (2D-SIM), high-resolution images with optimal optical-sectioning (OS) cannot be obtained simultaneously. This tradeoff can be overcome by using a tunable-frequency 2D-SIM system and a proper reconstruction method. The goal of this work is twofold. First, we present a computational approach to reconstruct optical-sectioned images with super-resolution enhancement (OS-SR) by using a tunable SIM system. Second, we propose an incoherent tunable-frequency 2D-SIM system based on a Fresnel biprism implementation. Integration of the proposed

computational method with this tunable structured illumination system results in a new 2D-SIM system that is advantageous compared to other 2D-SIM systems with comparable complexity, because it provides high-resolution optical-sectioned images independent of the objective lens used, without the presence of coherent noise and without reducing the contrast of the structured pattern as in other incoherent implementations. Evaluation of our proposed system is demonstrated with comparative studies of simulated and experimental reconstructed images to validate our theoretical findings. Our experimental results show a simultaneous improvement of the lateral resolution by a factor of 1.8× with the desired OS capability achieved in the resulting OS-SR combination image. Our experimental results also verify that our system can provide better OS capability than the commercial Zeiss ApoTome-SIM system in the investigated study.

OCIS codes: (180.6900) Three-dimensional microscopy; (110.2945) Illumination design; (110.1758) Computational imaging; (100.6640) Superresolution; (100.3020) Image reconstruction-restoration.

2.1. Introduction

Structured illumination microscopy (SIM) is a technique known for its potential to enhance both the axial and lateral resolution of conventional widefield fluorescence microscopy beyond the classical Abbe diffraction limit. In SIM, the underlying specimen is excited using a spatially-varying structured illumination (SI) pattern, which enables high-resolution three-dimensional (3D) images to be retrieved using the proper

computational reconstruction process. Among all types of SIM systems, there are two SIM approaches based on which traditional SIM systems have been developed and successfully commercialized. The first SIM approach, proposed by Neil and Wilson [10,18], is based on the generation of the SI pattern via the incoherent projection of a grating onto the sample plane. The main advantages of this implementation are: 1) the image of the grating is axially localized in the sample volume, which provides good optical-sectioning (OS) capability; 2) it does not present coherent noise; and 3) it has been successfully implemented in a commercial microscope as an add-on device (Zeiss ApoTome.2®). Nonetheless, this system is not aimed as a super-resolution technique because improvement in the lateral resolution is not significant due to the use of low modulation frequency structured patterns. This is because high-frequency information gets severely attenuated twice by the incoherent optical transfer function (OTF), due to its well-known shape, of both the illumination and detection imaging systems.

The second SIM approach was developed to enhance the lateral resolution. Super-resolution (SR) performance was achieved by Gustafsson [12] by illuminating the sample using a sinusoidal pattern created by the interference of two light beams emerging from a diffraction grating (2D-SIM). With this implementation, there is a tradeoff between OS capability (by filling the frequency information in the OTF's missing-cone) and doubling the lateral resolution [14,23]. To overcome this tradeoff, Gustafsson *et al*. [14] proposed illuminating the fluorescent sample with three mutually coherent beams from a diffraction grating and therefore the structured pattern varied in both the lateral and axial directions (3D-SIM). In commercial SIM systems based on Ref. [14], the SI pattern is generated using coherent illumination from a laser, which is known to result in images with coherent noise.

As with the ApoTome-based SIM system, the most important limitation of commercial SIM systems (such as, Zeiss Elyra, Nikon N-SIM and DeltaVision OMX and OMX SR from GE Healthcare Life Sciences) is that their performance is objective lens-dependent. Because only a discrete number of gratings is available, the OS and SR improvement is limited to only a particular set of objective lens. This problem can be solved by the use of electro-optical devices (e.g., reflective and transmissive spatial light modulators (SLMs) [24,25,34,35,26–33], which allow rapid generation of multiple SI patterns in a controlled way using either coherent or incoherent illumination. However, these devices are costly. In this study, we present an alternative cost-effective approach for a compact 2D-SIM system with tunable modulation-frequency SI pattern implemented using incoherent illumination. In our proposed setup, a Fresnel biprism [48,49] is illuminated by a wavefront emerging from one spatially-incoherent linear source and it produces a SI pattern in which the modulation frequency changes with the location of the Fresnel biprism along the optical axis. The use of a biprism in a coherent-based tunable-frequency 2D-SIM was previously demonstrated [50]. An additional advantage of this system is that the modulation contrast of the SI pattern is not attenuated by the illumination incoherent OTF (as in the case of the ApoTome-based SIM) and thus, its modulation frequency can always be set as high as the cutoff frequency of the objective lens used independently of the wavelength. Thus, our system is suitable for multi-color SR SIM imaging.

Additionally, to take advantage of the tunability of our proposed SIM system we also present a computational method that provides optical-sectioned images with super-resolution. Our computational approach can be applied to any tunable-frequency 2D-SIM by recording phase-shifted images from two independent modulation frequencies. The

lower spatial modulation frequency provides OS capability by filling the missing cone and the other one produces SR performance by almost doubling the cutoff frequency of the conventional widefield system. These two datasets are properly combined to provide simultaneous OS and SR in the reconstructed image. Although, in the last decade, other computational methods have been proposed to enhance the resolution in widefield imaging based in part on a 2D-SIM approach [41,51–55], to our knowledge, this is the first time that two data sets from a tunable-frequency 2D-SIM system are used to enhance both OS and SR capabilities. Preliminary results of this work have been presented in [21,56]. In this paper, we investigate experimentally the approach proposed in [21] based on the optical system provided in [56] in order to show a simultaneous improvement of the lateral resolution by a factor of 1.8× with the desired OS capability achieved by combining the OS and SR information. Here we compare OS capability of our system to the one provided by the commercial Zeiss ApoTome-SIM. To complete the study of [21], we have investigated different filters to combine the two different datasets. Moreover, since the structured pattern created by the Fresnel biprism cannot be described by a pure sinusoid we have proposed a computational approach to correct the envelope distorted the SI pattern.

The paper is organized as follows. Section 2 reviews the basic theory of 2D-SIM and presents our computational approach to combine OS and SR information. The performance of our approach is validated numerically and compared to the 3D-SIM [14] performance in simulation. In Section 3, we describe our incoherent-based tunable-frequency SIM system. Section 4 shows experimental implementation of our system and some experimental results obtained with our approach. Experimental comparison of results from

our system and the Zeiss ApoTome.2 system is also shown in Section 4. The main achievements of this study are summarized in Section 5.

2.2. Tradeoffs in 2D-SIM performance

2.2.1. Background

In a 2D-SIM system, the specimen under investigation is illuminated by a SI pattern, usually generated by interfering two coherent beams [12]. Therefore, the fluorescent sample is illuminated by an axially-extended sinusoidal pattern, $I(x,y)=1+\cos(2\pi u_m x+\phi)$ with modulation frequency u_m and initial phase ϕ. Since the imaging formation is a linear shift-invariant process, the 3D recorded image, $D(\cdot)$, is given by the 3D convolution of a uniformly scaled copy of the 3D distribution emitted from the object, $O(\cdot)$, and the 3D intensity point spread function (PSF) of the imaging system, [12,23]:

$$D(\mathbf{x},z)=\frac{1}{M^2}\left\{\left[1+\cos\left(2\pi\frac{u_m}{M}x+\phi\right)\right]O\left(\frac{\mathbf{x}}{M},\frac{z}{M^2}\right)\right\}\otimes_3\left|h(\mathbf{x},z)\right|^2, \quad (1)$$

where $\mathbf{x}=(x,z)$ are the transverse coordinates, $h(\mathbf{x},z)$ is the conventional widefield amplitude PSF, $\otimes_3$ stands for the 3D convolution operator and M is the lateral magnification of the imaging system. The high-resolution information, which is encoded inside the compact support of OTF needs to be retrieved by a computational method. This task can be performed by capturing three modulated images in which the SI pattern has been laterally shifted. After straightforward mathematical manipulation, the 3D irradiance

distribution of the synthetic SIM forward image, $D_{SIM}(\cdot)$, can be expressed as the 3D convolution of the fluorescence intensity distribution emitted from the object, $O(\cdot)$, and a synthetic 3D PSF, $h_{SIM}(\cdot)$, provided by the SI pattern [23]:

$$D_{SIM}(\mathbf{x},z)=\frac{1}{M^2}O\left(\frac{\mathbf{x}}{M},\frac{z}{M^2}\right)\otimes_3 h_{SIM}(\mathbf{x},z), \tag{2}$$

where

$$h_{SIM}(\mathbf{x},z)=\left|h(\mathbf{x},z)\right|^2\cos^2\left(2\pi\frac{2u_m}{M}x\right). \tag{3}$$

Similar to the conventional widefield system, it is more illustrative to analyze the SIM imaging process in the spatial frequency domain. The 2D-SIM system is characterized by a synthetic OTF function, $H_{SIM}(\cdot)$, obtained by taking the Fourier transform of Eq. (3):

$$H_{SIM}(\mathbf{u},w)=H(\mathbf{u},w)+\frac{1}{2}H\left(u-\frac{u_m}{M},v,w\right)+\frac{1}{2}H\left(u+\frac{u_m}{M},v,w\right), \tag{4}$$

where $\mathbf{u}=(u,v)$ and w are the transverse and the axial frequency coordinates, respectively. The restored image, $\hat{O}(\cdot)$, can be computed by solving a set of linear equations, processing with a generalized Wiener filter, and finally shifting and properly combining the retrieved frequency components, a process detailed in Ref. [14]. Without loss of generality, we assume M = 1. Eq. (4) shows that the synthetic OTF is obtained as the sum of three-shifted replicas of the conventional widefield OTF, $H(\cdot)$. Consequently, the synthetic OTF of 2D-SIM is enlarged along the u axis compared to the conventional widefield OTF. As it is already known, this enlargement provides resolution improvement along the x direction,

which is the direction in which the SI pattern changes. In fact, the performance of 2D-SIM depends on the modulation frequency of the illumination pattern [14,23]. Fig. 9 shows the meridional section in the *uw* plane of the synthetic OTF for two different modulation frequencies ($u_m = 0.5u_c$ and $u_m = u_c$, where u_c is the cutoff frequency of the imaging system). From this figure, it is clear that there is a tradeoff between the OS and SR capabilities of the SIM system depending on the modulation frequency [14,23]. The best optical-sectioned image [Fig. 9(a)] does not have double lateral resolution, and the highest improvement of lateral resolution [Fig. 9(b)] is not accompanied by any improvement of the OS capability. Therefore, the conventional 2D-SIM systems are not able to provide simultaneously the highest improvement in lateral resolution and optical-sectioning

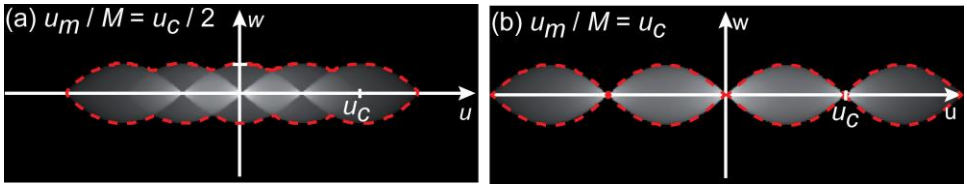

Fig. 9. The frequency support of the synthetic 2D-SIM OTF depends on the modulation frequency (u_m) of the SI pattern. *uw*-section of the 3D synthetic OTF obtained from Eq. (4) with M = 1 and a SI pattern with: (a) $u_m = 0.5u_c$ and (b) $u_m = u_c$. Note that either the missing cone is completely filled providing OS (a) or the effective cutoff frequency is doubled providing SR (b).

2.2.2. Proposed computational approach

To overcome the described issue of 2D-SIM and to provide both SR and OS, simultaneously, an approach to combine data from two modulation frequencies is proposed and investigated here. This approach requires that two SIM datasets (of 3 or 9 images total: 3 phase shifts at 1 or 3 orientation angles of the pattern fringe direction, respectively) with different u_m should be captured: one that supports OS and the other SR. The same

reconstruction method described above and detailed in Ref. [14] is first applied to the two 2D-SIM datasets to yield two restored images: $\hat{O}_{OS}(\cdot)$ and $\hat{O}_{SR}(\cdot)$ with OS and SR content, respectively. In this work, we propose a computational approach to combine the information from the OS and SR restored images as follows:

$$\hat{O}_{OS-SR}(\mathbf{x},z)=\hat{O}_{OS}(\mathbf{x},z)+h_{HP}(\mathbf{x},z)\otimes_3\hat{O}_{SR}(\mathbf{x},z), \tag{5}$$

where $h_{HP}(\cdot)$ is a spherically symmetric high pass filter with a radial profile in frequency domain defined by:

$$\tilde{h}_{HP}(\rho;n)=\begin{cases}(\rho/u_{OS})^n & \rho\le u_{OS}\\ 1 & u_{OS}<\rho\le u_{SR}\\ 0 & \text{otherwise}\end{cases}, \tag{6}$$

where u_{OS} and u_{SR} are the modulation frequencies for OS and SR datasets, respectively, $\rho=\sqrt{u^2+v^2+w^2}$, and n is the order of the high pass filter which is $n=0,1,2,3$ indicates no filter, linear, parabolic, and cubic filter, respectively. The goal of our approach is to retrieve high frequency information from the SR dataset while keeping the OS frequency information unaltered. Therefore, the filter should attenuate the low spatial frequencies of the SR part since we are interested in retaining the information at these frequencies from the OS part. Based on qualitative and quantitative comparisons (not shown), the performance of the parabolic and the cubic filters was found to be similar. This is consistent with the goal of our approach. Since the parabolic filter performs slightly better in resolving the fine structure of the object, we used it in the OS-SR combination results shown in the

paper. The design of a filter optimal in some sense may yield better results, however it is beyond the scope of this paper.

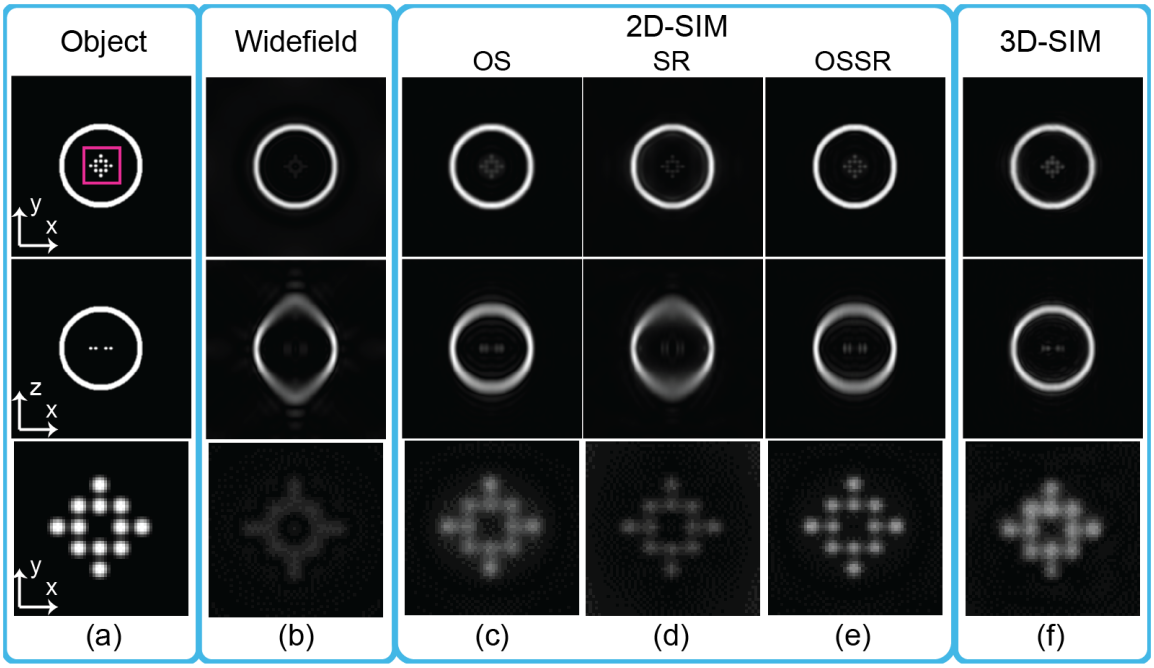

Fig. 10. Qualitative evaluation of the proposed method. Lateral view (top row), axial view (middle row) and zoomed view of the cropped square marked with a dashed pink line in the top left image (bottom row) of the 3D: (a) true object; (b) deconvolved widefield image using a Wiener filter; (c) reconstructed 2D-SIM image for $u_m = 0.5u_c = 2.7$ μm^{-1} (d) reconstructed 2D-SIM image for $u_m = 0.9u_c = 4.8$ μm^{-1}; (e) combined 2D-SIM reconstructed image with proposed method (Eqs. 5 & 6); and (f) reconstructed image from 3D-SIM raw data using the method in Ref. [14]. Scale bars: 1 μm (top and middle row) and 0.3 μm (bottom row). The cutoff frequency (u_c) is 5.4 μm^{-1} (the emission wavelength at λ = 515 nm and the imaging len's NA = 1.4).

To investigate the restoration performance of the proposed approach, a synthetic 3D test object was simulated on a 256×256×256 grid as shown in Fig. 10(a). An outer spherical shell and inner spherical beads to mimic a cell's structure in biological studies compose this object. While the diameter and the thickness of the spherical shell is 3 μm and 200 nm, respectively, the diameter of each bead is 125 nm and the closest distance between two neighboring beads is equal to 100 nm. The latter is below the resolution limit of the

conventional widefield microscope based on the parameters used for the microscope in this simulation study: emission wavelength at λ = 515 nm and the imaging len's numerical aperture (NA) is equal to 1.4. Therefore, the cutoff frequency is 5.4 μm^{-1} ($u_c = \frac{2\mathrm{NA}}{\lambda}$). The phase ϕ of the SI pattern is changed by $2\pi/3$ for the 3 phase images along three orientation angles: θ = 0, 60 and 120 degrees.

The lateral and axial views of the restored images of the test object (Fig. 10) show that the OS-SR combination result [Fig. 10(e)] incorporates the benefits of both the OS result [Fig. 10(c)] and SR result [Fig. 10(d)] images. To evaluate how well simultaneous OS and SR is achieved by our proposed method we compare this result with one we obtained using 3D-SIM [14] which is the benchmark for 3D optical-sectioned images with double lateral resolution [Fig. 10(f)]. Fig. 11 shows a quantitative comparison of these results [Fig. 10(a), (e) and (f)]. As expected, the performance of the proposed method is worse than 3D-SIM in the achieved OS as evident by the axial views [middle row in Fig. 10(e) and (f), respectively] because more axial frequencies are filled in the missing cone in 3D-SIM than in our approach. Theoretically both methods should provide the same lateral increase of the synthetic OTF since the modulation frequency of the pattern we simulated for the 3D-SIM image and the second image of our approach is the same ($u_m = 0.9u_c = 4.8$ μm^{-1}). Our simulated results show that the contrast of the lateral performance in our approach is slightly better [top and bottom rows in Fig. 10(e) and (f), respectively]. This result might be related to the use of the apodization filter [Eq. (6)] in our restoration method [Eq. (5)], in which the SR information is weighted by the filter in order to enhance the high-frequency content and thus the contrast of the restored images can be increased. However, because

such a filter is not used in the 3D-SIM approach, we did not apply it to the 3D-SIM result [Fig. 10(f)] shown here and this could be the reason between the contrast discrepancy. Overall, these noiseless simulation results verify the simultaneous OS and SR performance achieved by our approach, which is expected compared to 3D-SIM.

The current implementation of our proposed method uses 6 phase-shifted images (3 images per each modulation frequency) for each orientation angle of the pattern, as opposed to the 5 phase-shifted images required in 3D-SIM. This results in a 20% data-acquisition increase over 3D-SIM. However, it is worth noting that the two 2D-SIM datasets used in our approach have the same widefield component, and thus in fact only 5 phase-shifted images are needed to restore the OS-SR image. We plan to take advantage of this fact in our future implementation, thereby avoiding the current data-acquisition increase.

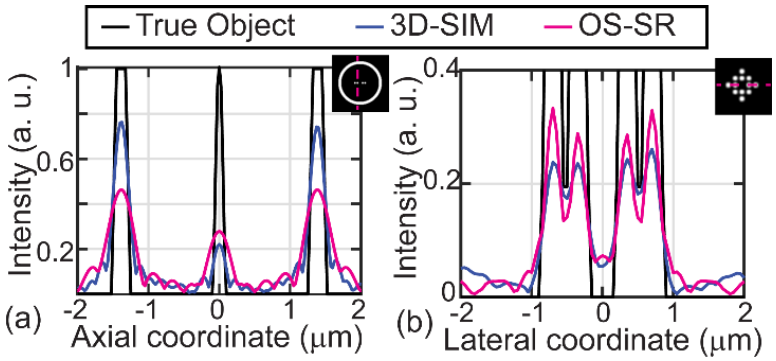

Fig. 11. Quantitative comparison of the proposed method and 3W interference SIM using the results shown in Fig. 10. Normalized intensity profiles from the: (a) axial view; and (b) lateral view of cropped image along *x* axis.

2.3. Incoherent tunable-frequency 2D-SIM based on Fresnel biprism

As mentioned above, integration of our proposed method to a tunable frequency SIM system is advantageous. This Section describes our incoherent tunable-frequency 2D-SIM system shown in Fig. 12. The frequency tunability is achieved by the use of a Fresnel biprism which is illuminated by the diffracted light emerging from a spatially-incoherent linear source [57]. The main advantage of the incoherent illumination is that: (i) no coherence noise distorts the recorded SIM images [56] and (ii) the contrast of the fringes is not penalized by the shape of the illumination OTF as in ApoTome-based SIM systems.

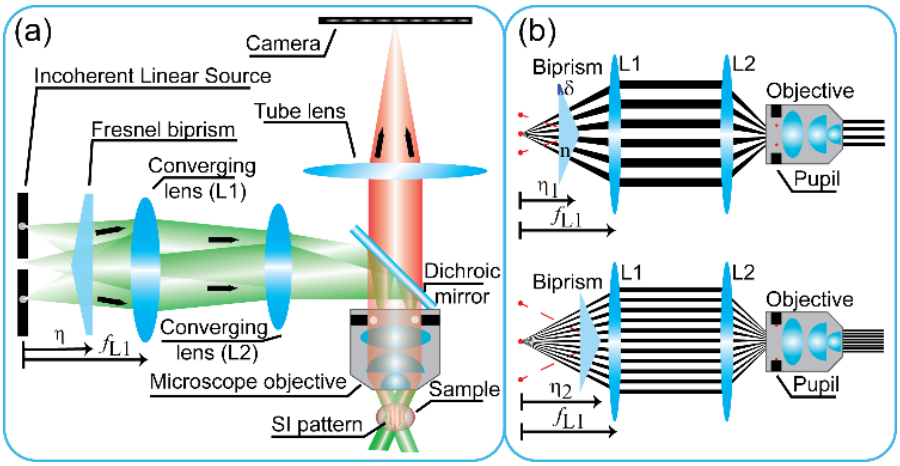

Fig. 12. (a) Illustration of the tunable-frequency 2D-SIM using a Fresnel biprism, which is illuminated by the diffracted light emerging from an incoherent linear source. (b) Tunable capability of our 2D SIM system. The lateral modulation frequency of the structured pattern (u_m) is changed by the axial displacement of the Fresnel biprism (η). Illustration for two modulation frequencies: half (top) or equal to (bottom) the cutoff frequency of the objective lens.

The use of a Fresnel biprism to generate interference patterns is a well-known strategy. It is based on the fact that this element generates the virtual splitting of a point source located at a distance η from it. These two virtual sources are located at the same plane of the original source, and symmetrically distributed from its original position along a line

perpendicular to the edge of the biprism (Fig. 12). The distance between these sources is given by a $a(\eta) = 2\eta(n-1)\tan(\delta)$, where n and δ are the refractive index (in general the dispersion of Fresnel biprism material is known to be less than 1.3% in the visible range) and the refringence angle of the biprism, respectively [48,49]. Because these twin sources come from the same real source, they are mutually coherent and a high-contrast interference pattern is generated at any transverse observation plane beyond the biprism. Note that any lateral displacement (along the *x* and *y* directions) of the real source generates a corresponding shift of the interference pattern. However, if the displacement occurs along the biprism's edge direction (*y* direction), this shifting is not distinguishable due to the invariance of the fringe structure along this direction [22,57].

The invariance along the y-direction of the interference patterns is, in fact, a key point for our incoherent SI proposal. Let us consider that the Fresnel biprism is now illuminated using an incoherent linear source (e.g. a slit). This incoherent-illuminated slit is aligned with the biprism's edge and placed at a distance η from it. Following the same reasoning as before, each point source of the slit generates the same high-contrast interference pattern at any observation plane behind the biprism. Thus, in noiseless conditions, since each incoherent point produces the same intensity distribution, there is just a reinforcement of the intensity signal compared with the case of the single-point source. However, in a realistic experimental situation, the result is slightly different. Note that in the presence of noise, the vertical (*y*) displacement of the interference pattern for each point of the slit, which is unobservable in the signal response, can be detectable in the coherent noise pattern. Nonetheless, when considering the whole set of points of the slit, an averaging effect appears since each point source is incoherent with respect to its neighbor. This results

in an incoherent superposition of all the interference patterns created by the point sources, washing out speckle noise and improving signal-to-noise ratio.

It is worth to highlight that our incoherent proposed SI method provides high-contrast interference patterns because it is based on incoherent superposition of coherent interference patterns generated by each point of an incoherent slit. In this way, when these coherent fringes are projected to the sample space through an illumination imaging system (L1 and L2 lenses in Fig. 12), each coherent interference pattern is transmitted without loss in visibility. This is a unique feature of using coherent imaging systems and it represents a clear advantage to incoherent grating-projection SIM techniques.

To finalize the description of our SI system, we discuss its tunability capability. One can realize that the separation between the virtual point sources, $a(\eta)$, can be tuned by changing the axial position, η, of the biprism with respect to the source plane. Since both virtual point sources are placed at the front focal plane of a converging lens (L1 lens), the interference pattern at any observation plane (z) beyond L1 lens has a period $p(\eta) = \frac{\lambda f_{L1}}{a(\eta)}$ [57], which is constant along z. Particularly, the higher the separation between the source and the biprism, the lower the value of the period is and, as a result, a higher spatial frequency is obtained. It is important to realize that when this setup is used as the illumination system in SIM, the image of the virtual sources is placed at the pupil plane of the objective lens [Fig. 12(b)]. Therefore, the higher the separation between the real source and the Fresnel biprism, the higher the separation of the virtual sources at the pupil plane, $a'(\eta) = \frac{a(\eta) f_{L2}}{f_{L1}}$, and the higher the spatial transverse frequency of the structured pattern,

$u_m(\eta) = \dfrac{a'(\eta)}{\lambda f_{obj}}$. Note that the SR performance is achieved when the separation between the virtual sources at the pupil plane occupies the whole pupil diameter, in which case the modulation frequency of the pattern coincides with the cutoff frequency of the objective lens [Fig. 12(b), bottom panel]. As noted earlier, the dispersion of the biprism material over the visible range is insignificant and therefore, the distance $a'(\eta)$ is also invariant to the wavelength used in this range. Since both the modulation frequency and the cutoff frequency, of the objective lens are affected by the wavelength is the same manner, the SR performance of our system can always be satisfied for different wavelengths without any change any the illumination set-up. Thus, our system has the same multi-color advantage as incoherent grid-projection SIM systems.

Taking advantage of our tunable 2D-SIM system allows us to change the modulation frequency of the SI pattern with minimal changes; we can record the two SIM datasets with different u_m (OS and SR datasets) and apply the reconstruction method proposed in Section 2 in order to obtain a synthetic OS-SR SIM image. It is worth to highlight that the generated SI pattern provided by the Fresnel biprism is not completely a pure sinusoidal pattern, because the waves emerging from each virtual incoherent source are abruptly cut off by the biprism's edge [48,49]. To obtain a reliable evaluation of the SI pattern created by the biprism we model its transmittance by Eq. (17) of Ref. [22] and calculate the amplitude distribution behind the Fresnel biprism. After some mathematical operations, the irradiance distribution, computed as the absolute square value of Eq. (2) of Ref. [57], the SI patterns created beyond L1 lens are expressed as:

$$I(\mathbf{x},z;\eta)=\mathrm{env}(\mathbf{x},z;\eta)+\vartheta_C(\mathbf{x},z;\eta)\cos\left(2\pi\frac{a(\eta)}{\lambda f_{L1}}x\right)+\vartheta_S(\mathbf{x},z;\eta)\sin\left(2\pi\frac{a(\eta)}{\lambda f_{L1}}x\right), \quad (7)$$

where

$$\mathrm{env}(\mathbf{x},z;\eta)=1+\mathrm{C}[\alpha]+\mathrm{S}[\alpha]-\mathrm{C}[\beta]-\mathrm{S}[\beta]+\mathrm{C}^2[\alpha]+\mathrm{S}^2[\alpha]+\mathrm{C}^2[\beta]+\mathrm{S}^2[\beta], \quad (8)$$

$$\vartheta_C(\mathbf{x},z;\eta)=1+\mathrm{C}[\alpha]+\mathrm{S}[\alpha]-\mathrm{C}[\beta]-\mathrm{S}[\beta]+2\mathrm{C}[\alpha]\mathrm{C}[\beta]+2\mathrm{S}[\alpha]\mathrm{S}[\beta], \quad (9)$$

$$\vartheta_S(\mathbf{x},z;\eta)=-\mathrm{C}[\alpha]+\mathrm{S}[\alpha]-\mathrm{C}[\beta]+\mathrm{S}[\beta]+2\mathrm{C}[\alpha]\mathrm{S}[\beta]-2\mathrm{C}[\beta]\mathrm{S}[\alpha]. \quad (10)$$

$C[\cdot]$ and $S[\cdot]$ are the Fresnel integrals defined as the criterion of Abramowitz and Stegun [58], and α and β are given by:

$$\begin{aligned}\alpha&=\sqrt{\frac{2\eta}{\lambda}}\,\frac{f_{L1}x+(n-1)\delta\left[f_{L1}{}^2+\eta z-\eta f_{L1}\right]}{f_{L1}\sqrt{f_{L1}{}^2+\eta z-\eta f_{L1}}},\\ \beta&=\sqrt{\frac{2\eta}{\lambda}}\,\frac{f_{L1}x-(n-1)\delta\left[f_{L1}{}^2+\eta z-\eta f_{L1}\right]}{f_{L1}\sqrt{f_{L1}{}^2+\eta z-\eta f_{L1}}}.\end{aligned} \quad (11)$$

From Eq. (7) it is clear that the SI pattern created by the biprism cannot be described by a pure sinusoidal function as shown in Fig. 13(a) where the pattern is distorted by an upper and lower envelope due to the biprism, described by Eqs. (8)-(11). To investigate this issue, we simulated the effect of these envelopes by comparing the forward and restored images of a 6-μm spherical bead with an ideal (a pure sinusoidal function) and the real [Eq. (7)] SI patterns. It is observable from Fig. 13(c) that there is a residual pattern in the restored image from the data with the real pattern, as expected. The proposed approach to reduce the effect of the envelope consists of two parts. First, a low pass filter is applied

to the background of the raw forward images or the calibration data (such as, the image of a flat sheet of fluorescence acquired with the same imaging conditions) to extract the frequency information of the envelopes in the real pattern. Then the effect of the envelopes in the forward images is reduced by point-wise dividing each raw image by the computed envelopes, where division by zero is avoided using a small additive constant in the denominator. Here, we assumed that the sinusoidal term in Eq. (7) is negligible, which is a valid assumption based on a comparison (not shown) between the terms defined by Eqs. (9) and (10). Second, a notch filter, which filters the residual frequency around the modulation frequency's vicinity, is applied to the restored image. As shown in Fig. 13(d), the proposed approach is able to reduce the residual pattern. Fig. 13(e) shows the normalized intensity profile along the center of the restored bead images in Fig. 13(b), (c) and (d) for a quantitative comparison and verification of the envelope correction method.

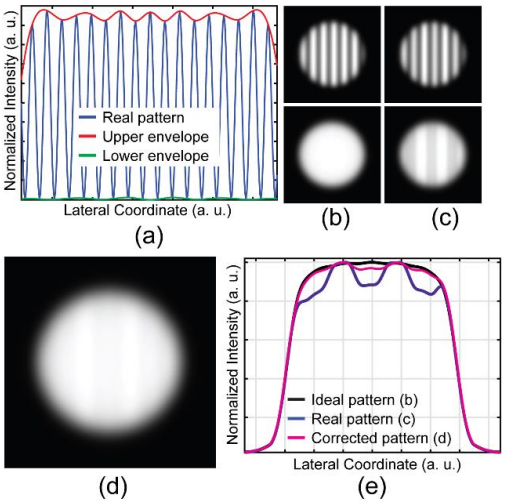

Fig. 13. Qualitative evaluation of the proposed envelope correction method to address the real SI pattern in tunable 2D-SIM based on the Fresnel biprism. (a) Real pattern generated by the biprism and the corresponding lower and upper envelope. Lateral view from the 3D: (b) forward image (top row) and reconstructed image (bottom row) with ideal sinusoidal pattern; (c) forward image with real pattern (top row) and its reconstruction with ideal sinusoidal pattern (bottom row); (d) reconstructed image after envelope correction applied to (c). (e) Quantitative comparison of images restored from ideal and real pattern SIM data assuming an ideal sinusoidal pattern, with and without envelope correction.

2.4. Experimental verification

This Section is divided in two subsections. Firstly, the implementation of our incoherent tunable-frequency SIM system is described and how experimental SIM data is acquired. After this brief description, experimental results are presented and discussed to show: a) improvement of the resolution achieved by using our system; b) successful integration of our tunable SI system with our proposed method (Section 2.2) to obtain optical-sectioned high-resolution images; and c) comparison of the optical-sectioning capability of our system with a commercially-available optical-sectioning technique (Zeiss ApoTome® SIM).

2.4.1. Experimental setup

The optical configuration of Fig. 12(a) has been implemented in an open-setup. In this setup, a variable-width linear source is illuminated incoherently by the light emerging from a 488-nm laser (Oxxius, RPMC Lasers, Inc., O'Fallon, Missouri) and passing through a rotating diffuser that removes spatial coherence (while other methods could also be used). In our setup, the rotating diffuser is imaged onto the linear source using a converging lens and the linear source is set at the front focal plane of a converging lens (L1) whose focal length is 100 mm. A Fresnel biprism with 2.5° angle and refractive index of 1.5194 at wavelength 532 nm (NewLight Photonics, Inc., Toronto, Canada) is used. To set the two virtual images of the linear source at the pupil plane of the objective lens, a converging lens (L2) of focal length 250 mm is inserted behind the L1 lens. The pupil plane of the objective lens is set at the back focal plane of the L2 lens, so that the objective lens (20X Plan NeoFluar 0.5 NA, Zeiss) recollimates the beams and creates the interference between

two plane waves in the objective lens' object focal plane, which is in the object space. This illumination irradiance pattern can be thought of as a demagnified replica of the irradiance pattern obtained after the L1 lens [Eq. (7)] whose lateral magnification is $M_{ill} = f_{obj}/f_{L2} =$ 0.032. Fluorescence light emitted by the sample is recollected again by the same objective lens and transmitted through a dichroic mirror of transmission cutoff wavelength $\lambda_c = 506$ nm. An emission filter (wavelength bandpass of 530 ± 50 nm) is inserted after the dichroic mirror to block the scattered excitation light. The emitted fluorescence distribution is imaged onto a high-sensitivity CMOS camera (Orca-Flash4.0 C11440-22CU, Hamamatsu) using an imaging system of lateral magnification $M_{det} = f_{TL}/f_{obj} = 37.5$. The camera has a 6.5×6.5 μm^2 cell, which produces a 0.173×0.173 μm2 pixel in the lateral object space.

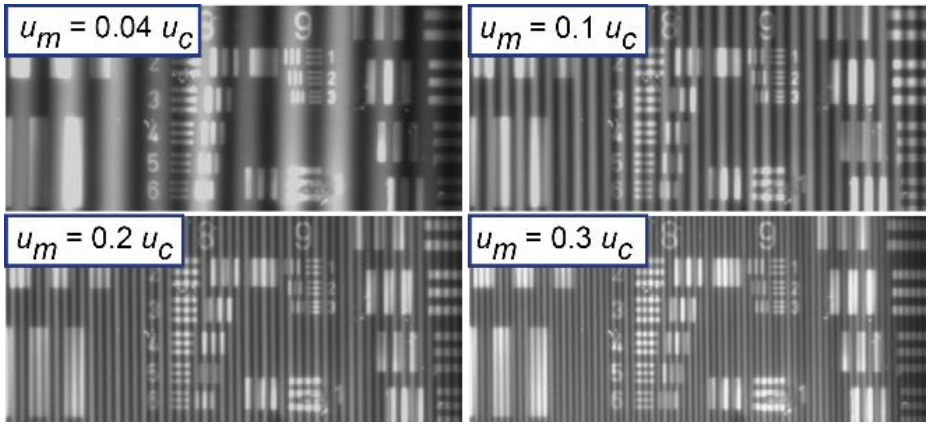

Fig. 14. Experimental verification of the frequency tunability capability of our SIM system. Fluorescent USAF target images acquired at four different axial positions of the Fresnel biprism in our open setup implementation. The cutoff frequency (u_c) is 1.9 μm^{-1} (the emission wavelength at $\lambda = 515$ nm and the imaging len's NA = 0.5).

3D datasets are acquired by axially scanning the sample volume using a motorized linear translation stage and 1-μm intervals, which is the smallest distance possible with this stage. For each transverse plane, we record three phase-shifted SIM images in which the phase of the illumination pattern is shifted by laterally translating the Fresnel biprism. For

this purpose, the Fresnel biprism is mounted onto a motorized translation stage. All these steps are implemented in an acquisition software developed in Labview©. With this software, we have control of the exposure time of the camera, the axial spacing between transverse planes and the lateral displacement of the Fresnel biprism. For all experimental data shown here, we used a 4-μm lateral displacement of the biprism.

To modify the modulation frequency of our structured pattern, the Fresnel biprism is mounted onto an optical rail that is parallel to the optical axis of our experimental system. Therefore, the tunability of the illumination pattern is obtained by axially displacing the Fresnel biprism. Fig. 14 shows images of a fluorescent USAF test (Ready Optics, Calabasas, California) acquired for four different axial positions of the biprism. These images show a variation by a factor of 7.5 in the modulation frequency of the pattern. Although this figure does not show high modulation frequencies, as we will show later, we are able to tune the modulation frequency until the cutoff frequency of the objective lens, where the experimental cutoff frequency is $u_c = 1.9\ \mu\text{m}^{-1}$. In general, this statement is valid for any objective lens used, however, in this current implementation, the focal length of the L1 and L2 lenses may have to be changed in order to achieve the highest modulation frequency for a different objective lens.

For ideal implementation, the linear source should be illuminated by the beam emerging from an ultra-bright light-emitting diode (LED), which is already a spatially-incoherent source. However, because the modulation frequency of the illumination pattern is wavelength-dependent, the higher the spectral bandwidth of the LED, the narrower the field of view (FOV) of the pattern. This results in using only LEDs with spectral bandwidth

< 10 nm if one wants to have a similar FOV as the one provided by the laser-diffuser implementation. Observing the experimental results of Fig. 2(c) of Ref. [56], one can realize the reduction of the FOV in terms of the bandwidth of the LED source.

2.4.2. Experimental results

Firstly, we are interested in verifying the resolution performance of our incoherent tunable-frequency SIM system. For this task, the fluorescent USAF target was imaged with our system using two different modulation frequencies ($u_m = 0.5u_c = 0.95\ \mu\text{m}^{-1}$ and $u_m = 0.9u_c = 1.7\ \mu\text{m}^{-1}$) and compared the achieved resolution to the resolution of the conventional widefield system. Fig. 15 shows the 2D Wiener-filtered image from the conventional raw data [Fig. 15(a)] and the reconstructed SIM images for both modulation frequencies [Fig. 15(b) and (c)]. It is worth to mention that these images were obtained after applying first the envelope function compensation (Section 3) using calibration data (e.g. the SIM image from a thin fluorescent layer) and followed by the proposed reconstruction SIM method (Section 2).

From Fig. 15 one can observe the lateral resolution achieved in each case. Note that for each case the smallest resolved element of the group 10 is highlighted by a dashed pink rectangle. Normalized intensity profiles along the vertical direction (marked by the two white arrows in Fig. 15) of group 10 are also compared [Fig. 15(g)] to indicate the resolution limit in each case. From the results in Fig. 15(d-f), we determined the highest detectable spatial frequency for each case to be: 1024 lp/mm (element 2 of group 10), 1448 lp/mm (element 4 of group 10) and 1825 lp/mm (element 6 of group 10), respectively. Therefore, the spatial frequency is increased by a factor of 1.4 for $u_m = 0.5u_c$ and a factor

1.8 for $u_m = 0.9u_c$ in comparison with the conventional imaging. As it is expected from the SIM technique, the use of a modulation frequency closer to the cutoff frequency of the imaging system almost doubles the resolution limit of the conventional system. Since the variation between the theoretical and experimental factor is less than 10%, one could claim that the improvement of the experimental resolution is predicted by the theory discussed in Section 2 within the error range.

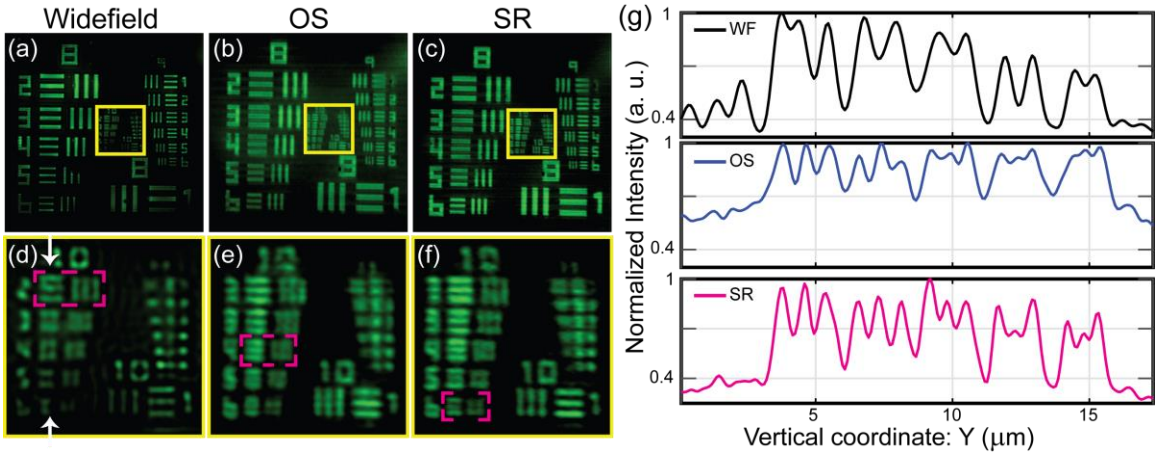

Fig. 15. Achieved SR verified in experimental images of the fluorescent USAF target: (a) & (d) Widefield restoration; (b) & (e) Reconstructed SIM image for $u_m = 0.5u_c = 0.95$ μm^{-1} (OS); (c) & (f) Reconstructed SIM image for $u_m = 0.9u_c = 1.7$ μm^{-1} (SR); (g) Intensity profile through the horizontal elements of group 10 along the direction marked by the arrows in panel (d). Images in (d)-(f) are zoomed versions of the areas indicated by the yellow squares in images (a)-(c), correspondingly. The groups marked with the pink dashed line in (d)-(e) indicated the achieved resolution in each case.

For the second experiment, we used again the USAF target as a sample to verify our computational approach described in Section 2. To have a proof of the OS improvement, the sample was tilted approximately 80 deg with respect to the optical axis. In Fig. 16, we show the OS reconstructed image corresponding to the SIM image for $u_m = 0.5u_c$ [Fig. 16(a)], the SR reconstructed image corresponding to the SIM image for $u_m = 0.9u_c$ [Fig.

16(b)], and the OS-SR reconstructed image corresponding to the image after applying our approach [Fig. 16(c)]. For better visualization of the enhancement of the resolution, cropped and zoomed views of groups 10 and 11 are shown in the second row of Fig. 16 for each case. As before, the dashed pink rectangles mark the smallest resolved element for each image. Based to these images, it is clear that the OS-SR image preserves the high spatial frequencies of the SR image since both of them present the same resolution limit (the highest resolved spatial frequency is 1825 lp/mm).

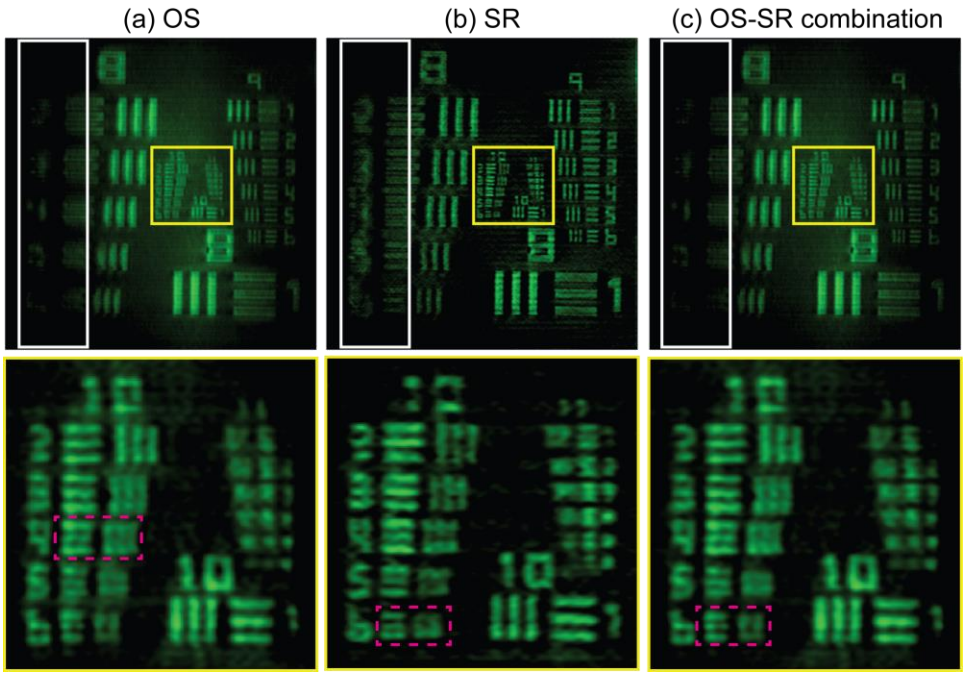

Fig. 16. Simultaneous OS and SR achieved and verified with experimental images of a tilted fluorescent USAF target: (a) Reconstructed SIM image for $u_m = 0.5u_c = 0.95\ \mu m^{-1}$ (OS); (b) Reconstructed SIM image for $u_m = 0.9u_c = 1.7\ \mu m^{-1}$ (SR); (c) Reconstructed 2D-SIM image with proposed method (OS-SR combination).

These experimental results coincide with those modeled in Section 2 and predicted by simulations in Fig. 10 and Fig. 11. Regarding assessment of the achieved OS, we compared the areas inside the white vertical rectangles located in the left side of each panel in the

first row of Fig. 16. From these areas, one can observe how the out-of-focus information is better rejected in the OS and OS-SR images than in the SR image. These results demonstrate that the depth discrimination of the OS-SR image is kept comparable to the OS case, while it has an increase in the lateral resolution by a factor of 1.8 over the conventional resolution, thereby providing a final image with an overall improvement in quality.

In our last experiment, we compared the performance of our incoherent tunable-frequency 2D-SIM with the Zeiss ApoTome.2® SIM module on a Zeiss AxioImager.Z2 upright microscope. For this experiment, as a sample we used a cluster of 6-μm spherical shells. The sample was a-priori prepared by mounting spherical shells of diameter 6-μm and a shell thickness of 1 μm (Invitrogen, Molecular Probes, FocalCheck microspheres, 6-μm fluorescent green ring stain/blue throughout) in ProLong Diamond (refractive index equal to 1.47). To fix the shells inside the mounting medium, the sample was cured at room temperature for 24 hours. The top panel of Fig. 17(a) shows a transverse section of the sample using widefield microscopy in which several spherical shells are clustered at different random locations. This cluster was captured using the ApoTome-SIM system [first row of Fig. 17(b)] and our incoherent tunable SIM system with two desired modulation frequencies [first row of Fig. 17(c)] in order to create the OS-SR image. It is important to realize that although we have used the highest modulation frequency possible for the ApoTome implementation, its value is much smaller compared to those in our implementation. Note that the modulation frequency for the ApoTome system is only 4% of the cutoff frequency of the objective lens used while our system allows us to tune it up to 90% of the cutoff frequency.

All raw images were properly processed to obtain the restored images shown in Fig. 17. It is important to mention that the images in Fig. 17(a) and (b) were restored using deconvolution methods implemented in the Zeiss ZEN.2 software [59] in which we have taken into account an aberrated PSF at a 30-μm depth, which is the determined pre-aberration of our experimental microscope [60], and the refractive index of the mounting medium. In both cases, the regularization parameter of the deconvolution method has been properly set to get the best image quality. The corresponding reconstructed images are shown in the second row of Fig. 17. Clearly, from these experimental results, one can realize that our system provides better OS capability than the commercial ApoTome-SIM system. Note that the intensity of the out-of-focus spherical shells (marked by the colored arrows) is less in the OS-SR image than in the other cases. Even though the contribution of the SR image is not visible in the OS-SR image since the size of the spherical shells is much higher than the resolution limit of our system, the OS-SR combination shows a 5% improvement in the signal-to-noise ratio (SNR), which was found to be equal to 26.3 dB, compared to the OS image, which has SNR = 25.1 dB. The SNR is computed by taking the ratio of the average intensity of the signal over the spherical shell with uniform intensity and the standard deviation of the background intensity. Moreover, the contrast for the OS and OS-SR images are 0.47 and 0.69, respectively. Therefore, in the OS-SR image both the SNR and the contrast have been improved. It is worth noting that the spherical shell of fluorescence is not evident in the restored images as expected. We believe that this is due to occlusion of the out-of-focus light within the cluster and perhaps the presence of an air bubble near the cluster. It is clear that there are residual fringes in Fig. 17(c) and this is because the envelope correction (Section 3) could not applied to these restorations, as

calibration data about the pattern's envelope is not available for this dataset. In the USAF target, data shown in (Fig. 15 and Fig. 16) the envelope information could be extracted from the background intensity. However, in the case of the 6-µm cluster, the object does not emit fluorescence light across the FOV, and thus calibration data (such as, the image of a flat sheet of fluorescence acquired with the same imaging conditions) is needed for the envelope correction.

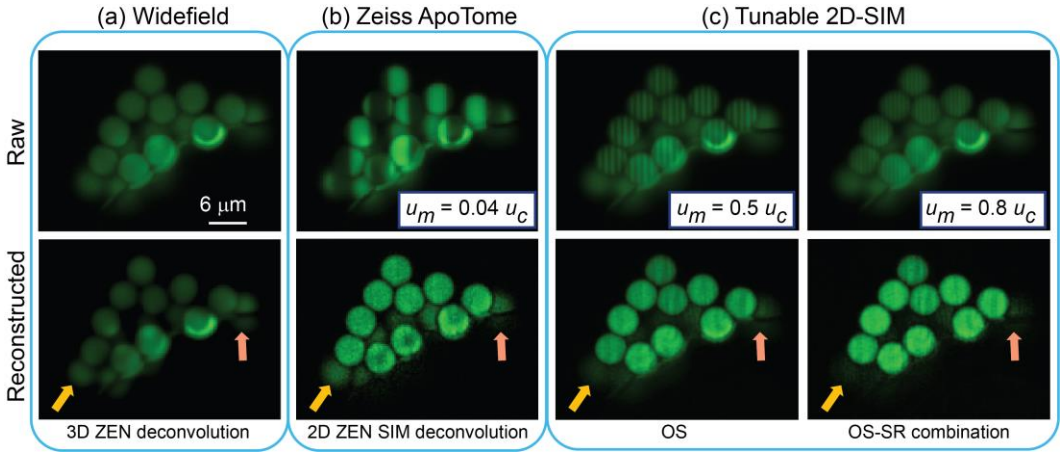

Fig. 17. Experimental validation of improved optical sectioning achieved with our approach. Experimental images of a 6-µm spherical shells cluster from different systems: (a) Zeiss AxioImager.Z2 Widefield; (b) Zeiss ApoTome.2®; (c) our tunable 2D-SIM. The reconstructed images of panels (a) and (b) are obtained using the Zeiss ZEN.2 software. The arrows illustrated that our system has better optical-sectioning capability over ApoTome.2®. Lens: 20×/0.5 NA; Emission wavelength: 515 nm.

2.5. Conclusion

We have shown the performance of an incoherent-based 2D-SIM system with tunable modulation frequency. In our system, the structured illumination pattern is generated by splitting an incoherent linear source using a Fresnel biprism. A key feature of this setup is that the structured pattern is free from coherence noise and its modulation contrast is not reduced through the illumination system. Additionally, our system is cost-effective and

produces a continuous variation of the pattern's frequency, up to the cutoff frequency of any commercially available objective lens independently of the wavelength used. Based on the later our system is suitable for multi-spectral imaging in fluorescence microscopy. In order to take advantage of our tunability capability, we have also proposed a computational OS-SR algorithm that reconstructs optical-sectioned images with double lateral resolution. Although our OS-SR method is based on a 2D-SIM system it provides superior performance over single modulation-frequency 2D-SIM by providing simultaneous OS and SR information, which is the hallmark of 3D-SIM. We are currently investigating the OS-SR combination with 5 images and we will report our studies in a future publication. Experimentally, we have applied the OS-SR algorithm to the image of a titled extreme USAF test. From the reconstructed OS-SR image, we show that the resolution limit is increased by a factor of 1.8× and the OS capability of the OS-SR is also enhanced. Finally, the performance in terms of the OS capability of our tunable 2D-SIM system was compared with the one provided by the Zeiss ApoTome.2® by imaging 6-µm spherical fluorescent shells in a test sample. Our results verified that our system provides better OS capability than the commercial ApoTome-SIM system in the case of this test sample.

Funding

National Science Foundation (NSF) (DBI 1353904), the University of Memphis; Ministerio de Economia y Competitividad (MINECO) (DPI2015-66458-C2-1-R); Generalitat Valenciana (PROMETEOII/2014/072).

Acknowledgments

We thank our collaborators Dr. Martinez-Corral (Univ. of Valencia, Spain), Dr. S. V. King (St. Jude Children's Research Hospital, Memphis, TN) for scientific and technical discussion and N. Patwary (PhD candidate, the University of Memphis) for assistance with ApoTome data acquisition and Zeiss ZEN processing.

3. TUNABLE-FREQUENCY 3D-SIM WITH REDUCED DATA-ACQUISISTION

This chapter is a paper by A. Doblas, H. Shabani, G. Saavedra and C. Preza, published in the ***Optics Express, Volume 26(23) 30476-30491 (2018).***

Tunable-frequency three-dimensional structured illumination microscopy with reduced data-acquisition

Ana Doblas[1,3], Hasti Shabani[1,3], Genaro Saavedra[2], and Chrysanthe Preza[1,*]

[1]Computational Imaging Research Laboratory, Department of Electrical and Computer Engineering, The University of Memphis, Memphis, TN 38152, USA.

[2]3D Imaging and Display Laboratory, Department of Optics, Universitat of València, E-46100, Burjassot, Spain.

[*]Corresponding author: cpreza@memphis.edu

[3]*First two co*-authors *have contributed equally to this work.*

Received 2 August 2018; revised 18 October 2018; accepted 21 October 2018; published 6 November 2018 (Doc. ID 341411).

Abstract: The performance of a tunable three-dimensional (3D) structured illumination microscope (SIM) system and its ability to provide simultaneously super-resolution (SR) and optical-sectioning (OS) capabilities are investigated. Numerical results show that the performance of our 3D-SIM system is comparable with the one provided by a three-wave interference SIM, while requiring 40% fewer images for the reconstruction and providing

frequency tunability in a cost-effective implementation. The performance of the system has been validated experimentally with images from test samples, which were also imaged with a commercial SIM based on incoherent-grid projection for comparison. Restored images from data acquired from an axially-thin fluorescent layer show a 1.6× improvement in OS capability compared to the commercial instrument while results from a fluorescent tilted USAF target show the OS and SR capabilities achieved by our system.

OCIS codes: (180.6900) Three-dimensional microscopy; (110.2945) Illumination design; (110.1758) Computational imaging; (100.6640) Super resolution; (100.3020) Image reconstruction-restoration

3.1. Introduction

Three-dimensional (3D) structured illumination microscopy (SIM) is a well-known method used to improve axial and lateral resolution beyond the diffraction limit in conventional widefield fluorescence microscopy [14]. Gustafsson *et al*. [14] demonstrated that illuminating a fluorescent sample with a structured illumination (SI) pattern, generated from the interference of three mutually-coherent beams emerging from a diffraction grating, enables detection of frequencies beyond the compact support of the optical transfer function (OTF) of the conventional system. This information can be properly demodulated from a set of five SIM images acquired from the same field of view (FoV) of a sample by phase shifting the SI pattern and then computing a final restored optical-sectioned image with double lateral and axial resolution. To achieve quasi-isotropic resolution, images in three different orientations of the SI pattern must be acquired resulting in 15 raw SIM

images for each FoV of a 3D sample. This technique has been successfully commercialized by several companies and has been used in a variety of biological studies [61–68]. Since the seminal paper in 2008, different research groups have implemented 3D SIM using a spatial light modulator (SLM) in order to tune the lateral modulation frequency of the SI pattern [28,29,32].

Because super-resolution (SR) SIM represents a promising high-throughput imaging method for revealing nanoscale morphological features in biological studies, we have been working towards a new simple, compact and cost-effective SI design that provides tunability of the lateral modulation frequency of the structured pattern using a Fresnel biprism. Recently, we have showed proof-of-concept results of this design in an incoherent two-dimensional (2D) SIM system (based on a SI pattern that is constant axially) capable of achieving simultaneously SR and optical sectioning (OS) due to its modulation frequency tunability using a two-shot data acquisition approach [15]. In this work we present a 3D-SIM system (based on a SI pattern that varies axially) with a clear advantage over the standard 3D-SIM system (in which the SI pattern is obtained as the interference between three waves) [14] in that it only requires acquisition of three raw images per SI orientation instead of five, while providing a comparable performance. As it is known, to achieve 3D isotropic resolution, images in 3 different orientations of the SI pattern must be acquired. This means acquiring 9 raw images per axial plane for our system and 15 for the standard 3D-SIM system [14]. Reducing the number of raw images in SIM to increase data-acquisition speed and reduce photo bleaching effects has been investigated by taking advantage of the redundancy of information in the raw SIM images when dealing with 2D samples [69–74]. All these efforts have focused on computational approaches for 2D data

processing using only 4 raw images acquired from each axial plane as follows: (1) one SIM image for each of the three orientations and a single widefield image; or (2) two phase-shifted SIM images from one orientation and one from each of the other two orientations. We expect that this reduction from 9 to 4 images per axial plane is applicable to our 3D-SIM system since the SI pattern in our system has only a single lateral modulation frequency as is the case in 2D-SIM systems. However, in the case of the standard 3D-SIM system [14] 4 raw images are not sufficient as extra axial information is provided by the 3D SI pattern at half of the lateral modulation frequency. Notwithstanding, the reduction in data acquisition offered by our proposed 3D-SIM system is without any doubt a desired feature for the utility of SIM in live-cell imaging [14,29,32]. Furthermore, the proposed design for the 3D SI pattern presented here offers the possibility of designing *at will* a 3D-SIM system matched to the specific needs of a biological application, and thus providing the best system performance. Investigation of this property will be reported in a future publication. Here we validate experimentally the features of the 3D SI pattern and the implementation of a 3D-SIM system using this novel 3D pattern.

3.2. Fundamentals of tunable-frequency 3D-SIM based on a Fresnel biprism

3.2.1. Implementation of the tunable-frequency 3D-SIM system

The incoherent tunable-frequency 3D-SIM system presented here uses a SI design based on the illumination of a Fresnel biprism using a properly coded spatially-incoherent source. The source is composed by an array of N mutually-incoherent parallel equidistant slits with the same irradiance [22]. The optical configuration of our current experimental

setup is shown in Fig. 18. In this 3D-SIM system, both the lateral and axial modulation frequencies of the 3D structured pattern can be tuned by axially displacing the biprism. The irradiance distribution of the 3D structured pattern beyond the L1 lens in Fig. 18(b) can be approximated by:

$$e\left(\boldsymbol{x}_{ill}, z_{ill}; \eta, x_0, N\right) \approx 1 + \mathcal{V}'\left(z_{ill}; \eta, x_0, N\right) \cos\left[2\pi \frac{a(\eta)}{\lambda f_{L1}} x_{ill}\right], \tag{1}$$

where $\boldsymbol{x}_{ill} = (x_{ill}, y_{ill})$ and z_{ill} are the transverse and axial coordinates after the L1 lens (e.g. illumination space), x_0 is the lateral distance between two neighboring slits, λ is the source's wavelength, f_{L1} is the focal length of L1 lens and $a(\eta) = 2\eta(n-1)\tan\delta$ is the separation between the two sources created by the Fresnel biprism and depends on the biprism-slits distance (η), the refractive index (n) and the refringence angle (δ) of the biprism. It is important to mention that although Eq. (1) does not provide the full description of the structured pattern since the finite lateral extent of the biprism and the diffraction effect due to the biprism's edge have been neglected [22,43], the axial position of the maxima and minima of $\mathcal{V}'(z_{ill}; \eta, x_0, N)$ is predicted accurately. Also, we have verified that the effect of the envelope function introduced by the biprism's edge is less significant when the Fresnel biprism is illuminated by several spatially-incoherent slits (N).

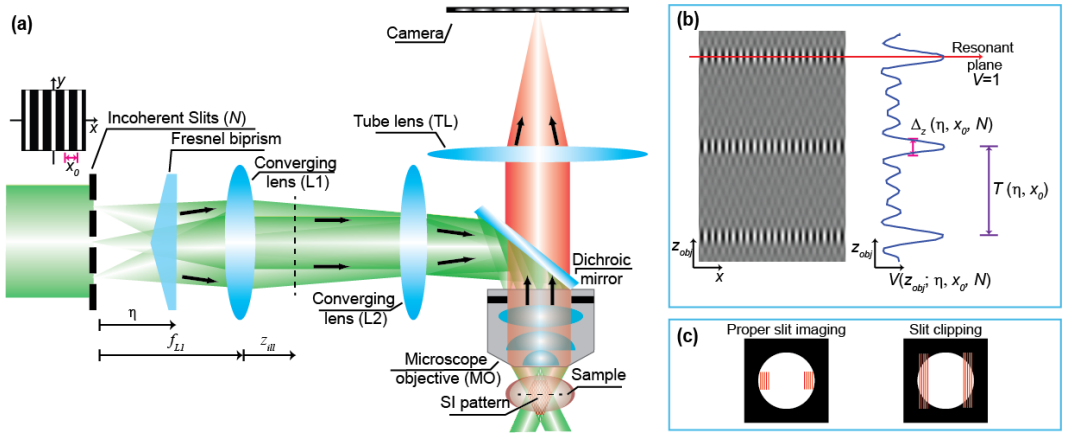

Fig. 18. Tunable-frequency 3D-SIM system based on a Fresnel biprism illuminated by a set of equidistant incoherent slits (N). (a) Illustration of the system. (b) 3D SI pattern with periodic visibility variation [Eq. (2)] created by the system in the sample space (z_{obj}). High-contrast fringes are located at a set of discrete axial planes. The 3D pattern exhibits a periodic axial contrast and its characteristics are controlled by three system parameters: N , x_0 and η . (c) Illustration demonstrating that improper imaging of the slits in the back focal-plane of the objective lens can lead to clipping of the slits and consequently, to a reduction in the contrast of the fringes. z_{ill} refers to axial coordinates located after L1 lens.

From Eq. (1) it is clear that the SI pattern varies axially due to $\mathcal{V}'(z_{ill};\eta,x_0,N)$. Following the same reasoning as in [22], the visibility function, which describes the variation in the fringes' contrast along the axial coordinate, is determined to be as follows:

$$V'\left(z_{ill};\eta,x_0,N\right)=\frac{\sin\left(2\pi N\, w'_m\left(\eta,x_0\right)z_{ill}\right)}{N\sin\left(2\pi w'_m\left(\eta,x_0\right)z_{ill}\right)}, \tag{2}$$

where $w'_m(\eta,x_0)=\frac{a(\eta)x_0}{2\lambda f_{L1}^2}$ is the axial modulation frequency of the pattern. In Eq. (2) we have assumed that the slits' width, Δ, is infinitesimal and, consequently, the maximum of the visibility is always equal to 1. Equation (2) shows that the visibility of the irradiance distribution is a periodic function that only takes maximum values in a discrete set of axial planes [Fig. 18(b)]. Because the slits are set at the front focal-plane of L1 lens, the groups

of planes of maximum contrast [$\mathcal{V}'(z_{ill};\eta,x_0,N)=1$] referred to here as the resonant planes, are equidistant. The separation between the resonant planes, $T'(\eta,x_0)=1/w'_m(\eta,x_0)$, changes inversely with both the slits' separation (x_0) and the biprism position (η). Note that the position of the resonant planes and their separation are totally independent of the number of slits (N). In fact, the number of slits affects only the axial extent of the fringes, $\Delta_z(\eta,x_0,N)=2T'(\eta,x_0)/N$, defined by the region around each resonant plane in which the visibility function is zero. The higher the number of slits, the narrower the axial extent of the fringes.

To verify the performance of our SI device, the optical configuration of Fig. 18(a) has been implemented in an open setup. In our implementation, a custom-made set of slits is illuminated incoherently by the light emerging from a 488-nm laser (Oxxius, RPMC Lasers, Inc., O'Fallon, MO) after passing through a rotating diffuser that removes spatial coherence [56]. The customized slit array fabricated by Ealing Inc. (Scotts Valley, CA) contains 30 slits of 3-mm length and 10-μm width (Δ). The separation between two neighboring slits was specifically fabricated to be $x_0=100$ μm. A Fresnel biprism with a 2.5-deg angle (NewLight Photonics, Inc., Toronto, Canada) was inserted between the slit array and a converging lens (L1) of focal length 100 mm. Using a converging lens (L2) of focal length 250 mm and an infinity-corrected objective lens (20× Plan NeoFluar of numerical aperture (NA) equal to 0.5, Zeiss), a demagnified replica of the 3D SI pattern obtained after the L1 lens [Eq. (1)] is found in the object space. Note that the system composed by the L2 lens and the objective lens follows a telecentric-afocal configuration. The light emitted by the sample is recollected again by the same objective lens and imaged

onto a high-sensitivity CMOS camera with 6.5-μm square pixels (Orca-Flash4.0 C11440-22CU, Hamamatsu) using a converging lens (TL lens) of focal length 300 mm. The cutoff frequency ($u_c = 2\,\mathrm{NA}/\lambda$) of our imaging system is 1.9 μm^{-1} for an emission wavelength of 515 nm and a 0.5 NA lens. With an experimental detection-system lateral magnification, $M = -f_{TL} / f_{MO} = -36.6$, a lateral sampling of $0.178 \times 0.178\ \mu m^2$ is achieved in the object plane.

In all the experimental studies described here, the sample was mounted onto a motorized linear translation stage (FOC300, PIEZOCONCEPT, Inc. Lyon, France) and its volume was scanned in intervals of 0.3-μm. On the other hand, the three needed phase-shifted SIM images were captured by laterally displacing the Fresnel biprism [15] in steps of 4-μm, for a single orientation of the SI pattern. As in [15], the lateral modulation frequency of the pattern can be tuned by axially displacing the biprism (η). For this reason, the biprism is mounted onto a separate rail that is parallel to the optical axis.

3.2.2. Experimental validation of 3D structured illumination (SI) design

By replacing the dichroic mirror in Fig. 18(a) with a beam splitter and using a flat mirror as the object, we acquired images of the 3D SI fringes by axially scanning the sample volume. Fig. 19 shows *xz*-views from the experimental and numerical [computed using Eq. (1) and an illumination lateral magnification of $M_{ill} = -f_{MO} / f_{L2}$] interference patterns created using a different number of slits, i.e. $N = 5$, and 9. As previously predicted, Fig. 19 shows us that the increase of the number of slits (N) produces a decrease of the axial extent of the fringes. Particularly, the experimental axial extent of the fringes,

measured by the full-width half-maximum (FWHM) of the axial profile through a resonant plane at a lateral maximum (defined by the red arrows in Fig. 19) has been reduced from 3.3 μm to 2.3 μm as quantified in Fig. 19. Nonetheless, it is important to highlight that the axially-localized fringes are both axially and laterally periodic and these periodicities remain invariant to *N*. The experimental lateral modulation frequency has been measured as $u_m = (1.50 \pm 0.13)\ \mu\text{m}^{-1} = (0.77 \pm 0.07) u_c$, based on the mean and standard deviation of the four resonant planes shown in Fig. 19. The agreement of this value with the theoretical one, $u_m = \dfrac{a(\eta)}{\lambda f_{L1} M_{ill}} = 1.52\ \mu\text{m}^{-1} = 0.8 u_c$ for η = 56 mm, is high. Regarding the axial periodicity, the distance between two neighboring resonant planes in the experimental results, was determined to be equal to (8.25 ± 0.05) μm, which is consistent with the theoretical value, $T(\eta, x_0) = M_{ill}^2 T'(\eta, x_0) = 8.4$ μm. Note that the difference in these values is less than 2%.

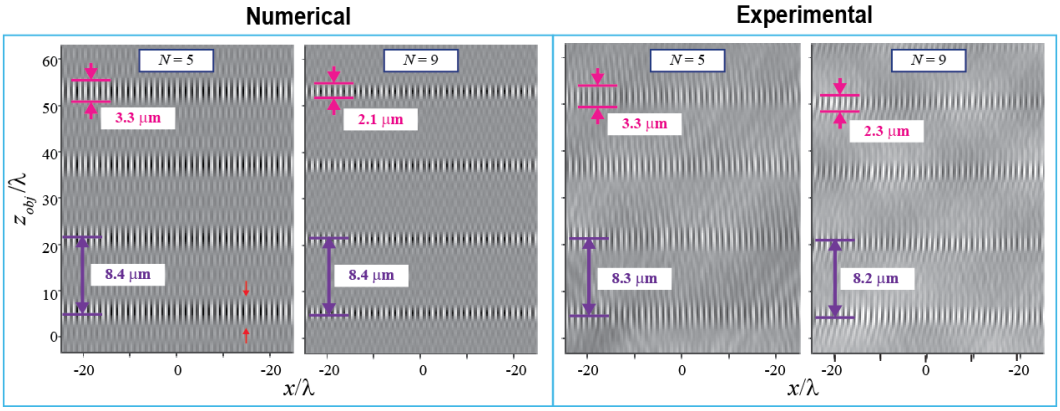

Fig. 19. Experimental and numerical *xz*-section images of the 3D SI pattern generated using a different number of slits N. The lateral (u_m) modulation frequency for both numerical and experimental results is $\sim 0.8 u_c$ and for $u_c = 1.9\ \mu\text{m}^{-1}$. The axial modulation frequency of the 3D SI pattern is $w_m = 0.0156 u_m$.

To conclude this comparison, we would like to mention that the contrast of the experimental fringes is not penalized by the increase of the number of slits, see Table 1 in [42]. This is because the slits have been illuminated in such a way that each point in a slit has its two virtual ones at the aperture stop [i.e., no clipping of the slits occurs as shown in Fig. 18(c)] and, therefore, the fringes' contrast is kept at the maximum value. However, if clipping of some of the virtual slits occurs [Fig. 18(c)], then, for each slit, some point of the coherent pair does not pass through the aperture stop and, therefore, the one which passes will contribute to the background provoking a reduction of the fringes' contrast.

In this 3D-SIM system, the axial displacement of the biprism (η) controls the lateral modulation frequency (u_m) [15] and the distance between regions of resonant planes (T), which is the inverse of the axial modulation frequency (w_m), and their axial extent (Δz). Fig. 20 shows the xz-sections of the 3D SI pattern recorded for two different axial positions of the biprism (η = 31 mm for $u_m = 0.44u_c$; and η = 54 mm for $u_m = 0.77u_c$) and the same number of slits ($N = 9$). Although the experimental values present a small variation, again, the degree of correlation between simulated and experimental data is very high. These images show a 34% reduction in the axial extent of the fringes when the lateral modulation frequency increases. Thereby, the higher the lateral modulation frequency, the greater the axial confinement of the fringes and the larger the axial modulation frequency. As we will show later, this leads to better out-of-focus light discrimination achieved by the system (i.e, improved OS capability). Again, it is important to mention that the change in the lateral modulation frequency does not affect the fringes' contrast, which means that their visibility is not penalized by the shape of the illumination OTF as in incoherent grid-projection SIM

systems [10]. For this experimental data, the measured contrast is 0.53 ± 0.03 for $u_m = 0.44u_c$ and 0.56 ± 0.03 for $u_m = 0.77u_c$.

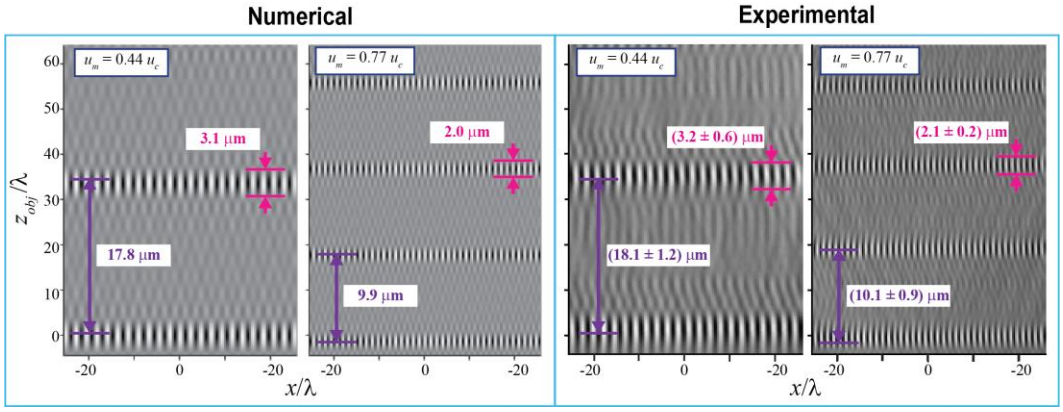

Fig. 20. Numerical and experimental *xz*-section images of the 3D SI pattern generated using a different lateral modulation frequency (u_m). The axial modulation frequency of the 3D SI pattern is $w_m = 0.0156u_m$. The cutoff frequency of the system is $u_c = 1.9\ \mu m^{-1}$. The number of slits used was $N = 9$. For the experimental data we report the mean and the standard deviation of the measured axial extent of the fringes computed from 12 axial profiles through the maxima of four different resonant planes.

To conclude the discussion, we would like to highlight the main features of our 3D SI device: (i) the contrast of the fringes is always maximum independent of the slit design (x_0 and N) or the lateral modulation frequency of the pattern (u_m) when clipping is avoided in the pupil plane; (ii) although both the axial modulation frequency and the lateral one are tuned by the position of the biprism, they are still decoupled because the axial modulation frequency can be set at will by changing the slit design (x_0); and (iii) the larger the number of slits (N), the greater the axial confinement of the high-visibility patterns. In addition, to these advantages, the fringes generated by the proposed 3D SI device are unaffected by coherence noise and their lateral modulation frequency can always be tuned to the effective cutoff frequency of the objective lens used. In what follows only

experimental results for $N = 9$ slits are shown, which is the maximum number of slits that can be set experimentally at the aperture stop of the 20×/0.5 NA objective for the highest lateral modulation frequency ($u_m = 0.8u_c$) and $x_0 = 100$ μm. Note that, for an ideal SIM system (e.g., no penalization through the illumination system and noiseless data acquisition), the fringes' contrast at a lateral modulation frequency of $u_m = 0.8u_c$ is attenuated by 0.1 (the value of the conventional detection modulation transfer function (MTF) at this frequency [75]) and, therefore, we have considered this frequency as the realistic effective cutoff frequency of an experimental setup.

3.2.3. Experimental validation of 3D image formation

Because the proposed excitation illumination pattern [Eq. (1)] is separable into axial and lateral functions, the intensity of a 3D image recorded by the camera in Fig. 18, $g(\boldsymbol{x}, z)$, can be expressed as [44]:

$$g(\boldsymbol{x}, z) = o(\boldsymbol{x}, z) \otimes_3 \left|h(\boldsymbol{x}, z)\right|^2 + \left\{\cos\left(2\pi u_m(\eta)\, x + \phi\right) \times o(\boldsymbol{x}, z)\right\} \otimes_3 \left\{\left|h(\boldsymbol{x}, z)\right|^2 \times \mathcal{V}(z; \eta, x_0, N)\right\}, \tag{3}$$

where $\boldsymbol{x} = (x, y)$ and z are the transverse and axial coordinates in the image volume, $o(\boldsymbol{x}, z)$ is the 3D density distribution of fluorophores within the sample volume, $|h(\boldsymbol{x}, z)|^2$ is the 3D PSF of the conventional widefield system, $\otimes_3$ stands for the 3D convolution operator, ϕ is the initial phase of the SI pattern, and

$$\mathcal{V}(z; \eta, x_0, N) = \frac{\sin\left(2\pi N w_m(\eta; x_0)\, z\right)}{N \sin\left(2\pi w_m(\eta; x_0)\, z\right)}, \tag{4}$$

where $w_m(\eta, x_0) = w'_m(\eta, x_0) / M_{ill}^2$ is the axial modulation frequency in the object space and it is proportional to the lateral modulation frequency, i.e., $w_m(\eta, x_0) = [u_m(\eta) x_0] / [2 f_{L1} M_{ill}]$. Without loss of generality, in Eq. (3) we assume that the lateral magnification of the detection imaging system (M) equal to 1. From Eq. (3) one realizes that the lateral modulation function modulates the object directly while the axial illumination function changes the axial behavior of the conventional PSF.

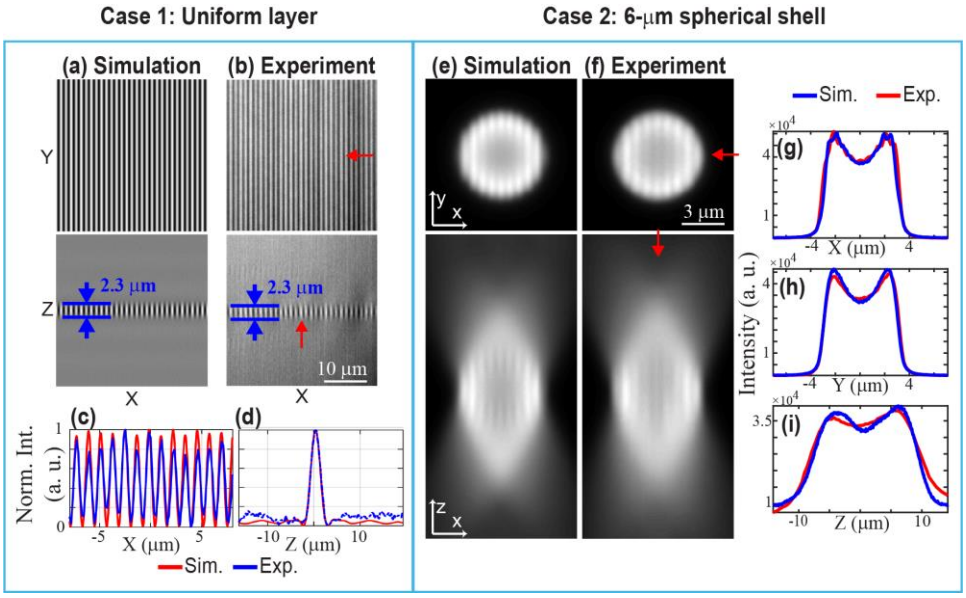

Fig. 21. Evaluation of the experimental 3D-SIM system ($N = 9$ slits) through comparison of experimental and numerical [Eq. (3)] 3D forward images of a fluorescent uniform layer (Case 1) and a 6-μm spherical shell (Case 2). Case 1: *xy* and *xz* views of the numerical (a) and experimental (b) 3D image; normalized lateral (c) and axial (d) intensity profile through the center (marked by the red arrows) of the *xy* and *xz* sections in (a) and (b), respectively. The experimental lateral profile was obtained from the average of 6 central rows while the axial profile was obtained from the average of 16 axial profiles through the maxima. Intensity profiles were obtained after background subtraction followed by normalization. Case 2: *xy* and *xz* views of the numerical (e) and experimental (f) 3D image; lateral (g, h) and axial (i) intensity profiles obtained from the center (marked by the red arrows) of the *xy* and *xz* sections in (e) and (f), respectively. The cutoff frequency $u_c = 1.9\ \mu m^{-1}$. Lateral and axial modulation frequencies: $u_m = 0.44 u_c = 0.85\ \mu m^{-1}$ and $w_m = 0.0135\ \mu m^{-1}$ for Case 1; and $u_m = 0.7 u_c = 1.33\ \mu m^{-1}$ and $w_m = 0.021\ \mu m^{-1}$ for Case 2.

To validate the imaging performance of the experimental system we imaged two different test samples and compared the experimental 3D-SIM images with numerical results provided by Eq. (3). The first object is an axially-thin fluorescent layer, originally placed at an arbitrary distance z_0 in the object space, i.e., $o(\boldsymbol{x}, z) = \delta(z - z_0)$. For this case, the lateral and axial modulation frequency was $u_m = 0.44u_c = 0.85\ \mu\text{m}^{-1}$ and $w_m = 0.0135\ \mu\text{m}^{-1}$, respectively. The experimental axially-thin fluorescent layer was created by inserting a drop of a regular liquid fluorescent marker between a coverslip and a glass slide. The 3D numerical and experimental forward images are shown in Fig. 21(a) and (b), respectively. For a quantitative comparison, we measured the FWHM of the axial extent of the region where resonant planes are located [Fig. 21(a) and (b), *xz*-view images]. The axial extent for both cases is 2.3 μm. Comparison of normalized intensity profiles along the lateral and axial directions show that experimental data is successfully predicted by the model [Fig. 21(c) and (d)]. Note that the minimum background values were first subtracted.

For the second evaluation study, the test sample consisted of 6-μm in diameter spherical shells with a shell thickness equal to 1 μm (FocalCheck, Invitrogen, Molecular Probes, Carlsbad, CA) embedded in ProLong Diamond antifade mountant (Invitrogen, Molecular Probes) with a refractive index of 1.47. A detailed description of the sample preparation can be found in [15]. To better mimic the experimental conditions, we included spherical aberration (w_{40} = 0.19 which is computed as in [76]) in the simulated PSF. In addition, Poisson noise was incorporated in the forward image [77] resulting in a noisy image with a signal-to-noise ratio (SNR) of 18.5 dB, which is equal to the experimental SNR in Case 2 of Fig. 21. The average photons in the experimental data were estimated from the

conversion datasheet provided by the camera's manufacturer and the SNR was computed by calculating the square root of the average photons over the entire 3D volume. Poisson noise was generated using the poissrnd built-in function of Matlab at a level comparable to the experimental data. For both simulated and experimental data we used a high lateral and axial modulation frequency $u_m = 0.7u_c = 1.33\ \mu\text{m}^{-1}$ and $w_m = 0.021\ \mu\text{m}^{-1}$ for η = 50 mm. Note that both lateral and axial modulation frequencies have been increased by a factor of 1.6 over Case 1. Fig. 21(e) and (f) show the corresponding *xy* and *xz* sections of the numerical and experimental data. Qualitative and quantitative agreement between the experimental and simulated 3D images is high, with only some evident discrepancies in the axial profiles depicted in panel (i). Thus, we conclude that the simulated data captures the trends in the experimental data.

3.2.4. Data Processing

To provide a better understanding of our system's performance, we analyze the imaging process of our SIM implementation by taking the Fourier transform of Eq. (3) to obtain:

$$G(\boldsymbol{u}, w) = D_0(\boldsymbol{u}, w) + \frac{e^{i\phi}}{2} D_{+1}(\boldsymbol{u}, w) + \frac{e^{-i\phi}}{2} D_{-1}(\boldsymbol{u}, w), \tag{5}$$

where $\boldsymbol{u} = (u, v)$ and *w* are the transverse and axial frequency coordinates,

$$D_n(\boldsymbol{u}, w) = O(u - nu_m, v, w)\, H_n(\boldsymbol{u}, w), \qquad n = 0, \pm 1, \tag{6}$$

and

$$H_n(\boldsymbol{u},w)=\begin{cases} H(\boldsymbol{u},w) & n=0 \\ \mathrm{FT}\left\{\left|h(\boldsymbol{x},z)\right|^2 \mathscr{V}(z;\eta,x_0,N)\right\} & n=\pm 1 \end{cases}. \tag{7}$$

$\mathrm{FT}\{\cdot\}$ indicates the Fourier transform operation.

Equation (7) shows the three terms that compose the effective synthetic OTF of our 3D-SIM system. The compact support of this synthetic OTF [Fig. 22(a), white dashed line] is comparable with the one achieved in three-wave interference (standard) 3D SIM (Fig. 22(b) white dashed line). Fig. 22 shows that both the lateral and axial effective cut-off frequencies of our implemented system for $N=9$ slits are equal with those of the standard 3D-SIM system. Additionally, this achieved OTF enlargement provides OS capability because the missing cone of frequencies present in the conventional OTF (Fig. 22, pink dashed line) is filled when 3D-SI is used. However, it is important to mention that the strength of the OTF for the three-wave 3D-SIM system [Fig. 22(b)] is greater, particularly in the axial direction, than the one observed in the OTF of the tunable 3D-SIM system with $N=9$ slits [Fig. 22(a)]. Note that, without considering the widefield component, there are 6 replicas in the three-wave 3D-SIM OTF and 18 ($2N$) in our synthetic OTF. Based on the conservation of energy, it is clear that the strength of each OTF replica in our system would be lower than in each replica in the three-wave SIM OTF. In addition, as the location of the replica overlap varies, the overall strength in different regions of the two systems' OTFs is different. Nonetheless, in our system design one can engineer the compact support of the 3D OTF and its strength by designing the slit element. A more detailed analysis of how the slit element affects the compact support of our system's OTF will be reported in a future study.

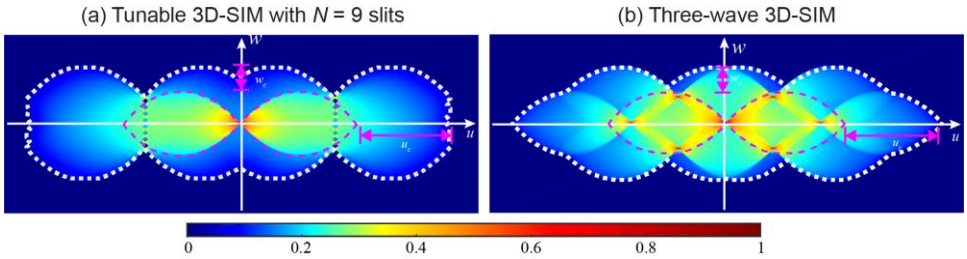

Fig. 22. Meridional section (uw) of the 3D synthetic MTF (absolute value of the synthetic OTF) for: (a) our 3D-SIM system with $N = 9$ slits; and (b) the conventional three-wave 3D-SIM system [14]. In both systems, we have considered the maximum lateral SR capability ($u_m = 0.8u_c$). Our synthetic OTF is composed of the 3 terms in Eq. (7). The pink and white dashed lines mark the compact support of the widefield and the 3D-SIM synthetic OTFs, respectively. The pink arrows highlight the extension of the lateral and axial cut-off frequencies achieved in both 3D-SIM synthetic OTFs.

Since the forward image's spectrum in tunable 3D SIM is composed by the sum of three shifted versions of the true sample's spectrum [Eq. (5)], only three forward images in which the SI pattern has been laterally shifted [ϕ in Eq. (3)] are needed to solve for the three unknown components, $D_n(\boldsymbol{u}, w)$. It is important to note that in the standard 3D SIM five images are needed to solve for five unique components. The standard reconstruction method for SIM [14] is based on a sequence of decomposition, deconvolution, shifting and recombination of these components. In our current system implementation, these unknown components are separated by solving a set of three linear equations and deconvolved using a generalized Wiener filter [14]:

$$\hat{D}_n(\boldsymbol{u}, w) = \frac{D_n(\boldsymbol{u}, w) H_n^*(\boldsymbol{u}, w)}{\sum_{n'} \left| H_{n'}(u + n' u_m - n\, u_m, v, w) \right|^2 + \beta^2} A(u - n\, u_m, v, w), \qquad n = 0, \pm 1 \qquad (8)$$

where $A(\boldsymbol{u}, w)$ is an apodization function that decreases linearly from unity at origin to zero at the border of the extended OTF support [14], * denotes the conjugate operator, and

β is a regularization parameter that needs to be adjusted empirically. Finally, the deconvolved components are shifted and combined properly (i.e., by ensuring that the energy of all deconvolved components is the same, thereby avoiding zeroth-order component dominance) to obtain the final restored image. To avoid undesired artefacts in the 3D restored image, the precise knowledge of the lateral modulation frequency and phase shifts in the modulated raw SIM images is critical. In experimental studies, we estimate these values by taking the Fourier transform of each raw SIM image and determining the phase associated with its sideband peaks [78].

Fig. 23 evaluates the performance of our 3D-SIM system and compares it to the performance of the standard 3D-SIM system [14] through restoration from simulated images of a numerical 3D test object. The 3D object was computed to mimic a cell's structure in biological studies. It is composed by an outer spherical shell (diameter = 3 μm and thickness = 200 nm) and inner spherical beads whose diameter is 125 nm. To show SR performance, the distance between two neighboring beads is equal to 100 nm, which is below the resolution limit of the conventional widefield microscope ($\lambda/2NA$ = 184 μm for an emission wavelength of λ = 515 nm and an imaging lens' NA = 1.4). In this numerical study, the phase of the SI pattern is changed by $2\pi/3$ for the 3 phase images in the tunable 3D-SIM system and $2\pi/5$ for the 5 phase images needed in three-wave 3D SIM along three orientation angles of the pattern (θ = 0°, 60° and 120°) to achieve isotropic resolution improvement. Furthermore, Poisson noise was introduced in the forward image [77] resulting in a SNR of 18.5 dB (equal to the experimental SNR in Case 2 of Fig. 21). The regularization parameter was empirically determined and it was set equal to β = 0.002. Negative values in the restored images due to Wiener filtering were set to zero. Qualitative

observation of the 3D restored images from both systems [Fig. 23(b) and (c)] as well as comparison of intensity profiles through them [Fig. 23(e) and (f)] indicate that the overall performance of both systems is quite comparable. These results are consistent with the comparison of the two systems' synthetic-OTF compact support (Fig. 22).

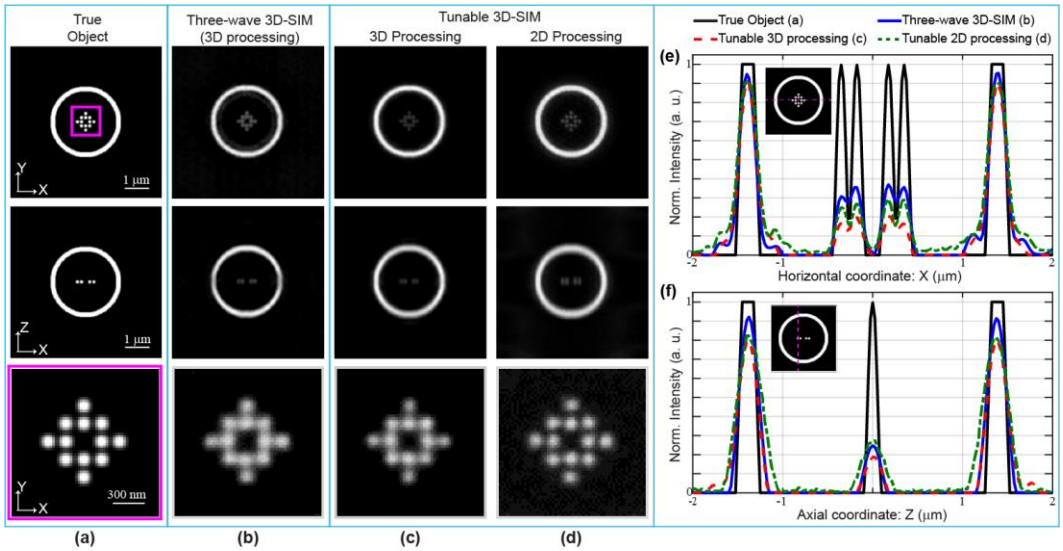

Fig. 23. Qualitative and quantitative evaluation of the proposed 3D-SIM system performance using simulated data. Lateral view (top row), axial view (middle row) and zoomed view of the cropped square marked with a pink line in the top left image (bottom row) of the 3D: (a) true object; (b) reconstructed image from three-wave interference 3D SIM; (c) reconstructed image from our 3D-SIM system; (d) reconstructed 3D image with proposed 2D processing method. Lateral (e) and Axial (f) views of normalized intensity profiles. For both 3D-SIM systems, the lateral modulation frequency was set at $u_m = 0.8u_c = 4.35\ \mu\text{m}^{-1}$.

The restoration method mentioned above [Eq. (8)] is used when the entire 3D image of the object is captured. However, if only some raw 2D images are available, one can approximately restore the object information by 2D processing at each plane using either the 2D generalized Wiener filter [44] or the approach in [41]. The latter works well if only the in-focus information is modulated with the SI pattern, i.e., when the SI pattern is axially confined. This approach is valid if the axial extent of the SI pattern is smaller than or

comparable to the depth of field of the imaging lens used. In our current implementation, both values are equal; the theoretical depth of field (λ/NA2) for the 20×/0.5 NA objective lens is 2.06 μm and the axial extent of the pattern for 9 slits is 2.1 μm (Fig. 20). Therefore, using a similar approach as the one in [41] we compute a new dataset of forward images in which the out-of-focus information has been removed. Using these pre-processed raw SIM images, we obtain the final restored image by applying the same process of demodulation, shifting and combining of the retrieved frequency components as before [44] but without the final deconvolution. The pre-processing is based on the method in [41] but our approach in computing components that are mathematically equivalent to the ones reported in Eqs. (4) and (5) of [41] is different. In our approach, we first deconvolve each 2D raw image by applying a 2D Wiener filter with the non-aberrated 2D PSF at the best focal plane to remove the diffraction effects of the PSF [79]. Note that each deconvolved raw image $g'(\boldsymbol{x})$ is still expressed by the sum of three unknown components, $\{d_n'(\boldsymbol{x},z)\}$, which are then decomposed by solving a set of linear equations to provide the unmodulated part, $d_0'(\boldsymbol{x},z)$, and the in-focus optically-sectioned demodulated content, $\mathrm{e}^{-\mathrm{i}2\pi u_m x} d_{+1}'(\boldsymbol{x},z)+\mathrm{e}^{\mathrm{i}2\pi u_m x} d_{-1}'(\boldsymbol{x},z)$.

Fig. 23(d) shows the 3D restored image of the numerical test object obtained by stacking all the transverse planes after applying the 2D processing method. The regularized parameter in the 2D Wiener filtering of step 1 of the method was empirically determined to be equal to 0.05. Interestingly, the zoomed view of the cropped square in the *xy*-section image from this 3D restored image (Fig. 23(d), bottom row) shows qualitative improvement over the result obtained with the 3D processing method (Fig. 23(c) bottom

row). However, as expected the 3D method provides better axial performance than the 2D processing method. A comparison of the intensity profiles through the center of the restored images discussed in this section [Fig. 23(e) and (f)] confirms qualitative observations.

3.3. Proof-of-concept experimental results

In this section, we present reconstructed images obtained from three proof-of-concept experimental datasets recorded using a 20×/0.5 NA dry objective lens. The 3D SI pattern was generated using 9 slits and the position of the Fresnel biprism was set at η = 56 mm to achieve the highest lateral and axial modulation frequencies, $u_m = 0.8u_c = 1.55\ \mu m^{-1}$ and $w_m = 0.049\ \mu m^{-1}$, respectively. Results from the proposed 3D-SIM system are also compared to results obtained from the same test samples with a commercial incoherent grid-projection system [10] (ApoTome.2 SIM module on a Zeiss AxioImager.Z2 upright available in our laboratory) to validate its performance. To acquire the 3D dataset of the sample under research with the commercial ApoTome-SIM system, we used the L-illumination grating, which provides the highest available lateral modulation frequency ($u_m = 0.14u_c = 0.27\ \mu m^{-1}$), and an axial scanning interval equal to 0.3 μm. The final 3D image from the commercial system was restored using the ApoTome deconvolution method (Zeiss ZEN.2 software [59]).

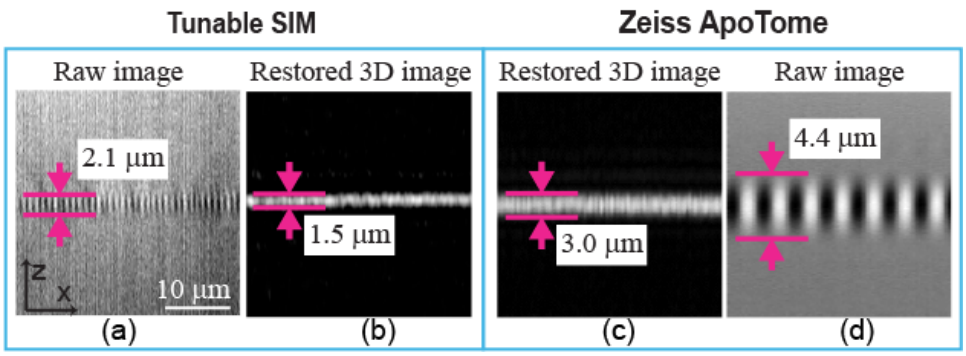

Fig. 24. Achieved OS capability verified with experimental images of an axially-thin fluorescent layer: *xz*-sections of the raw (a and d) and restored SIM image (b and c) from the tunable 3D-SIM ($u_m = 0.8u_c$) and the ApoTome-SIM ($u_m = 0.14u_c$) systems. Because ApoTome processing does not consider the widefield component, which is equivalent to the $\hat{D}_0(\cdot)$ component [Eq. (8)], we neglected this term when computing the restored image in the case of our system (b) for a fair comparison. In panels (a) and (d), the pink arrows indicate the axial extent of the SI pattern, quantified by the value shown on each image. The pink arrows in panels (b) and (c) quantify the FWHM of the integrated intensity, obtained by averaging the intensity values along its lateral coordinate for each restored image.

The first experiment evaluates the OS capability of our system. The OS capability was evaluated using the integrated intensity [23], which relates the total power in out-of-focus planes with the power in the in-focus plane. Experimentally, the integrated intensity is measured by axially scanning an axially-thin fluorescent layer in the object space. Fig. 24 shows *xz*-section images from an axially-thin fluorescent layer. As evident from these images our SIM implementation [Fig. 24(a)] can operate like the ApoTome system [Fig. 24(d)] because it has a confined SI pattern but with a 40% reduced axial extent due to the larger modulation frequency that can be used in our system compared to the ApoTome system. Since fewer transverse sections of the sample are modulated by the SI pattern, our 3D-SIM system can provide better discrimination of the out-of-focus light than ApoTome SIM. The corresponding reconstructed images of the fluorescent layer in Fig. 24(b) and (c) allow quantitative comparison of the OS capability of the two systems using the integrated

intensity (computed by averaging the intensity values along the lateral coordinate for each axial position of the layer). The measured FWHM of the integrated intensity is 1.5 µm and 3 µm for the proposed 3D-SIM and ApoTome-SIM systems, respectively. Because the narrower the integrated intensity, the highest the OS capability, one can conclude that our system determines more accurately the layer's axial position than the commercial ApoTome-SIM system.

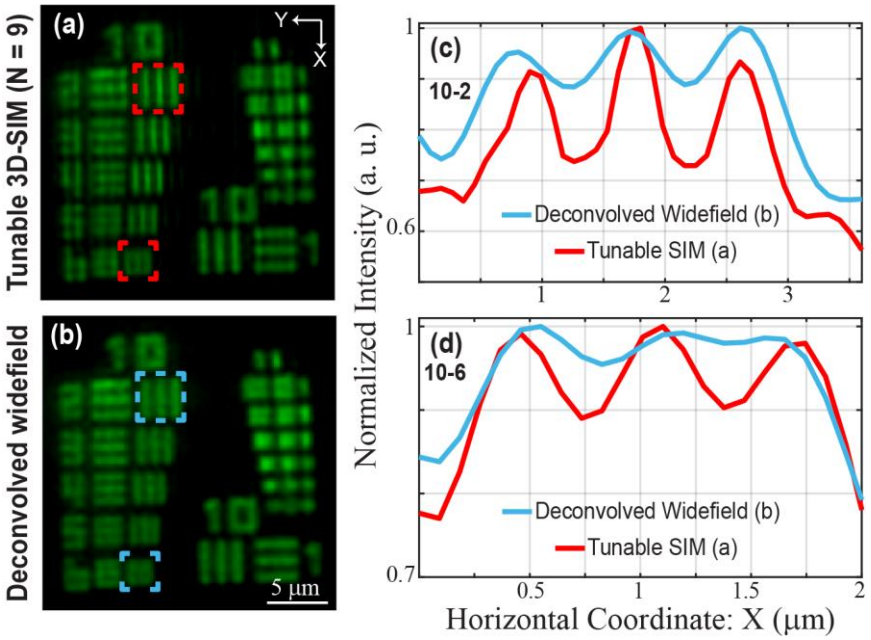

Fig. 25. Achieved SR verified in experimental images of the fluorescent USAF target: (a) Reconstructed SIM image for $u_m = 0.8u_c$ and (b) Synthetic deconvolved widefield image. (c) and (d) Normalized intensity profiles through the center of the vertical elements 10-2 and 10-6, marked by the dashed rectangles in (a) and (b), from both images.

The achieved SR capability of our system is validated experimentally with SIM mages acquired from an extreme USAF target (Ready Optics, Calabasas, California) whose metallic surface was painted with fluorescent dye. Fig. 25 shows the reconstructed SIM image [Fig. 25(a)] and the deconvolved synthetic widefield image (obtained from the zero-

order component) [Fig. 25(b)]. The smallest resolved element of group 10 in Fig. 25(a) and (b) provides the lateral resolution limit achieved in each case. The resolution has been increased from 1149 lp/mm (element 2 of group 10) in the deconvolved synthetic widefield image) to 1825 lp/mm (element 6 of group 10) in the image from our 3D-SIM system. Note that the corresponding resolvable distance of these elements is 435 nm and 274 nm, respectively. Normalized intensity profiles along the horizontal direction through the center of these vertical elements of group 10 [10-2 and 10-6 marked by the dashed rectangles in Fig. 25(a) and (b)] from both images are plotted in panels (c) and (d), respectively, to confirm the resolution limit in each case. As it is expected, the use of the SIM technique almost doubles the resolution limit of the native system when the lateral modulation frequency of the SI pattern is close to the cutoff frequency of the imaging system ($u_m = 0.8u_c$). Particularly, the smallest resolvable distance has been reduced by a factor of 1.8 (from 515 nm, which is the diffraction limit for an emission wavelength of λ = 515 nm and an imaging lens' NA = 0.5, to 274 nm) for the native system and 1.6 (from 435 nm to 274 nm) after applying deconvolution. Note that the lateral SR performance of our proposed 3D-SIM system is comparable with the performance of a standard 3D-SIM system. From the spectrum shown in Figs. 3(a) of [80], one can estimate that the lateral resolution of a commercial Zeiss Elyra PS.1 system has been improved by a factor of 1.7, which would correspond to a lateral modulation frequency of $u_m = 0.7u_c$ independent of the objective lens used.

Finally, in our last experiment, simultaneous OS and SR capabilities are verified using a tilted fluorescent USAF target. The induced tilt is ~6.5 degrees with respect to the optical axis to create an object with axial variability. Fig. 26 shows experimental raw SIM images

obtained at three different axial positions of the target using our 3D-SIM system. As expected, the SI pattern is visible only where the tilted USAF target is in-focus in each transverse plane image.

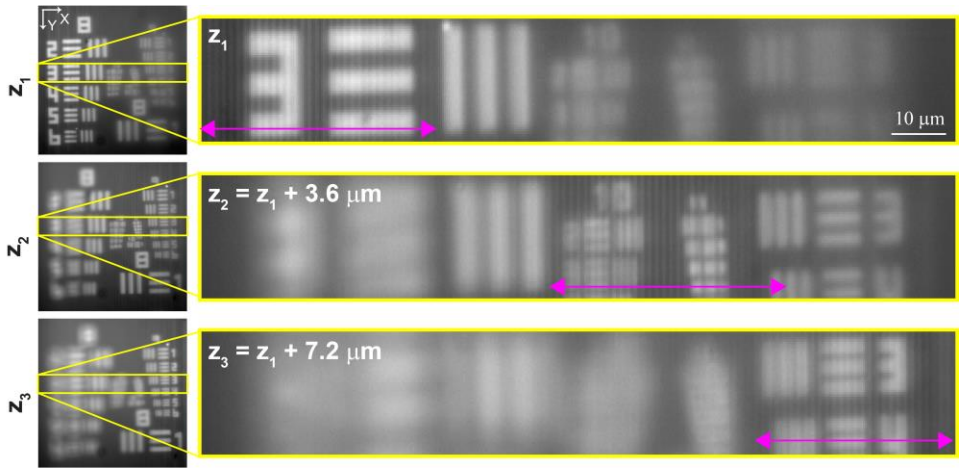

Fig. 26. Experimental raw images of a titled fluorescent USAF target at three different axial positions (z_i). Note that the fringes are visible only in the region of the FoV where the target is in-focus, marked by the pink double arrow in the zoomed versions of the areas marked by the yellow rectangles in the images shown on the left.

The experimental 2D raw images for these three axial positions (Fig. 26) in our system have been reconstructed using the 2D processing method described in Sect. 2.4 (see results in Fig. 27). To quantify the achieved OS we determine the reduction in the out-of-focus information by computing and comparing the integrated intensity inside the different magenta rectangles illustrated in Fig. 27(a) and (b). Note that different elements are marked by the rectangles in each focal plane to assess regions where we do not expect in-focus information such as: the vertical elements of group 8 in the first column, the numbers and horizontal elements of group 8 in the second column, and the groups 10 and 11 in the last column. Fig. 27(a) shows the synthetic raw widefield image (e.g., the estimated widefield image from the raw SIM data without applying any deconvolution method), which contains

out-of-focus information since the imaging system does not have any OS capability. Nonetheless, in the reconstructed image from tunable 3D-SIM system [Fig. 27(b)] the out-of-focus information has been reduced by at least 70%.

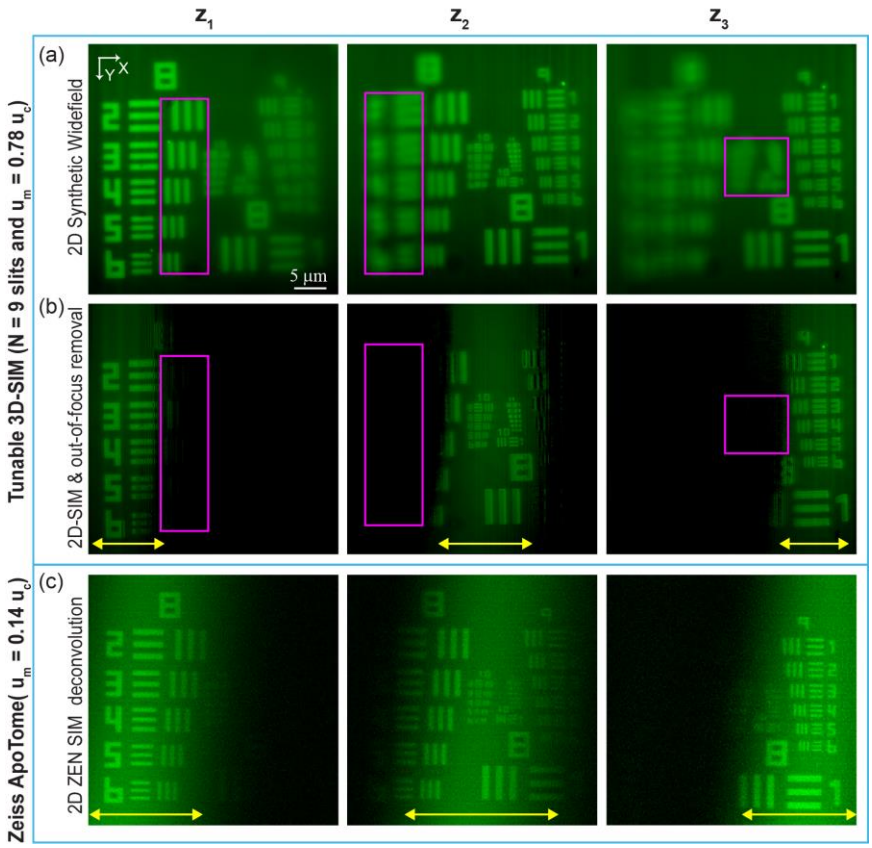

Fig. 27. Experimental verification of simultaneous OS and SR achieved with our tunable 3D-SIM system by imaging a tilted fluorescent USAF target. *xy*-sections images obtained at three different axial locations of the target: (a) Synthetic raw widefield images; (b) Reconstructed SIM images from our systems using 2D processing (Sect. 3.2.4); (c) Reconstructed ApoTome-SIM images using the Zeiss ZEN.2 software. The corresponding magenta rectangles in (a) and (b) highlight the reduction of out-of-focus light achieved in the tunable 3D-SIM system image (b) compared to the conventional widefield image (a). The rectangles highlight different regions of the FoV in which in-focus information is not expected in each axial location of the tilted target. The yellow arrows indicate the lateral extent of the FoV reconstructed in the final image. The images in each case (a), (b) and (c) are displayed using a separate color scale. However, the group of three images in (a), (b), and (c), respectively, are displayed using a global minimum and maximum intensity mapped to the same color scale to show relative intensities in different axial planes. Lens: 20×/0.5 NA dry lens; Emission wavelength: 515 nm. Lateral modulation frequency: $u_m = 0.8u_c = 1.552\ \mu m^{-1}$ for the tunable 3D-SIM system and $u_m = 0.14u_c = 0.27\ \mu m^{-1}$ for the commercial ApoTome-SIM system.

To finalize this study, we compared the restored images from this tilted object obtained with our proposed SIM system [Fig. 27(b)] and the Zeiss ApoTome system [Fig. 27(c)]. The portion of the retrieved information for each transverse section, marked by the yellow arrows in panels (b) and (c) of Fig. 27, is narrower in the images from our system than in the ones from the ApoTome-SIM system. In fact, the reconstructed FoV in the images shown in Fig. 27(c) is larger than those in Fig. 27(b) by a factor of 1.56×, 1.63× and 1.65× for the three different transverse positions (z_i). This restored FoV is proportionally related to the axial extent of the SI pattern (Fig. 26). As expected, the narrower the axial extent of the SI pattern, the narrower the reconstructed FoV in each transverse section and, consequently, the higher the ability of the system to determine the axial position of each lateral feature. Following this reasoning, one could claim that our system provides better OS capability. Note that this conclusion agrees with the result in Fig. 24. Fig. 28 shows the resolution achieved in the tilted USAF target images from our 3D-SIM system. The measured lateral resolution limit ranges between 308 nm and 345 nm, which exceeds the diffraction limit by a factor of 1.5×. Thus, simultaneous OS and SR capabilities of our 3D-SIM system are verified with this experiment.

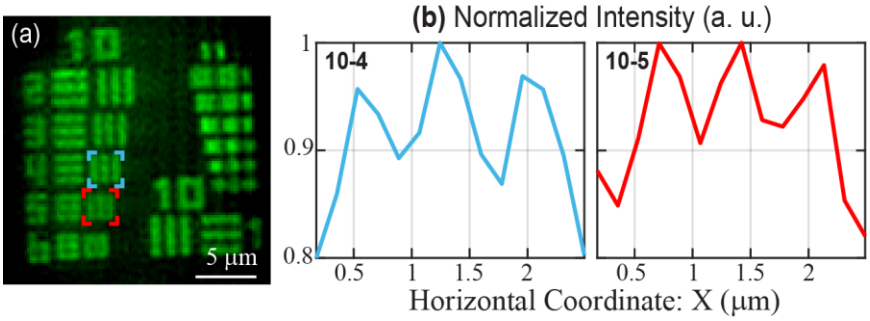

Fig. 28. Verification of the lateral SR capability in the experimental image of the tilted fluorescent USAF target: (a) zoomed version of the groups 10 and 11 in the reconstructed SIM image obtained at the axial location z_2 in Fig. 27(b). (b) Normalized intensity profiles through the center of the vertical elements 10-4 and 10-5, marked by light blue and red dashed rectangles, along the horizontal direction.

3.4. Conclusion

In this work an incoherent-based 3D-SIM system that provides high-contrast structured illumination patterns localized at discrete axial planes was presented and its performance was investigated numerically and experimentally. The 3D SI pattern in this system is generated by illuminating a Fresnel biprism using the emerging light coming from multiple spatially-incoherent slits. An advantage of the system is that both lateral and axial periodicities of the 3D fringes can be tuned independently, providing axial SR capability independent of the lateral SR performance. While both lateral and axial periodicities of the pattern can be continuously tuned by axially displacing the biprism, the axial periodicity of the pattern can be independently tuned by the choice of the slits' separation (x_0). A more detailed study of this axial tunability will be reported in a future publication. Here, we provide proof-of-concept studies using a low-NA implementation and for the particular design of $N = 9$ slits and $x_0 = 100\ \mu\text{m}$. In the investigated studies, we showed that the narrower the axial extent of the fringes, the better discrimination of out-of-focus light is achieved (improved OS capability) in the final restored image of an axially-thin fluorescent layer. Additionally, the proposed tunable 3D-SIM system is shown to provide an increase in the lateral resolution limit by a factor of 1.8× compared to the native system, which is comparable with the performance of a commercial 3D-SIM system [80], and improved OS capability by a factor of 1.6× compared to the ApoTome-SIM system. Nonetheless, the main hallmark of the proposed 3D-SIM system is that it requires fewer images for the final restoration than the three-wave interference 3D-SIM system, which is the standard, while the performance of both systems appears to be comparable based on the compact support of the synthetic OTF comparison and numerical results from reconstruction of simulated

data. Note that our final SIM image is restored using 40% less data since only three phase-shifted images are needed per orientation of the pattern, as opposed to the five images required by the standard 3D-SIM system. Although we have not rotated the 3D SI pattern to achieve isotropic resolution improvement, the pattern can be rotated by jointly rotating the slits' element and the Fresnel biprism or, in a more practical way, by inserting a Dove prism [81] in the SI system and rotating it. To avoid the mechanical movement of the Dove prism, one could use an acousto-optic Dove prism [82]. Because the approaches to provide the needed phase shifting and the rotation of the SI pattern are already available, and implemented in commercial 3D-SIM systems, we believe that a commercial prototype of our tunable 3D-SIM system (e.g. with similar components as those used in commercial 3D-SIM systems) should operate 40% faster than commercially-available systems due to the 40% reduction in the data required for restoration. Additionally, by taking advantage of symmetries and redundancies, we expect that a reduction in the number of images, required for isotropic resolution, from 9 to 4 could also be possible, and future studies will investigate this additional data reduction to make our tunable 3D-SIM system better suited for live-cell imaging.

Funding

National Science Foundation (DBI award 1353904, PI: CP); the University of Memphis; Ministerio de Economia y Competitividad, Spain (DPI2015-66458-C2-1-R); Generalitat Valencia (PROMETEOII/2014/072).

Acknowledgement

We thank collaborators S. V. King (St. Jude Children's Research Hospital, Memphis, TN) and M. Martinez-Corral (Univ. of Valencia, Spain) for scientific and technical discussion.

4. OPTICAL TRANSFER FUNCTION ENGINEERING FOR A TUNABLE 3D STRUCTURED ILLUMINATION MICROSCOPE

*This chapter is based on a paper accepted for publication in the **Optics Letters** journal in press (2019).*

Optical transfer function engineering for a tunable 3D structured illumination microscope

Hasti Shabani[1], Ana Doblas[1], Genaro Saavedra[2], Chrysanthe Preza[1]*

[1]Computational Imaging Research Laboratory, Department of Electrical and Computer Engineering, The University of Memphis, Memphis, TN 38152, USA

[2]3D Imaging and Display Laboratory, Department of Optics, University of Valencia, Burjassot, E-46199, Spain

*Corresponding author: cpreza@memphis.edu

Abstract: Two important features of three-dimensional structured illumination microscopy (3D-SIM) are its optical sectioning (OS) and super-resolution (SR) capabilities. Previous works on 3D-SIM systems show that these features are coupled. We demonstrate that a 3D-SIM system using a Fresnel biprism illuminated by multiple linear incoherent sources, provides a structured illumination pattern whose lateral and axial modulation frequencies can be tuned separately. Therefore, the compact support of the synthetic optical transfer function (OTF) can be engineered to achieve the highest OS and SR capabilities for a particular imaging application. Theoretical performance of our

engineered system based on the OTF support is compared to that achieved by other well-known SIM systems.

http://dx.doi.org/10.1364/OL.99.099999

Three-dimensional structured illumination microscopy (3D-SIM), in which the structured illumination (SI) pattern varies laterally and axially, has become one of the most effective optical imaging modalities used in biological investigations because of its optical-sectioning (OS) and super-resolution (SR) capabilities. The SI pattern in a 3D-SIM system has been traditionally implemented by interfering three coherent waves (3W-SIM) [14] and recently using a tunable-frequency incoherent illumination based on a Fresnel biprism (tunable-SIM) [16]. It has been demonstrated experimentally that 3W-SIM can double both the lateral and axial resolution limits while providing OS capability [14]. As expected, the choice of the lateral modulation frequency of the SI pattern in 3W-SIM determines the final performance (i.e., achieved lateral and axial SR and OS capabilities) because in 3W-SIM the axial and lateral modulation frequencies are coupled. Therefore, the system's performance would be compromised if the highest lateral modulation frequency cannot be used (e.g., when an optically thick sample is imaged the contrast of the SI pattern can be severely reduced necessitating the use of a lower modulation frequency [83,84]). We have recently shown that the 3W-SIM and the tunable-SIM systems have comparable performance at the highest possible modulation frequency by noisy simulation of a particular numerical object used in this study [16]. However, the lateral and axial modulation frequencies of the tunable-frequency 3D pattern can be controlled separately by system parameters, which is not the case in the 3W-SIM system. This unique property

allows us to engineer the synthetic OTF of the tunable-SIM system for a desired imaging application.

In this Letter, we investigate the performance of our novel tunable-SIM system [16] based on the achieved extension of the compact support of its synthetic optical transfer function (OTF), which is controlled by system parameters. These parameters can be chosen to design the pattern and thereby engineer the synthetic OTF. To our knowledge, this is the first 3D-SIM setup that enables independent control of the achieved OS and SR capabilities. The analysis of the system's performance is evaluated through its synthetic OTF. Based on the approach previously used to derive 2D-SIM synthetic OTF [23], we formulate the synthetic OTF of a 3D-SIM system, $H_{\mathrm{SIM}}(\mathbf{u}, w)$, when the 3D SI pattern is separable into a transverse and axial function (as it is the case for the 3W-SIM and tunable-SIM systems), as

$$H_{\mathrm{SIM}}(\mathbf{u}, w) = H(\mathbf{u}, w) \otimes_3 I(\mathbf{u}, w), \tag{1}$$

where $\mathbf{u} = (u, v)$ and w are, respectively, the lateral and axial spatial frequency coordinates, $H(\mathbf{u}, w)$ is the conventional OTF, and $I(\mathbf{u}, w)$ is the Fourier transform (FT) of the 3D SI pattern. In our tunable-SIM system, axially-localized high-contrast sinusoidal patterns are generated by incoherent overlapping of axially-extended interference patterns produced by a set of equidistant parallel incoherent linear sources (slits) and a Fresnel biprism [16]. This incoherent superposition produces a 3D SI pattern that is axially periodic. The 3D SI pattern in the sample volume is given by [16]:

$$i(\mathbf{x}, z) \approx 1 + \mathcal{V}(z) \cos(2\pi u_m x + \varphi), \tag{2}$$

where $\mathbf{x} = (x, y)$ and z denote the lateral and axial coordinates, respectively, φ is the phase of the SI pattern shifted by laterally translating the Fresnel biprism [16], and

$$\mathcal{V}(z) = \frac{\sin(2\pi N w_m z)}{N \sin(2\pi w_m z)}, \tag{3}$$

defined as the visibility function [16], depends on the number of slits N, and on the lateral and axial modulation frequencies, $u_m = \frac{2\eta(n_F - 1)\tan\delta}{\lambda f_{L1} M_{ill}}$, and $w_m = \frac{x_0 u_m}{f_{L1} M_{ill}}$, respectively, determined by system parameters (Fig. 1 in Ref. [16]): excitation wavelength (λ), biprism position (η), focal length of the first converging lens (f_{L1}), lateral magnification of the illumination system (M_{ill}), biprism refringence angle (δ) and refractive index (n_F), and the distance between two neighboring slits (x_0). Although Eq. (2) shows the lateral modulation only in one direction, modulation in other lateral directions can be achieved by rotating the 3D SI pattern laterally [16].

As mentioned earlier, the lateral and axial modulation frequencies of the 3D SI pattern can be controlled separately. The lateral modulation frequency (u_m) can be tuned, up to the effective cutoff frequency of the system ($u_{c-eff} = 0.8u_c$, in which u_c is the cutoff frequency of the WFM), by axially changing the position of the Fresnel biprism (η) w.r.t. the slits' plane. Although the axial modulation frequency (w_m) depends on u_m, it can be tuned independently by selecting x_0 in the design of the slits element while keeping u_m constant. The space and frequency representations of our tunable 3D pattern [Eq. (2)] are shown in Fig. 29(a) and (c), respectively. The blue profile plotted in Fig. 29(a) represents

the absolute value of the visibility function [Eq. (3)]. We observe that the fringes' visibility is a periodic function that takes its maximum value [$\mathcal{V}(z)=1$] at a discrete set of axial planes, referred to as the resonant planes. The separation between two resonant planes, $T=\frac{1}{w_m}$, is inversely proportional to η and x_0 but independent of N [Fig. 29(a)]. On the other hand, the axial extent of the fringes [$\Delta z=\frac{2}{Nw_m}$], defined by the region around the resonant planes in which $\mathcal{V}(z)=0$, decreases with increasing N, x_0, and η. Note that the FT of Eq. (3), $V(w)$, is given by:

$$V(w)=\frac{1}{N}\sum_{n=0}^{N-1}\delta\left[w-\left(2n-N+1\right)w_m\right]. \tag{4}$$

Inserting the FT of Eq. (2) in Eq. (1), the synthetic OTF of the tunable-SIM system can be expressed by:

$$H_{\mathrm{SIM}}(\mathbf{u},w)=H(\mathbf{u},w)+\sum_{n=0}^{N-1}\frac{H\left[u\pm u_m,v,w-(2n-N+1)w_m\right]}{2N}, \tag{5}$$

which is the sum of the conventional widefield fluorescence microscope (WFM) OTF and two new components, each composed by the sum of N axially-shifted replicas of the conventional OTF separated by $2w_m$, that are shifted laterally by $\pm u_m$ [Fig. 29(d)]. Note that the number and the location of the replicas in the synthetic OTF [Fig. 29(c)] change with the number of slits (N) and the distance between two neighboring slits (x_0), respectively. However, there is still one single lateral modulation frequency (u_m) for all the replicas. Therefore, only 3 images per orientation of the SI pattern are needed to

reconstruct SR images with the tunable-SIM system, independent of the number of slits (N) or other system parameters (N , x_0). Taking advantage of the independent tuning of u_m and w_m, it is possible to engineer the synthetic OTF's compact support by selecting parameters (N , x_0, η) for a specific SI design.

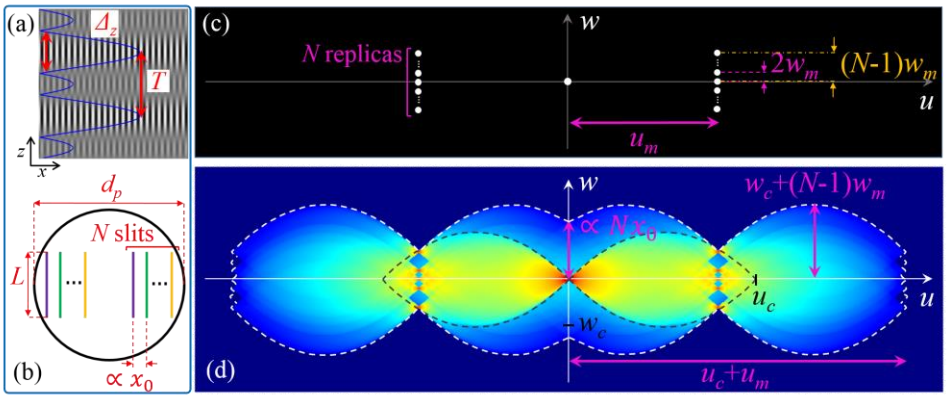

Fig. 29. Relation of the SI design and synthetic OTF of the tunable-SIM system. (a) *xz*-section of 3D SI pattern and $|\mathcal{V}(z)|$ (blue curve) of Eq. (3). (b) Schematic of the slits-element image at the back focal plane of the objective lens. (c) *uw*-section of the 3D pattern's FT. (d) *uw*-section of the synthetic MTF for $u_m = u_{c-eff} = 0.8u_c$. OTF compact support for WFM and tunable-SIM shown by black and white dashed lines, respectively.

Because it is desired to operate at the highest lateral SR performance, the η-parameter should be fixed to provide SI fringes with the highest lateral modulation frequency $u_m = u_{c-eff} = 0.8u_c$ (this is also the highest frequency usable for 3W-SIM as demonstrated in [80]). This is because at this frequency, the fringes' contrast is attenuated by a factor of 0.1 due to the incoherent detection OTF for fluorescence imaging [75]. Fig. 29(d) shows the *uw*-section image of the synthetic modulation transfer function (MTF), absolute modulus of the OTF, of our tunable-SIM system, for the general case of N slits (separated by a distance x_0). From this figure, one realizes that both lateral and axial OTF compact

support (white dashed line) have been extended compared to the compact support of the conventional OTF (black dashed line). Note that the lateral and axial resolution limits [pink arrows in Fig. 29(d)] have been increased by a factor of $1+(u_m/u_c)$ and $1+\left[(N-1)(w_m/w_c)\right]$, respectively, where $u_c=\frac{2\mathrm{NA}}{\lambda}$ and $w_c=\frac{\mathrm{NA}^2}{2n\lambda}$ are the lateral and axial cutoff frequencies of the WFM system, respectively. Note that NA is the lens' numerical aperture and n is the refractive index of the lens' immersion medium. In addition to the lateral and axial extension of the OTF, Fig. 29(d) shows that the upper portion of the missing cone of frequencies in the conventional OTF is filled by *N*/2 axially-shifted WFM OTF replicas, with axial separation between two neighboring replicas equal to $2w_m$. Therefore, the amount of the missing cone that has been filled is quantified by Nw_m. This means that: (1) the higher the number of slits and/or (2) the larger the separation between two neighboring OTF replicas (i.e., larger w_m), the better the OS capability of the system. Because w_m is proportional to x_0, the product Nx_0 can be used as a metric in the synthetic SIM-OTF engineering. It is worth realizing that this metric, Nx_0, is related to Δz in the reciprocal space; a smaller Δz allows greater discrimination of out-of-focus information.

As mentioned earlier, increasing the number of slits (N) provides higher axial SR and better OS capability. However, in a realistic experiment, one cannot increase the number of slits *at will*. There is an upper limit for the *N*-value determined by the pupil's diameter (d_p) of the objective lens used, given by

$$N_{\max} = 1 + \left(1 - \frac{u_m}{u_c}\right) \frac{f_{L1}\sqrt{d_p^2 - L^2}}{f_{L2} x_0}, \tag{6}$$

where L is the slits' length at the pupil plane and needs to fit entirely within the aperture stop of the objective lens [Fig. 29(b)] to avoid clipping of the slits' image and consequently, fringes with reduced contrast [16]. For example, the maximum number of slits for a 20×/0.5NA dry objective lens is $N_{\max} = 9$, assuming $x_0 = 100\ \mu$m, $u_m = 0.8u_c$ and a lateral magnification between the slits and pupil planes of $M = -f_{L2}/f_{L1} = -2.5$.

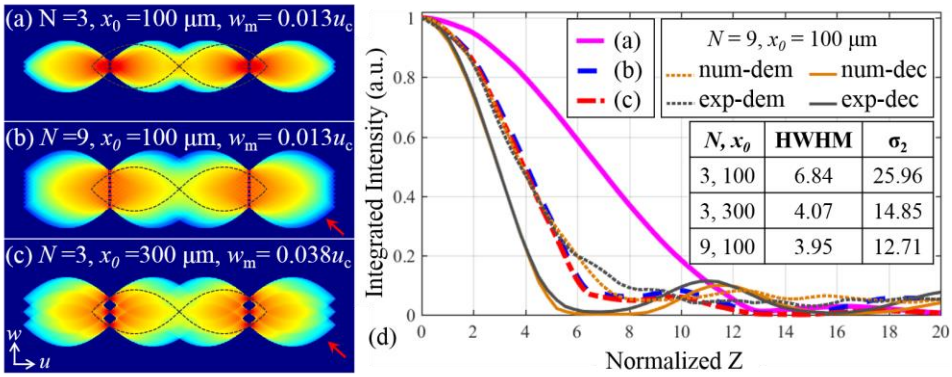

Fig. 30. The impact of slits' parameters (N and x_0) on the synthetic OTF's compact support and OS capability of the tunable-SIM system. (a-c) *uw*-section of the synthetic MTF for different designs; (d) Integrated intensity profiles of (a-c), experimental (exp) and numerical (num) results. Legends: 'dem' and 'dec' stand for demodulation and deconvolution, respectively. For this study we used $u_m = u_{c-eff} = 0.8u_c$.

Fig. 30(a) and (b) show the synthetic MTF for two different numbers of slits, where the image intensities are normalized and mapped to the same color scale [a similar intensity normalization is used in Fig. 31 and Fig. 32]. From these panels one realizes that the lateral cutoff frequency of the synthetic OTF is invariant with the N-value and always remains at the maximum value of $2u_{c-eff}$. On the other hand, the axial cutoff frequency increases with

the number of slits. Particularly, the axial resolution increases by a factor of 1.5× when the number of slits is increased from $N = 3$ [Fig. 30(a)] to 9 [Fig. 30(b)].

The OS capability is investigated through the integrated intensity function [Fig. 30(d)], which forms a Fourier-pair [23] with the axial OTF, $H(\mathbf{u} = 0, w)$, in any imaging system. Because the first term in the right-hand side of Eq. (5) is the WFM OTF and it lacks OS capability, in what follows we compute the integrated intensity profiles by neglecting this term. In addition, the axial distance is normalized by $4k\sin^2\left[\sin^{-1}(\mathrm{NA}/n)/2\right]$, where $k = 2\pi/\lambda$ is the wave vector in the lens' immersion medium of refractive index *n*. As expected, the system using 9 slits provides better OS capability (narrower integrated intensity) compared to the systems with $N = 3$. This is quantified by measuring the half width at half maximum (HWHM) of the integrated intensity profiles [Fig. 30(d)], found to be equal to 6.84 and 3.95 for $N = 3$ and $N = 9$, respectively. The theoretical OS performance of the tunable-SIM system with $N = 9$ slits is validated experimentally and numerically. Fig. 30(d) shows the integrated intensity of the experimental (gray dashed line) and numerical (orange dashed line) demodulated SIM images from an axially-thin fluorescent layer [16]. The OS performance can be further improved by applying deconvolution to the demodulated image [Fig. 30(d), gray and orange solid lines].

Although we have demonstrated that both the axial SR and the OS capability improve by increasing the number of slits, it is interesting to point out that similar OS performance can be achieved for a lower number of slits if the product between N and x_0 is kept constant. Fig. 30(b) and (c) show the synthetic OTF's compact support and the integrated intensity for two different cases in which Nx_0 = 900 μm. Note that although Nx_0 is fixed,

the axial modulation frequency w_m is different for each case providing a different axial SR. Although the difference in the HWHM values of the integrated intensity profiles for these two cases is negligible (< 4%), some difference in the secondary lobes of the integrated intensity curves is evident [Fig. 30(d)], and it is quantified by the normalized second order moment (σ_2), which classically it has been used to assess the global width of a function [85]. Considering both the HWHM and σ_2 metrics, then the system with the best OS performance is the one with a slit element of $N = 9$ and $x_0 = 100\ \mu$m [Fig. 30(d)]. Another difference is the attenuation of the frequencies located at the border of the synthetic OTF (regions indicated by red arrows in Fig. 30(b) and (c), which is less for the design with $N = 3$ and $x_0 = 300\ \mu$m. This attenuation is related to the 1/*N* factor in Eq. (5) and it potentially renders the system more sensitive to noise at high frequencies for higher *N*-values. Thus, there is a tradeoff between the optimal slits-element design (N and x_0) and the system's robustness to noise.

Theoretical predictions of the SR and OS capabilities of the tunable-SIM system are compared with the ones achieved by other well-established systems: the 3W-SIM [14], the incoherent grid-projection OS-SIM [10] and the confocal microscope [17]. For the case of the OS-SIM system, we have considered the highest theoretical lateral modulation frequency $u_m = 0.5u_c$ that can be used [10]. Regarding the confocal scanning system, we assumed an ideal pinhole and that the Stokes shift is 0.8 [23]. To provide an extensive comparison between the 3W-SIM and the tunable-SIM systems, we considered two different lateral modulation frequencies ($u_m = 0.5u_c$ and $u_m = 0.8u_c$), because when imaging optically-thick samples, there is a need to reduce the lateral modulation frequency

to modulate the sample's information [83,84]. In 3W-SIM systems, this reduction has been alleviated by either line scanning the sample laterally [86] or by combining a Bessel beam to the SIM system [87].

The *uw*-section images of the synthetic OTF for the tunable-SIM and 3W-SIM systems are shown in Fig. 31(a-e). From these images, one can realize that both systems provide the same lateral SR improvement for the same lateral modulation frequency of the SI pattern. However, the axial SR and OS capabilities are different depending on the lateral modulation frequency. Note that for each chosen slit element design of the tunable-SIM system, we determine the maximum distance between two neighboring slits (x_0) for a specific N and u_m using Eq. (6). For $u_m = 0.8u_c$, the synthetic OTFs of both 3D-SIM systems [Fig. 31(a) and (b)] have the same axial extension and thereby, both systems provide the same SR improvement along the lateral and axial directions. Notwithstanding, the OS capability is slightly different as one realizes from the integrated intensity curves [Fig. 31(f)]. Depending on the metric used, the HWHM and the normalized second order moment (σ_2) of the integrated intensity, one could conclude that either the 3W-SIM system or our 3D-SIM system provides the highest OS capability. Nonetheless, overall, the OS capability of both systems operating at $u_m = 0.8u_c$ is quite comparable and as expected higher than the one provided by the confocal and incoherent-grid-projection SIM [Fig. 31(f)]. However, we believe that our proposed system could have a significant impact when low and medium lateral modulation frequencies are needed. Fig. 31 shows that the tunable-SIM system (with either SI design) operating at $u_m = 0.5u_c$ presents the highest axial SR (axial OTF extension of $w_c + 0.144u_c$) and OS capabilities among all investigated systems.

Therefore, designing the slit element we can engineer the frequency response of our system to always operate at the highest performance for a given imaging application.

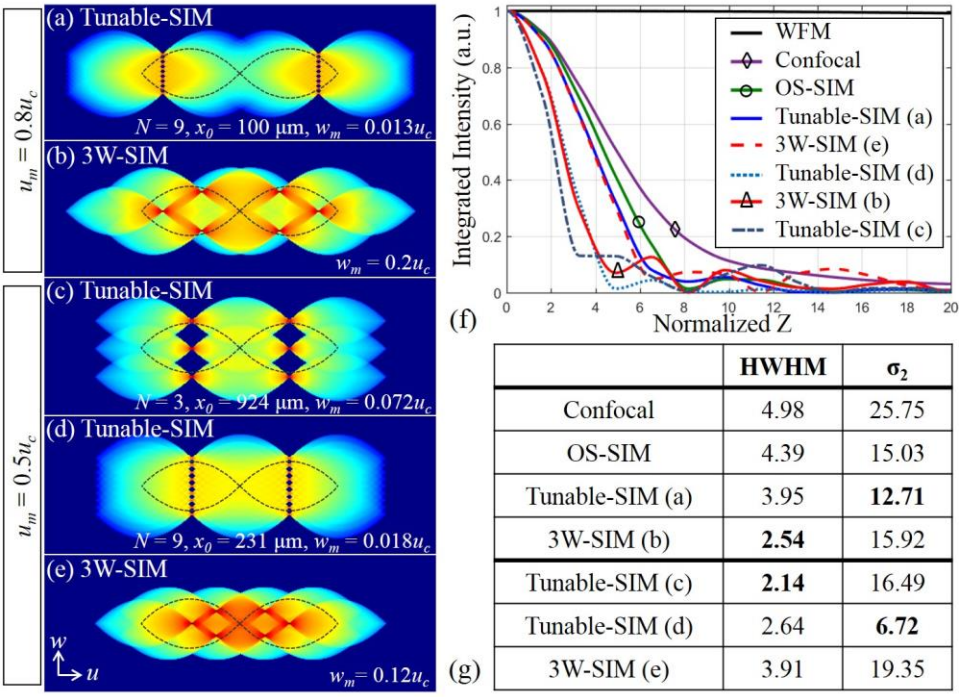

	HWHM	σ_2
Confocal	4.98	25.75
OS-SIM	4.39	15.03
Tunable-SIM (a)	3.95	**12.71**
3W-SIM (b)	**2.54**	15.92
Tunable-SIM (c)	**2.14**	16.49
Tunable-SIM (d)	2.64	**6.72**
3W-SIM (e)	3.91	19.35

Fig. 31. Comparison of different systems' performance. (a-e) *uw*-section of the synthetic MTF for tunable-SIM and 3W-SIM systems at different designs. (f) Integrated intensity profiles obtained from the MTF of systems: (a)-(e); OS-SIM ($u_m = 0.5u_c$); confocal microscope; and WFM. (g) HWHM and σ_2 values computed from integrated intensity curve.

Finally, we study how noise affects both 3D-SIM systems as their synthetic OTFs have a different strength. In fluorescent imaging, shot noise is the dominant noise source and is considered to be Poisson distributed [88]. For this study, the image of a sub-resolved bead, which represents the WFM point spread function (PSF), was scaled to mimic a specific photon count and it was used to generate Poisson noise. Since this model for the noise is spatially variant, the global noise level, as quantified by the signal to noise ratio (SNR), is computed by taking the average over the whole PSF. According to Poisson statistics, this

value corresponds to the mean of the squared root of the intensity at each pixel in the 3D image. A noisy WFM MTF was generated by taking the absolute value of the FT of the noisy WFM PSF. The noisy synthetic SIM MTF was then generated from the noisy WFM MTF using Eq. (5) for the tunable-SIM case while for 3W-SIM Eq. (1) with corresponding SI pattern was used instead. Fig. 32(a-d) shows the noisy synthetic MTFs (the average of a 100-realizations ensemble) of two designs of the tunable-SIM and the 3W-SIM systems for two modulation frequencies and at two different SNR levels. The noise effect is quantified by determining the effective lateral and axial cutoff frequencies as the limiting frequencies at which the noiseless synthetic MTF value falls below a threshold. The threshold was set equal to the background mean of the noisy synthetic MTF beyond the noiseless axial and lateral cutoff frequencies. As shown in Fig. 32(e) and (f), although both systems perform equally well for a high SNR (>20 dB for $u_m = 0.8u_c$ and >15 dB for $u_m = 0.5u_c$), their performances are different for low SNR. For SNR = 10 dB and $u_m = 0.8u_c$, there is a 12% and 20% reduction in the effective axial cutoff frequency in the 3W-SIM and tunable-SIM, respectively [Fig. 32(f)], while the reduction in the effective lateral cutoff frequency is less in the tunable-SIM [e.g., 13% and 17% reduction for tunable-SIM and 3W-SIM, respectively, in Fig. 32(e)]. This is because the different arrangement of the WFM OTF replicas results in a different synthetic OTF value in each system. On the other hand, for $u_m = 0.5u_c$, although the 3W-SIM system performs slightly better laterally for SNR <10 dB, (e.g. 36% and 45% reduction in the effective lateral frequency for 3W-SIM and tunable-SIM, respectively, when SNR = 5 dB), the tunable-SIM system outperforms 3W-SIM at all SNR levels with axial resolution improvement by a factor of 2.2× compared to the 1.6× improved achieved by the 3W-SIM system.

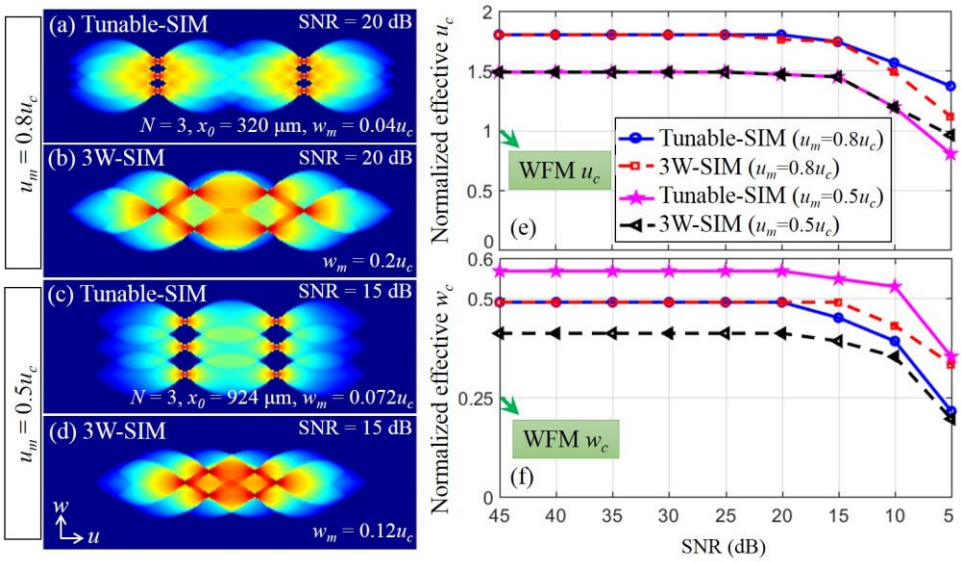

Fig. 32. Performance of two 3D-SIM systems under noisy conditions. *uw*-section of the synthetic MTF for tunable-SIM and 3W-SIM systems for (a-b) SNR = 20 dB and (c-d) SNR = 15 dB. Effective lateral (e) and axial (f) cutoff frequencies for different SNR levels.

In summary, we presented a unique tunable SI system that can be engineered for use in a 3D-SIM system that provides 40% reduction in data-acquisition compared to the 3W-SIM system [16]. Here we investigated different SI designs in terms of the OS and SR capabilities of the tunable-SIM system and show that the lateral and axial modulation frequencies of this SI pattern can be controlled separately by system parameters. This unique property allows us to engineer the synthetic OTF of the system for a desired imaging application by designing the slit element, so that our 3D-SIM system operates at the highest axial SR and OS capabilities even though the lateral SR must be reduced. We believe that our system will have a high impact in those biological imaging applications where the highest lateral modulation frequency cannot be used due to a reduction in the SI pattern's contrast.

Funding

National Science Foundation (DBI award 1353904, PI: CP); the University of Memphis; Ministerio de Economia y Competitividad, Spain (Grant DPI2015-66458-C2-1-R) and Generalitat Valenciana (Grant PROMETEOII/2014/072).

5. THREE-DIMENSIONAL DECONVOLUTION BASED ON AXIAL-SCANNING MODEL FOR STRUCTURED ILLUMINATION MICROSCOPY

Current model-based deconvolution methods for three-dimensional structured illumination microscopy (3D-SIM) assume that the observed image can be modeled as the convolution of the fluorescence emission with the detection point spread function. However, such a model is not suitable when 3D data is acquired using axial scanning of the sample as in the case of commercial microscopes, because the structured illumination (SI) pattern is changing axially. In this chapter, we implement a forward imaging model for 3D-SIM that takes into account specimen axial scanning and develop a 3D model-based (3D-MB) iterative approach to restore the final image by minimizing the mean squared error between the data and the forward images predicted by this model using a conjugate-gradient method. This method is applicable for 3D-SIM systems in which the SI pattern is separable into axial and lateral functions. To our knowledge, such a restoration method has not been published to date. Portions of this chapter appear in a 2019 IEEE ISBI conference paper [47].

5.1. Forward imaging model

In fluorescence imaging, the 3D recorded image of a sample (the observed image), whose 3D irradiance distribution is $g(\boldsymbol{x}, z)$, can be modeled by the following 3D convolution operation:

$$g(\boldsymbol{x}, z) = \left[o(\boldsymbol{x}, z) i(\boldsymbol{x}, z) \right] \otimes_3 h(\boldsymbol{x}, z) + \varepsilon(\boldsymbol{x}, z) \tag{1}$$

where, $\boldsymbol{x}=(x,y)$ and z are the transverse and axial coordinates, respectively, $o(\boldsymbol{x},z)$ is the density distribution of fluorophores within the sample, $i(\boldsymbol{x},z)$ is the irradiance distribution of the excitation illumination, $h(\boldsymbol{x},z)$ is the point spread function (PSF) of the imaging system, $\varepsilon(\boldsymbol{x},z)$ is the additive noise, and $\otimes_3$ stands for the 3D convolution operator.

However, this model [Eq. (1)] is not always valid for 3D-SIM depending on the 3D data-acquisition configuration. In advanced multi-focus acquisition microscopes where the images of the sample at various axial positions are recorded without any sample translation, the convolution model of Eq. (1) is appropriate. Recently, such multi-focus microscopes have been practically demonstrated using diffractive optical elements or beam splitters to image multiple focal planes [89,90]. However, most SIM commercial microscopes record information from one focal plane at a time and require axial scanning of the object to complete the 3D data acquisition. During this data-acquisition type, every plane of the object is illuminated by a different SI pattern at each axial shifting because the SI pattern is changing axially in a true 3D structured illumination, and thus different planes within the object are not excited by the same illumination; therefore, Eq. (1) is not a valid model for this case. In most WF imaging systems, the 3D recorded image of a sample is acquired by axial scanning the sample with respect to the focal plane of the microscope objective lens. Mathematically, the intensity in the 3D image recorded using axial scanning can be expressed by the following equation:

$$g(\boldsymbol{x},z)=\iint o(\boldsymbol{x}',z'+z)\,i(\boldsymbol{x}',z')\,h(\boldsymbol{x}-\boldsymbol{x}',0-z')d\boldsymbol{x}'dz', \tag{2}$$

assuming that the camera's position is fixed ($z=0$). Equivalently with a change of variables, $z''=z'+z$,

$$g(\boldsymbol{x},z)=\iint o(\boldsymbol{x}',z'')\,i(\boldsymbol{x}',z''-z)\,h(\boldsymbol{x}-\boldsymbol{x}',z-z'')d\boldsymbol{x}'dz''. \tag{3}$$

Equations (2) and (3) are basically the same, the former assumes the object is axially scanned through the illumination while the latter assumes the illumination is scanned through the object, or equivalently representing the physical translation of the sample stage and the microscope objective respectively. Particularly, in a conventional WF microscope the illumination is uniform, $i(\boldsymbol{x},z)=1$ and as a result, Eq. (3) is rewritten as:

$$g(\boldsymbol{x},z)=\iint o(\boldsymbol{x}',z'')\,h(\boldsymbol{x}-\boldsymbol{x}',z-z'')d\boldsymbol{x}'dz''=o(\boldsymbol{x},z)\otimes_3 h(\boldsymbol{x},z). \tag{4}$$

However, in the case of non-uniform structured illumination, the pattern plays an important role in the forward imaging model. Assuming that the SI pattern is separable into an axial function, $i_k(z)$, and a lateral function, $j_k(\boldsymbol{x})$, and that it can be expressed as a discrete sum of a finite number of components, $\boldsymbol{K}$, then the SI pattern can be written as follows (as it is the case for the 3W-SIM [14] and tunable 3D-SIM systems [16]):

$$i(\boldsymbol{x},z)=\sum_{k=1}^{K} j_k(\boldsymbol{x})\,i_k(z). \tag{5}$$

Inserting Eq. (5) in Eq. (3) results in:

$$g(\boldsymbol{x},z)=\sum_{k=1}^{K}\iint o(\boldsymbol{x}',z'')\,j_k(\boldsymbol{x}')\,i_k(z''-z)\,h(\boldsymbol{x}-\boldsymbol{x}',z-z'')d\boldsymbol{x}'dz'', \tag{6}$$

which can be rewritten as follows:

$$g(\boldsymbol{x},z)=\sum_{k=1}^{K}\left[o(\boldsymbol{x},z)\,j_k(\boldsymbol{x})\right]\otimes_3\left[h(\boldsymbol{x},z)i_k(-z)\right]. \tag{7}$$

It is important to realize that the lateral function modulates the object directly while the axial function is in the same axial coordinate with the PSF and thus, it is grouped with the PSF before the convolution operation. Note that the axial function is an even function, therefore we have used $i_k(z)$ instead of $i_k(-z)$ in the rest of the equations without loss of generality. Since the SI patterns in the 3W-SIM [14] and the tunable 3D-SIM [16] are separable into axial and lateral functions, Eq. (7) is a suitable forward imaging model for these SIM systems that employ axial scanning of the sample.

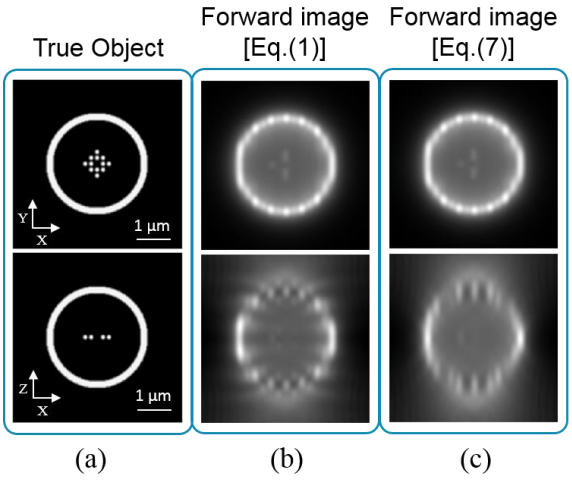

Fig. 33. Forward images of 3W-SIM system based on two different imaging model: one that does not account for axial scanning of the sample [Eq. (1)] and one that does [Eq. (7)]. Lateral view (top row), axial view (middle row) of the 3D: (a) true object; forward image using (b) Eq. (1) , (c) Eq. (7). For the 3D-SIM system, the lateral modulation frequency was set at $u_m = 0.8u_c = 4.35\ \mu\text{m}^{-1}$ where $u_c = 5.44\ \mu\text{m}^{-1}$. Images are displayed using a different intensity scale mapped to the grayscale to facilitate visualization of details in each image.

Clearly, Eq. (7) is different from Eq. (1) and the forward images predicted from these two models, shown in **Error! Reference source not found.**(b) and (c), respectively, are different. More over as demonstrated in Chapter 3 the model prediction obtained with Eq. (7) captures the trends observed in experimental data acquired from a uniform layer and 6 μm spherical shell (see Fig. 21). It is important to note that model-based restoration methods must be developed based on the most accurate model that predicts the acquired data in order to avoid undesirable restoration artifacts.

5.2. Current methods

Since SIM is based on a computational sensing paradigm, computational methods are an integral part of the imaging system modification and have a direct impact on the improved performance. Additionally, the illumination pattern plays the main role in the type of SIM achieved, which can be either 2D-SIM [15,91] (when the pattern provides only lateral modulation), or 3D-SIM [14,16,42] (when the pattern provides lateral and axial modulation simultaneously). There are two main computational approaches in solving the inverse imaging problem in SIM. The first approach is based on a set of steps involving demodulation using a matrix inversion followed by deconvolution with a non-iterative generalized Wiener filter [14,16,20], which assumes the correct imaging model [Eq. (7)], i.e., a model that takes into account how the data is acquired. The details of this approach for both the 3W-SIM [14] and the tunable-frequency 3D-SIM [16] systems are provided in Appendix C. Because of its simplicity and speed, this direct method is currently the most used in practice, and it is available on commercial SIM systems, such as the ZEISS Elyra and the Nikon S-SIM.

The second restoration approach relies on iterative model-based optimization algorithms that have the potential to significantly improve reconstruction quality and robustness over the direct approach. To the best of our knowledge, Orieux *et al.* [70] were the first to report an iterative approach for SIM microscopy. Several other works have since then resulted in related methods [74,92,101–103,93–100], which minimize the mean squared of the difference between the recorded data and the forward images predicted by the imaging model in every iteration, formulated as the cost function given below:

$$F\left(o(\boldsymbol{x},z)\right)=\sum_{l=1}^{L}\left\|g_l^{mes}(\boldsymbol{x},z)-g_l(\boldsymbol{x},z)\right\|^2. \tag{8}$$

where $\|.\|$ indicates the l^2-norm of the function, and $g_l^{mes}(\boldsymbol{x},z)$ and $g_l(\boldsymbol{x},z)$ are the l^{th} 3D recorded image and model prediction, respectively. These model-based methods have been developed for 2D restoration of high-resolution image from multiple low-resolution 2D images, i.e. for 2D processing of 2D images acquired with either a 2D-SIM or a 3D-SIM system, in which case the model in Eq. (1) is valid because the illumination is only present in a single axial plane. In this dissertation, we develop a model-based iterative method for 3D restoration using the correct 3D model of Eq. (7), which has the potential of providing improved 3D resolution over the current 2D-processing model-based methods.

5.3. Proposed deconvolution method

We have derived a 3D model-based (3D-MB) approach that minimizes the same cost function [Eq. (8)], which was used by other approaches [74,92,101–103,93–100]. The main difference is that we have applied the 3D forward imaging model [Eq. (7)], which takes

into account 3D data-acquisition with axial scanning as described in Section 5.1. It is important to note that model-based deconvolution methods based on the 3D forward imaging model of Eq. (1) are not valid for 3D-processing of data acquired with 3D-SIM systems to remove out-of-focus light. In [46], we have shown that 2D reconstruction provides less accurate results compared to 3D reconstruction, as it is not able to remove out-of-focus light adequately in every single plane. The 3D reconstruction can remove the out-of-focus light and improve the in-focus contrast, which helps in the visualization and quantification of high-resolution information. There are some other approaches that have restored a 3D image by performing a slice-by-slice 2D reconstruction and removing the out-of-focus light by subtraction [41] or considering a few additional planes (above and below each focal plane in order to collect out-of-focus light) during the reconstruction process [95,103]. In the case of our proposed method, 3D processing to remove out-of-focus light from the entire volume relies on a 3D forward imaging model, which is the basis of the reconstruction algorithm.

Similarly to [104], a conjugate-gradient descent algorithm has been used to solve the SIM linear inverse problem [Eq. (8)] to reconstruct $o(\boldsymbol{x}, z)$ using the following recursive relation:

$$\hat{o}_n = \hat{o}_{n-1} + \alpha_n d_n. \tag{9}$$

where $\hat{o}_n$ and $\hat{o}_{n-1}$ represent estimations of the unknown density of fluorophores at iteration steps n and $n-1$, respectively. The correction $\alpha_n d_n$ is composed of a scalar α_n

(the step size) and an updating direction d_n taken equal to the well-known Polak-Ribière conjugate gradient direction [105]:

$$d_n = \nabla_n + \gamma_n d_{n-1}, \qquad \text{with } \gamma_n = \frac{\langle \nabla_n \mid \nabla_n - \nabla_{n-1} \rangle}{\|\nabla_{n-1}\|^2} \tag{10}$$

in which $\langle \cdot \mid \cdot \rangle$ is the inner product. The gradient of the cost function, Eq. (8), with respect to $o(\boldsymbol{x}, z)$ is given by (see Appendix D for derivation):

$$\nabla = -2 \sum_{l=1}^{L} \sum_{k} j_{k;l}(\boldsymbol{x}) \left\{ \left[g_l^{mes}(\boldsymbol{x}, z) - g_l(\boldsymbol{x}, z) \right] \otimes_3 \left[h(\boldsymbol{x}, z) i_k(z) \right]^* \right\}. \tag{11}$$

where * stands for the conjugate operator. The step size α_n is determined at each iteration n by minimizing the cost function [Eq. (8)] with respect to α_n, in which the expression $\hat{o}_n$ is substituted by $\hat{o}_{n-1} + \alpha_n d_n$ [Eq. (9)]. This leads to the following cost function:

$$\begin{aligned} f(\alpha_n) &= F(o_{n-1} + \alpha_n d_n) = \sum_{l=1}^{L} \left\| g_l^{mes}(\boldsymbol{x}, z) - g_l(\boldsymbol{x}, z) \right\|^2 \\ g_l(\boldsymbol{x}, z) &= \sum_{k} \left[\left\{ o_{n-1}(\boldsymbol{x}, z) + \alpha_n d_n \right\} j_{k;l}(\boldsymbol{x}) \right] \otimes_3 \left[h(\boldsymbol{x}, z) i_k(z) \right]. \end{aligned} \tag{12}$$

By minimizing this polynomial (second order) cost function with respect to α_n, α_n is determined analytically as follows (see Appendix D for derivation):

$$\alpha_n = -\frac{d_n \nabla_n}{d_n \left(2 \sum_{l=1}^{L} \sum_{k} j_{k;l}(\boldsymbol{x}) \left[\sum_{k} \left[d_n j_{k;l}(\boldsymbol{x}) \right] \otimes_3 \left[h(\boldsymbol{x}, z) i_k(z) \right]^2 \right] \right)}. \tag{13}$$

It is important to note that, if one does not consider the axial scanning of the sample during the data acquisition and Eq. (1) instead of Eq. (7) is used in the cost function, then the gradient function would be different and expressed by:

$$\nabla = -2\sum_{l=1}^{L} i(\boldsymbol{x},z)\left\{\left[g_l^{mes}(\boldsymbol{x},z) - g_l(\boldsymbol{x},z)\right] \otimes_3 h(\boldsymbol{x},z)^*\right\}. \tag{14}$$

5.3.1. Proposed method with positivity constraint

In many cases introducing the positivity *a priori* information of the parameter of interest, herein the density of fluorophores, improves the performance of the inverse scheme [104]. This is realized by retrieving an auxiliary function $\xi(\boldsymbol{x},z)$ such that $o(\boldsymbol{x},z) = \xi^2(\boldsymbol{x},z)$. The inverse scheme presented above remains unchanged provided that the gradient ∇ [Eq. (11)] is replaced by the gradient ∇_ξ, which is the gradient of the cost functional F with respect to ξ instead of o (see Appendix D for derivation):

$$\nabla_\xi = -4\sum_{l=1}^{L}\sum_{k} j_{k;l}(\boldsymbol{x})\xi(\boldsymbol{x},z)\left\{\left[g_l^{mes}(\boldsymbol{x},z) - g_l(\boldsymbol{x},z)\right] \otimes_3 \left[h(\boldsymbol{x},z) i_k(z)\right]^*\right\}. \tag{15}$$

In addition, the scalar step α_n is determined analytically at each iteration n by minimizing the cost function as follows:

$$\begin{aligned} f(\alpha_n) &= F\left(\left[\xi_{n-1} + \alpha_n d_n\right]^2\right) = \sum_{l=1}^{L}\left\|g_l^{mes}(\boldsymbol{x},z) - g_l(\boldsymbol{x},z)\right\|^2 \\ g_l(\boldsymbol{x},z) &= \sum_k \left[\left[\xi_{n-1}(\boldsymbol{x},z) + \alpha_n d_n\right]^2 j_{k;l}(\boldsymbol{x})\right] \otimes_3 \left[h(\boldsymbol{x},z) i_k(z)\right]. \end{aligned} \tag{16}$$

The gradient of the cost function in Eq. (16) with respect to α (∇_α, see Appendix D for the derivation) is set to zero as follows:

$$\begin{aligned}
&\alpha_n^3 d_n^2 B + \alpha_n^2 \left(d_n^2 C + \xi d_n B \right) + \alpha_n \left(-d_n^2 A + \xi d_n C \right) + d_n \nabla_\xi = 0, \\
&A = 4 \sum_{l=1}^{L} \sum_{k} j_{k;l}(\boldsymbol{x}) \left[g_l^{mes}(\boldsymbol{x}, z) \otimes_3 \left[h(\boldsymbol{x}, z) i_k(z) \right]^* - \sum_{k'} \left[\xi^2 j_{k';l}(\boldsymbol{x}) \right] \otimes_3 \left[h(\boldsymbol{x}, z) i_{k'}(z) \right]^2 \right], \\
&B = 4 \sum_{l=1}^{L} \sum_{k} j_{k;l}(\boldsymbol{x}) \left[\sum_{k'} \left[d_n^2 j_{k';l}(\boldsymbol{x}) \right] \otimes_3 \left[h(\boldsymbol{x}, z) i_{k'}(z) \right]^2 \right], \\
&C = 4 \sum_{l=1}^{L} \sum_{k} j_{k;l}(\boldsymbol{x}) \left[\sum_{k'} \left[\xi d_n j_{k';l}(\boldsymbol{x}) \right] \otimes_3 \left[h(\boldsymbol{x}, z) i_{k'}(z) \right]^2 \right].
\end{aligned} \tag{17}$$

We minimized this forth order polynomial function with respect to α_n by determining analytically an admissible solution for α_n from the four roots of Eq. (17) using the *roots* built-in Matlab function.

5.4. Results

To assess the performance of the proposed iterative 3D-MB method and to compare it to the traditional non-iterative GWF approach used in SIM, simulations were performed. The method was applied to data from two different systems: 3W-SIM and tunable 3D-SIM. In this section, results obtained from noiseless and noisy simulated SIM data are presented and quantified using different criteria.

5.4.1. Criteria

The discrepancy between the estimated $\hat{o}$ and the true object o is assessed using the mean squared error (MSE) [106] and the structured similarity (SSIM) [106] computed as follows:

$$MSE(o,\hat{o}) = \frac{1}{XYZ}\sum_{x=1}^{X}\sum_{y=1}^{Y}\sum_{z=1}^{Z}\left[o(\boldsymbol{x},z) - \hat{o}(\boldsymbol{x},z)\right]^2, \tag{18}$$

$$SSIM(o,\hat{o}) = \frac{\left(2\mu_o\mu_{\hat{o}}\right)\left(2\,\mathrm{cov}_{o\hat{o}}\right)}{\left(\mu_o^2+\mu_{\hat{o}}^2\right)\left(\sigma_o^2+\sigma_{\hat{o}}^2\right)}. \tag{19}$$

where X, Y, and Z are the grid size, μ and σ indicate the mean and standard deviation, respectively, and $\mathrm{cov}_{o\hat{o}}$ is the covariance between o and $\hat{o}$.

5.4.2. Noiseless results

To investigate the restoration performance of the proposed iterative 3D-MB algorithm for 3D-SIM [Eqs (9)-(13)], a synthetic 3D test object was simulated, on a 256×256×256 grid as shown in Fig. 34(a). This object is a compound object composed by an outer spherical shell and inner spherical beads to mimic a cell's structure in biological studies, which is a suitable object for investigating OS and SR capabilities. While the diameter and the thickness of the spherical shell are 3 μm and 200 nm, respectively, the diameter of each bead is 125 nm and the closest distance between two neighboring beads is equal to 100 nm. This is below the lateral resolution limit of the conventional WF microscope, which is equal to $d_{xy} = \frac{0.61\lambda}{\mathrm{NA}} = 224$ nm [Eq. (1) in Chapter 1] for the emission wavelength at λ=515

nm and imaging lens' numerical aperture, NA=1.4. It is worth to mention that this is a challenging object because the SIM lateral resolution limit achieved by using the SI pattern is $d_{SIM} = \frac{d}{1+(u_m / u_c)}$, which is equal to 112 nm for the SI pattern when using the highest lateral modulation frequency and it is still below the closest distance between two neighboring beads.

We simulated the SI pattern in 3W-SIM and tunable 3D-SIM systems, using Eq. (14) and Eq. (16) in Section 1.3.2, respectively. Parameters for 3W-SIM are $u_m = 0.8u_c$, $w_m = 0.25u_m$, and 5 illumination phases, φ, shifted by a $\frac{2\pi}{5}$ step. Parameters for tunable 3D-SIM are $u_m = 0.8u_c$, $w_m = 0.04u_m$ [$x_0 = 320\ \mu$m and $N = 3$ (this is the same design that we have compared with 3W-SIM in Fig. 32 in Chapter 4 based on the synthetic OTF)], and 3 illumination phases, φ, shifted by a $\frac{2\pi}{3}$ step. Three orientation angles, $\theta = 0^\circ,\ 60^\circ,\ 120^\circ$, of the SI pattern are used for both system to provide isotropic resolution improvement. Then, 15 and 9 3D forward images (5 and 3 3D forward images per orientation) were generated based on Eq. (7) for 3W-SIM and tunable-frequency 3D-SIM systems, respectively.

The result from the proposed method (3D-MB) is compared to the result obtained from the generalized Wiener filter (GWF) [14] (see Appendix C for details about the GWF approach). The regularization parameter in the GWF method was empirically determined in each case.

Fig. 34(b) and (c) show the noiseless results from the GWF and 3D-MB methods applied to data from the 3W-SIM system; the *xy*-section images indicate that the 3D-MB provides better discrimination between two neighboring beads (high frequency information of the true object). This is because GWF is not robust as 3D-MB and therefore its performance deteriorates where high-frequency information needs to be retrieved. It is worth mentioning that the achieved SIM lateral resolution limit $d_{SIM} = 112$ nm for the SI pattern implemented here, which is still below the closest distance between two neighboring beads in the object. Therefore, the difference between the true object and the 3D-MB result is expected. However, the *xz*-section images show that GWF has better optical sectioning capability when considering the axial extent of the inner beads. This is because of the single-shot demodulation step in the GWF method rather than the iterative demodulation step in the model-based approach. To demonstrate the impact of using the correct 3D-SIM model on the restoration, i.e., by accounting for the axial scanning of the sample, we also processed the simulated image using the gradient function in Eq. (14) instead of Eq. (11) in the 3D-MB method, thereby simulating a model mismatch. The result from the model-mismatched 3D-MB [using the gradient in Eq. (11)] is shown in Fig. 34(d), suffers from many artifacts due to the model mismatch.

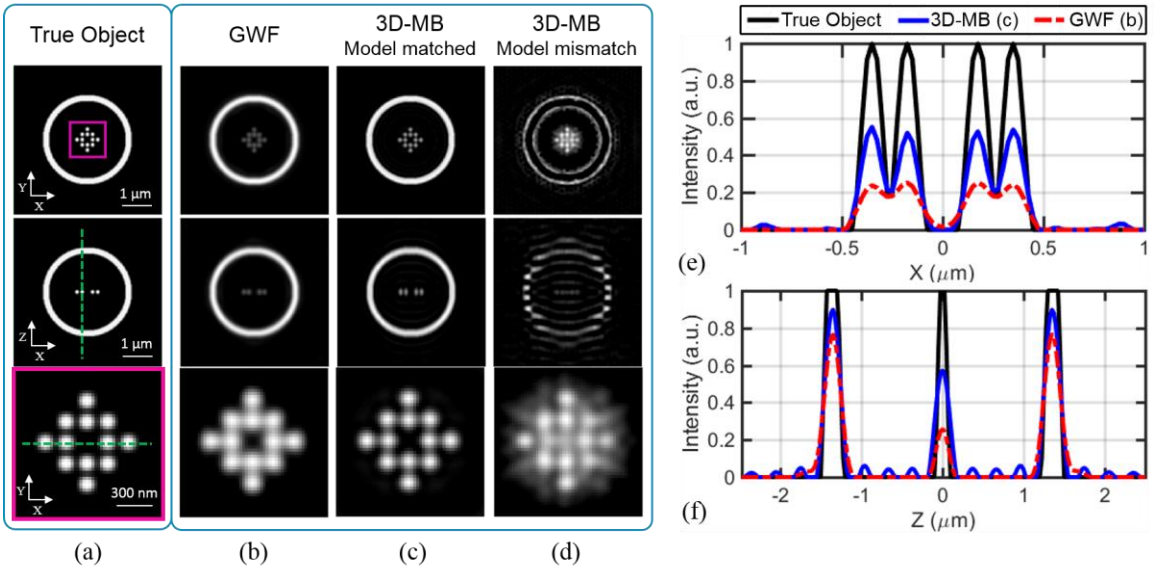

Fig. 34. Qualitative and quantitative evaluation of the proposed model-based approach (3D-MB) for 3W-SIM using simulated noiseless data. Lateral view (top row), axial view (middle row) and zoomed view of the cropped square marked with a pink line in the top left image (bottom row) of the 3D: (a) true object; reconstructed image using (b) GWF, (c) proposed 3D-MB when the model matches, (d) proposed 3D-MB when the model does not match the data. Lateral (e) and axial (f) intensity profiles taken along the green dashed lines shown in the bottom and middle rows of (a-c), respectively. For the 3D-SIM system, the lateral modulation frequency was set at $u_m = 0.8u_c = 4.35\ \mu\text{m}^{-1}$ where $u_c = 5.44\ \mu\text{m}^{-1}$. The 3D-MB method results are shown after 400 iterations with the initial guess set equal to WF image provided by averaging 15 forward SIM images. The regularization parameter in the GWF method was empirically determined and it is equal to 10e-6. Negative values in the restored images were set to zero. Images are displayed using a different intensity scale mapped to the grayscale to facilitate visualization of details in each image.

The proposed 3D-MB method is applied to two different 3D-SIM systems, 3W-SIM and tunable 3D-SIM, and compared with GWF approach as shown in Fig. 35. The result of the proposed 3D-MB approach applied to the tunable 3D-SIM [Fig. 35(e)] is also verified that the proposed 3D-MB approach is able to discriminate better between two neighboring beads than the GWF [see bottom row of Fig. 35(d) and (e) and the intensity profile in Fig. 35(g)]. However, the GWF has better optical sectioning capability considering the axial extent of the inner beads [see middle row of Fig. 35(d) and (e) and

the intensity profile in Fig. 35(h)]. This is again because of the single-shot demodulation step in the GWF method rather than the iterative demodulation step in the model-based approach, which was verified and discussed in Fig. 34 as well. It is expected to improve the optical sectioning capability in 3D-MB approach by increasing the number of iterations.

By comparing the results of the proposed 3D-MB approach applied to 3W-SIM [Fig. 35(c)] and tunable 3D-SIM [Fig. 35(e)], one can conclude that tunable 3D-SIM is able to discriminate better between two neighboring beads than the 3W-SIM [see bottom row of Fig. 35(c) and (e) and the intensity profile in Fig. 35(g)]. This is interesting as the two systems provide the same OTF compact support laterally [Fig. 31(a) and (b)], however they have different corresponding components (WF OTF replicas). In 3W-SIM, there are 5 components, D_k, $k=0,\pm1,\pm2$ (see Appendix C for more details): the D_0 component is related to the WF system, the $D_{\pm1}$ components are related to the OS capability, and the $D_{\pm2}$ components are related to the SR capability. In tunable 3D-SIM, there are 3 components, D_k, $k=0,\pm1$: the D_0 component is related to the WF system, and the $D_{\pm1}$ components are related to the SR capability, which their synthetic OTF, $H_{\pm1}(\boldsymbol{u},w)$, have been modified optically to remove the out-of-focus light from the $D_{\pm1}$ components and provide the OS capability simultaneously. The final restored image is the combination of these components. Therefore, the SR capability achieved by the $D_{\pm2}$ components in 3W-SIM is affected by the resolution limits of the $D_{\pm1}$ components, which is the half of the resolution limits of the $D_{\pm2}$ components. However, the SR capability achieved by the $D_{\pm1}$ components in the tunable 3D-SIM is only affected by the D_0 component, which is also the case for the 3W-SIM.

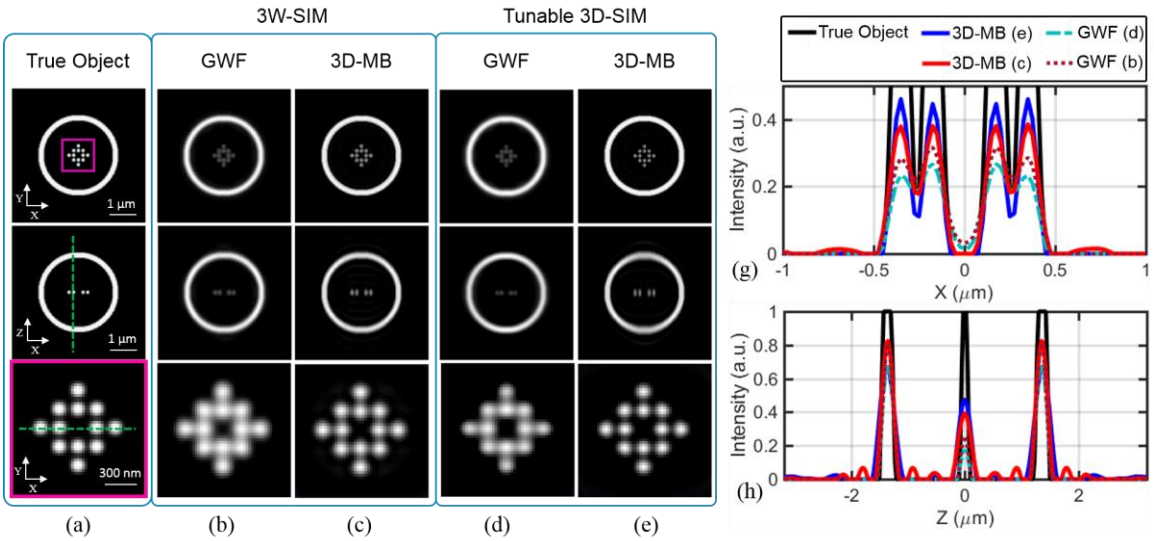

Fig. 35. Qualitative and quantitative evaluation of the proposed model-based approach (3D-MB) for 3W-SIM and Tunable 3D-SIM using simulated noiseless data. Lateral view (top row), axial view (middle row) and zoomed view of the cropped square marked with a pink line in the top left image (bottom row) of the 3D: (a) true object; reconstructed image for 3W-SIM system using (b) GWF, (c) 3D-MB; reconstructed image for Tunable 3D-SIM system using (d) GWF, (e) 3D-MB. Lateral (f) and axial (g) intensity profiles taken along the green dashed lines shown in the bottom and middle rows of (a-e), respectively. For the 3D-SIM system, the lateral modulation frequency was set at $u_m = 0.8u_c = 4.35\ \mu\text{m}^{-1}$ where $u_c = 5.44\ \mu\text{m}^{-1}$. The 3D-MB method results are shown after 400 iterations with the initial guess set equal to WF image provided by averaging the 9 forward images for tunable 3D-SIM and 15 forward images for 3W-SIM. The regularization parameter in the GWF method was empirically determined and it is equal to 10e-6 for (b) and (d), respectively. Negative values in the restored images were set to zero. Images are displayed using a different intensity scale mapped to the grayscale to facilitate visualization of details in each image.

Regarding the OS capability, it is shown in Chapter 4 that the 3W-SIM provides better OS capability than the tunable 3D-SIM at a high modulation frequency, $u_m = 0.8u_c$ and it is verified here through the restoration process [see middle row of Fig. 35(c) and (e) and the intensity profile in Fig. 35(h)].

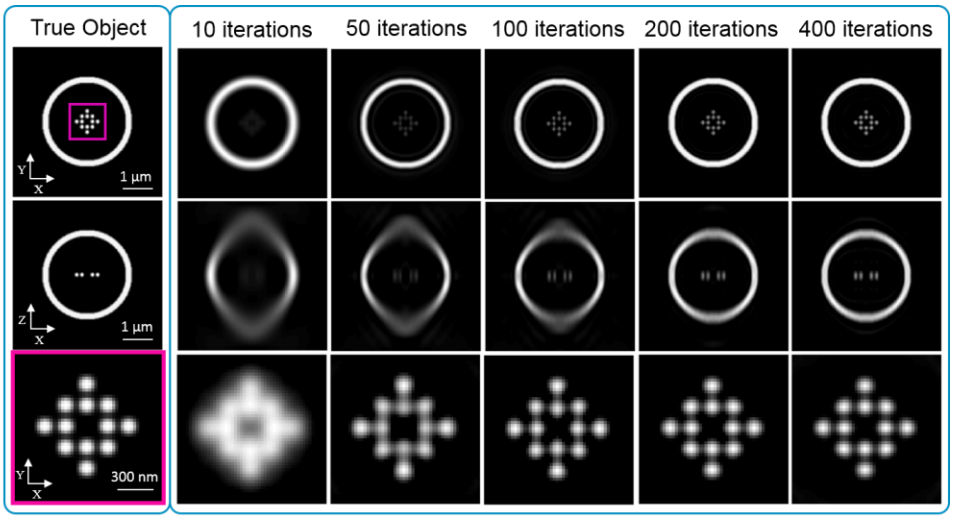

(g)

Number of Iteration	MSE	SSIM
10	6.1e-3	0.69
50	3.7e-3	0.83
100	2.4e-3	0.89
200	9.5e-4	0.96
400	6.8e-4	0.97

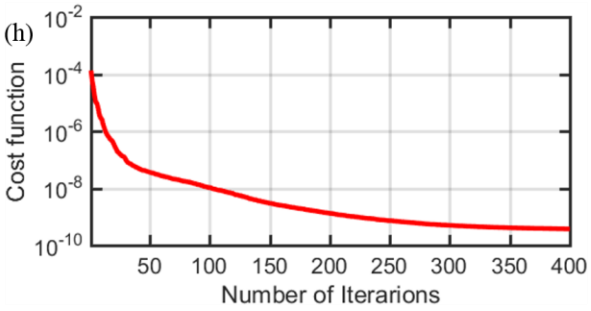

Fig. 36. The effect of the number of iteration on the performance of the proposed model-based approach (3D-MB) for tunable 3D-SIM using simulated noiseless data. Lateral view (top row), axial view (middle row) and zoomed view of the cropped square marked with a pink line in the top left image (bottom row) of the 3D: (a) true object; reconstructed image for tunable 3D-SIM system using (b) 10 iterations, (c) 50 iterations, (d) 100 iterations, (e) 200 iterations, (f) 400 iterations. Quantitative comparison using MSE and SSIM (g). Monotonically decreasing cost function [Eq. (8)] (h). For the 3D-SIM system, the lateral modulation frequency was set at $u_m = 0.8u_c = 4.35\ \mu\text{m}^{-1}$ where $u_c = 5.44\ \mu\text{m}^{-1}$. The initial guess set equal to WF image provided by averaging 9 forward SIM images. Negative values in the restored images were set to zero. Images are displayed using a different intensity scale mapped to the grayscale to facilitate visualization of details in each image.

In any iterative restoration approach, the higher the number of iterations used generally leads to a better result in a noiseless scenario as it is investigated in Fig. 36. The result of the proposed method applied to data from the tunable 3D-SIM, is shown for different number of iterations. The value of the MSE and SSIM are reported in a table shown in Fig.

36(g) to quantify the results. Moreover, the value of the cost function [Eq. (8)] for every iteration is also shown in Fig. 36(h).

5.4.3. Noisy results

In addition to the noiseless simulations, noisy simulations were performed to evaluate the proposed method. Poisson noise has been incorporated in the forward images [88] resulting in a noisy image with four SNR levels of 20, 15, 10, 5 dB. According to Poisson statistics, the SNR value corresponds to the mean of the squared root of the intensity at each pixel in the 3D image.

A quantitative comparison of the performance of the two approaches using the MSE the SSIM are summarized in Table 1, which verifies that the 3D-MB method is more robust to noise for both 3D-SIM systems compared to the GWF method. Moreover, the results from the GWF method are consistent with the results from the evaluation of synthetic OTF shown in Fig. 32 of Chapter 4 for $u_m = 0.8u_c$. We have concluded through the restoration results that both systems perform equally well for a high SNR (>20 dB) but their performances are different for low SNR. The 3W-SIM system performs slightly better axially for low SNR than the tunable 3D-SIM system, however the tunable 3D-SIM system outperforms laterally. This trend is also visible in Fig. 37(d) and (e). By applying the proposed 3D-MB method to both systems under noisy conditions as shown in Fig. 37(b) and (c), the 3W-SIM system has better performance axially than the tunable 3D-SIM system consistent with the results from the evaluation of synthetic OTF shown in Fig. 32 of Chapter 4 for $u_m = 0.8u_c$. Furthermore, the lateral performance of the tunable 3D-SIM

system outperforms for SNR = 20 dB and SNR = 15 dB. However, it underperforms for SNR = 10 dB and SNR = 5 dB compare with the lateral results of 3W-SIM systems.

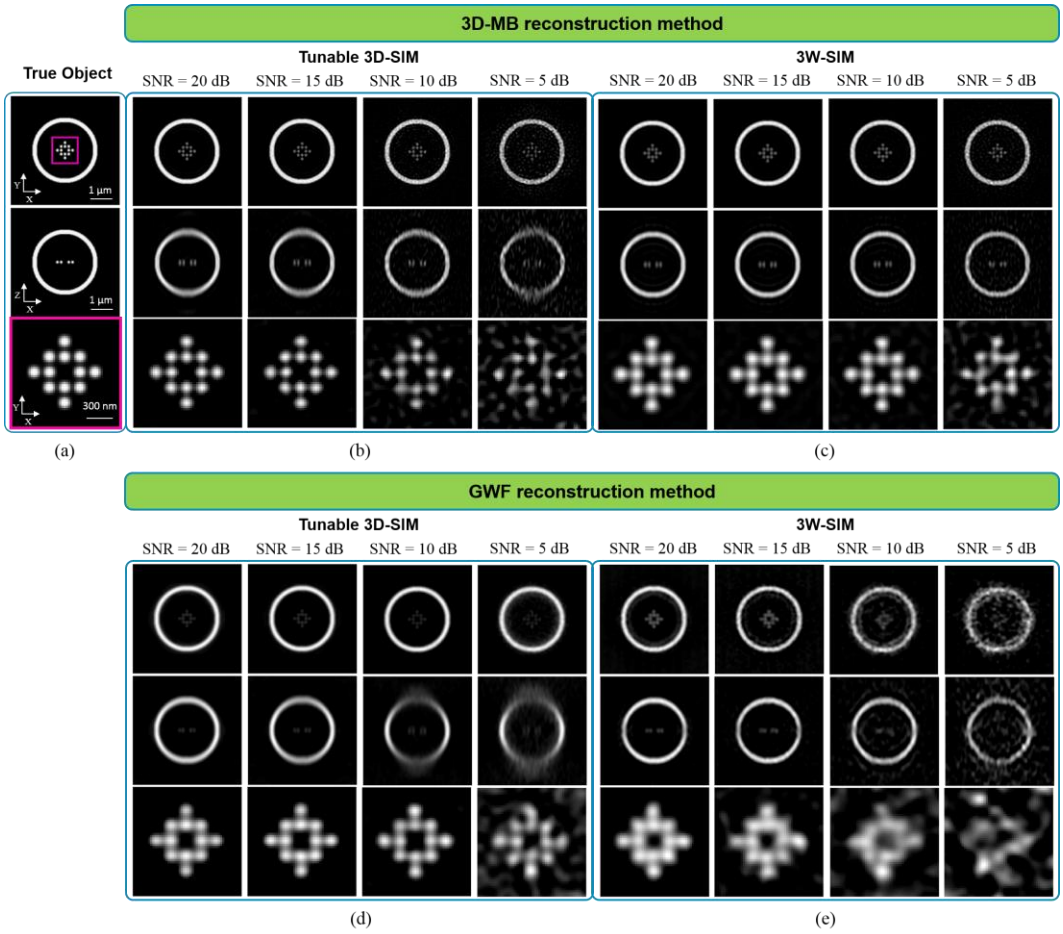

Fig. 37. Qualitative evaluation of the proposed model-based approach (3D-MB) applied to 3W-SIM and Tunable 3D-SIM using simulated noisy data. Lateral view (top row), axial view (middle row) and zoomed view of the cropped square marked with a pink line in the top left image (bottom row) of the 3D: (a) true object; (b) reconstructed image for tunable 3DSIM system for different SNR values with 3D-MB method; (c) reconstructed image for 3W-SIM system for different SNR values with 3D-MB method; (d) reconstructed image for tunable 3D-SIM system for different SNR values with GWF method; (e) reconstructed image for 3W-SIM system for different SNR values with GWF method. For both 3D-SIM system, the lateral modulation frequency was set at $u_m = 0.8u_c = 4.35\ \mu m^{-1}$. The 3D-MB method results are shown after 200 iterations with the initial guess set equal to WF image provided by averaging the 9 forward images for tunable 3D-SIM and 15 forward images for 3W-SIM. The regularization parameter in the GWF method was empirically determined and it is equal to 5e-3, 1e-2, 5e-2, and 9e-2, for 20dB, 15 dB, 10 dB, and 5 dB, respectively, for both (d) and (e). Images are displayed using a different intensity scale mapped to the grayscale to facilitate visualization of details in each image.

Table 1. Performance comparison of two SIM restoration methods and two 3D-SIM systems. MSE and SSIM computed between the restored and true object intensities.

	SNR	**20 dB**	**15 dB**	**10 dB**	**5 dB**
3W-SIM	GWF: MSE	1.2e-3	1.5e-3	2.4e-3	5.5e-3
	3D-MB: MSE	9.2e-4	9.3e-4	1.1e-3	2.5e-3
	GWF: SSIM	0.95	0.94	0.87	0.67
	3D-MB: SSIM	0.97	0.96	0.95	0.86
Tunable 3D-SIM	GWF: MSE	1.2e-3	1.3e-3	3.2e-3	4.7e-3
	3D-MB : MSE	1.0e-3	1.3e-3	2.4e-3	5.2e-3
	GWF: SSIM	0.94	0.94	0.84	0.69
	3D-MB: SSIM	0.96	0.94	0.88	0.72

To investigate the noisy results in more details and verify with the results obtained from the noise investigation of the synthetic OTF provided in Chapter 4, the restored images of two 3D-SIM systems (the 3W-SIM [14] and tunable 3D-SIM systems [16]) are evaluated at two different modulation frequencies ($u_m = 0.5u_c$ and $u_m = 0.8u_c$) and two different SNR levels (SNR = 5 and 10 dB). Fig. 38 shows the restored images by the proposed 3D-MB method at $u_m = 0.8u_c$ for SNR = 10 dB and the corresponding evaluation of the synthetic OTF. The result of 3W-SIM system is better than tunable 3D-SIM system based on MSE and SSIM metrics reported in a table in Fig. 38. For more evaluation, we have compared the lateral and axial views of the restored images. The *xz*-section of the restored images [middle row of Fig. 38(b-c)] indicate qualitatively that the 3W-SIM system provides slightly better OS capability compared to the tunable 3D-SIM system. This conclusion has been verified quantitatively (for SNR = 10 dB, there is a 12% and 20% reduction in the effective axial cutoff frequency in the 3W-SIM and tunable 3D-SIM, respectively) by evaluating the synthetic OTF in Fig. 38(e). However, the zoomed views of the *xy*-section from the restored images [bottom row of Fig. 38(b-c)] indicate that the

tunable 3D-SIM system provides slightly better lateral SR capability compared to the 3W-SIM system as the small beads are more resolvable. This conclusion has been verified quantitatively (for SNR = 10 dB, there is a 13% and 17% reduction in the effective lateral cutoff frequency in the tunable 3D-SIM and 3W-SIM, respectively) by evaluating the synthetic OTF in Fig. 38(d). There is some artifact due to the noise, which can be improved by adding a regularization term to the cost function in Eq. (8) to address the impact of noise effect on the restored images obtained by the proposed 3D-MB approach, which is suggested as a future work.

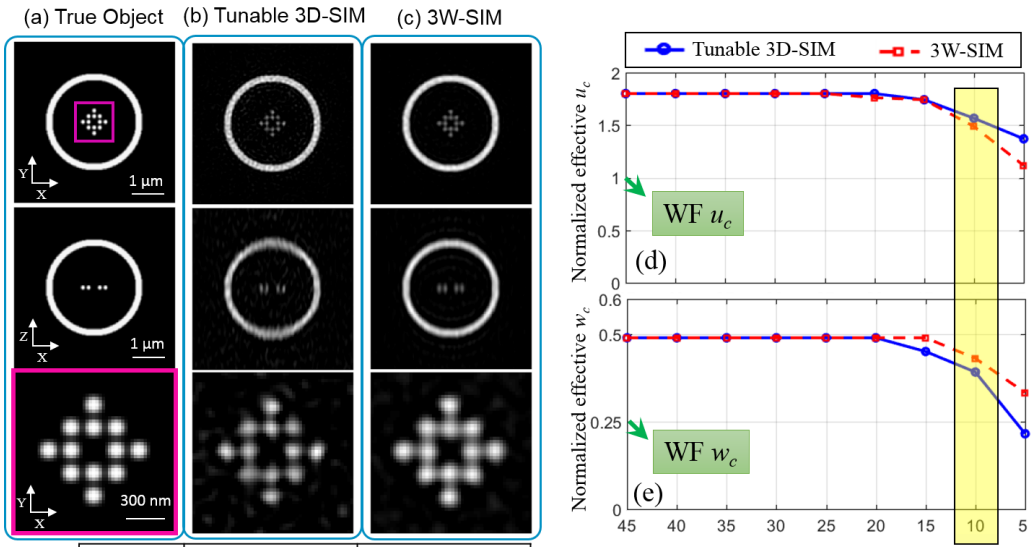

MSE	2.4e-3	1.1e-3
SSIM	0.88	0.95

Fig. 38. Qualitative and quantitative evaluation of the proposed model-based approach (3D-MB) applied to 3W-SIM and tunable 3D-SIM using simulated noisy data (SNR = 10 dB). Lateral view (top row), axial view (middle row) and zoomed view of the cropped square marked with a pink line in the top left image (bottom row) of the 3D: (a) true object; (b) reconstructed image for tunable 3D-SIM system; (c) reconstructed image for 3W-SIM system. Effective (d) lateral and (e) axial cutoff frequencies for different SNR levels. The lateral modulation frequency was set at $u_m = 0.8u_c = 4.35\ \mu\text{m}^{-1}$. The 3D-MB method results are shown after 200 iterations with the initial guess set equal to WF image provided by averaging the 9 and 15 forward images for tunable 3D-SIM and 3W-SIM systems, respectively. Images are displayed using a different intensity scale mapped to the grayscale to facilitate visualization of details in each image.

Because when imaging optically-thick samples, there is a need to reduce the lateral modulation frequency to modulate the sample's information [83,84], results from the two systems obtained at $u_m = 0.5u_c$ for SNR = 5 dB are also evaluated as shown in Fig. 39. The result from the 3W-SIM system is better than the one from the tunable 3D-SIM system based on the MSE and SSIM metrics reported in the table in Fig. 39. However, the performance of the two systems based on the axial and lateral views of the restored images at $u_m = 0.5u_c$ is different from their performance at $u_m = 0.8u_c$. The *xz*-section of the restored images [middle row of Fig. 39(b-c)] indicate qualitatively that the tunable 3D-SIM system provides better OS capability compared to the 3W-SIM system. This conclusion has been verified quantitatively (the tunable 3D-SIM system outperforms 3W-SIM at all SNR levels with axial resolution improvement by a factor of 2.2× compared to the 1.6× improved achieved by the 3W-SIM system) by evaluating the synthetic OTF in Fig. 39(e). The zoomed views of *xy*-sections from the restored images [bottom row of Fig. 39(b-c)] indicate that the 3W-SIM system provides slightly better lateral SR capability compared to the tunable 3D-SIM system. This conclusion has been verified quantitatively (for SNR = 5 dB, there is a 36% and 45% reduction in the effective lateral cutoff frequency of the 3W-SIM and tunable 3D-SIM systems, respectively) by evaluating the synthetic OTF in Fig. 39(d).

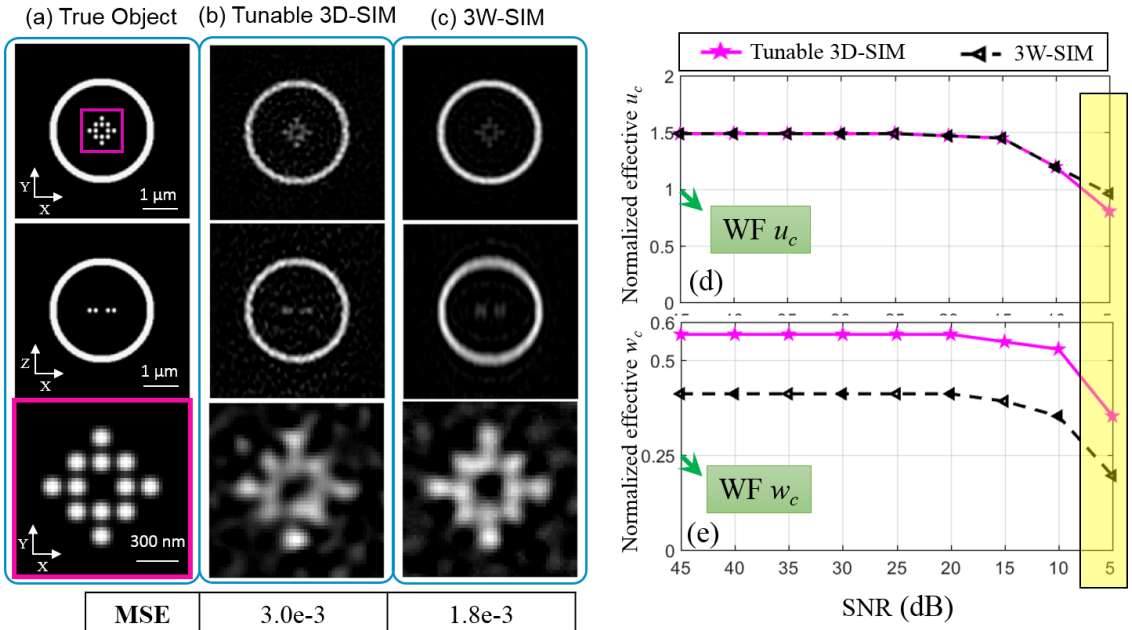

MSE	3.0e-3	1.8e-3
SSIM	0.84	0.92

Fig. 39. Qualitative and quantitative evaluation of the proposed model-based (3D-MB) approach applied to 3W-SIM and tunable 3D-SIM using simulated noisy data (SNR = 5 dB). Lateral view (top row), axial view (middle row) and zoomed view of the cropped square marked with a pink line in the top left image (bottom row) of the 3D: (a) true object; (b) reconstructed image for tunable 3D-SIM system; (c) reconstructed image for 3W-SIM system. Effective (d) lateral and (e) axial cutoff frequencies of the two systems for different SNR levels. For both 3D-SIM systems, the lateral modulation frequency was set at $u_m = 0.5u_c = 2.72\ \mu\text{m}^{-1}$. The 3D-MB method results are shown after 100 iterations with the initial guess set equal to the WF image computed by averaging the 9 forward images in the case of the tunable 3D-SIM system and the15 forward images in the case of the 3W-SIM system. Images are displayed using a different intensity scale mapped to the grayscale to facilitate visualization of details in each image.

5.4.1. Data redundancy

Taking into account the redundancy of the information in the raw SIM images [70], we have reconstructed the 3D image of a sample from simulated 3W-SIM system images by using only 7 (3 images from one pattern orientation and 2 from each of the other two orientations) out of the 15 raw SIM images recorded for each axial plane as they are required by the traditional GWF restoration (Fig. 37).

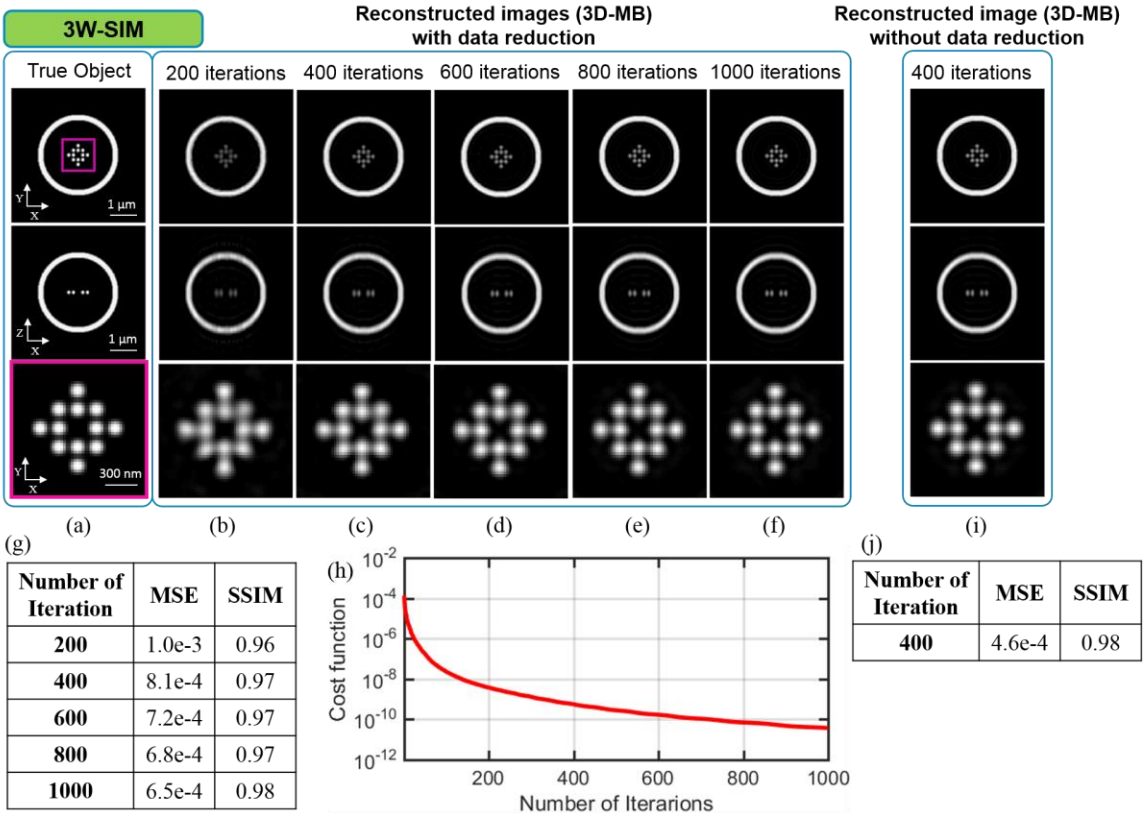

Number of Iteration	MSE	SSIM
200	1.0e-3	0.96
400	8.1e-4	0.97
600	7.2e-4	0.97
800	6.8e-4	0.97
1000	6.5e-4	0.98

Number of Iteration	MSE	SSIM
400	4.6e-4	0.98

Fig. 40. Effect of data reduction (7 out of 15 raw 3W-SIM images used) and number of iterations used on the restoration obtained with the proposed model-based approach (3D-MB) for 3W-SIM using simulated noiseless data. Lateral view (top row), axial view (middle row) and zoomed view of the cropped square marked with a pink line in the top left image (bottom row) of the 3D: (a) true object; reconstructed image using 7 out of 15 raw 3W-SIM images with (b) 200 iterations, (c) 400 iterations, (d) 600 iterations, (e) 800 iterations, (f) 1000 iterations. Quantitative comparison using MSE and SSIM (g). Monotonically decreasing cost function [Eq. (8)] (h). The initial guess set equal to WF image provided by averaging 7 forward SIM images. Reconstructed image using 15 raw 3W-SIM images with 400 iterations (i) and corresponding MSE and SSIM (j). The initial guess set equal to WF image provided by averaging 15 forward SIM images. For the 3D-SIM system, the lateral modulation frequency was set at $u_m = 0.8u_c = 4.35\ \mu\text{m}^{-1}$ where $u_c = 5.44\ \mu\text{m}^{-1}$. Negative values in the restored images were set to zero. Images are displayed using a different intensity scale mapped to the grayscale to facilitate visualization of details in each image.

The results obtained at a different number of iterations are shown in Fig. 40. The result obtained with the data reduction after 1000 iterations [Fig. 40(f)] is very similar to the result obtained without data reduction after 400 iterations [Fig. 40(i)] qualitatively and

quantitatively based on MSE and SSIM metrics reported in Fig. 40(g). It is expected that by increasing the number of iteration (greater than 1000), that we could have even better agreement between these results, suggesting that data reduction is possible in the absence of noise.

Motivated by this results (Fig. 40), we have reduced further the number of forward images used in 3W-SIM restoration of images from the 7 forward images used in Fig. 40 to 5 forward images (3 images from one orientation and 1 from each of the other two orientations) and 4 forward images (2 images from 1 orientation and 1 from each of the other two orientations). The results shown in Fig. 41 indicate that the restored image based on 5 forward images [Fig. 41(d)] provides the same quality as the one obtained based on 7 forward images used. However, with 4 forward images [Fig. 41(e)] some artifact is visible in the axial view (*xz*-section) of the restored images [middle row of Fig. 41(e)], which indicates that the 4 forward images are probably not enough for 3D reconstruction in 3W-SIM. This preliminary investigation indicates that 3D model-based reconstruction for 3W-SIM system can be achieved with a reduced number of forward images (i.e. less than 7 forward images) and more investigation is needed to consider the noise effects as well, which is suggested as a future work.

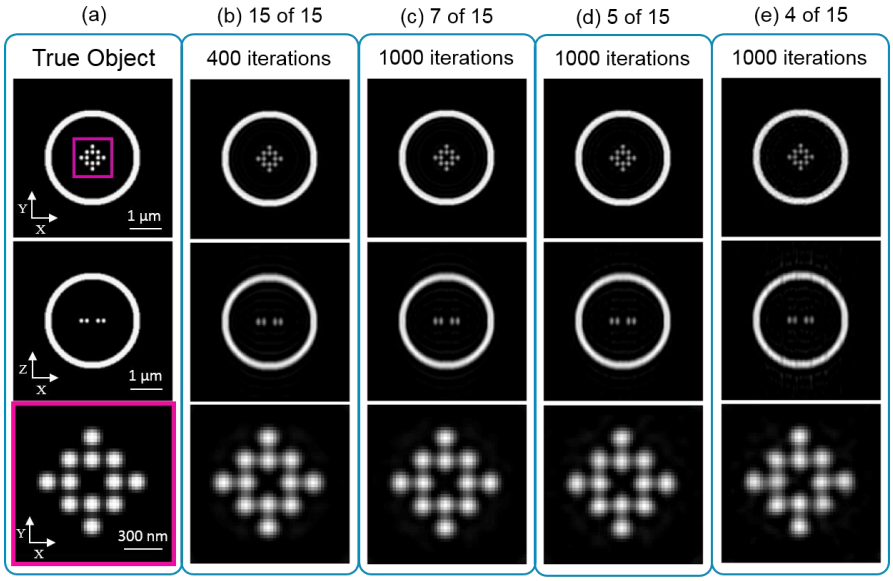

MSE	4.6e-4	6.5e-4	6.8e-4	9.0e-4
SSIM	0.98	0.98	0.97	0.97

Fig. 41. Effect of data reduction on the restoration obtained with the proposed model-based approach (3D-MB) for 3W-SIM using simulated noiseless data. Lateral view (top row), axial view (middle row) and zoomed view of the cropped square marked with a pink line in the top left image (bottom row) of the 3D: (a) true object; reconstructed image using (b) 15 out of 15 raw 3W-SIM images with 400 iterations, (c) 7 out of 15 raw 3W-SIM images with 1000 iterations, (d) 5 out of 15 raw 3W-SIM images with 1000 iterations, (e) 4 out of 15 raw 3W-SIM images with 1000 iterations and corresponding quantitative comparison using MSE and SSIM. The initial guess set equal to WF image provided by averaging the number of forward SIM images used. For the 3D-SIM system, the lateral modulation frequency was set at $u_m = 0.8u_c = 4.35\ \mu\text{m}^{-1}$ where $u_c = 5.44\ \mu\text{m}^{-1}$. Negative values in the restored images were set to zero. Images are displayed using a different intensity scale mapped to the grayscale to facilitate visualization of details in each image.

To investigate the noise effect in 3D reconstruction by 3D-MB method using less number of forward images, we investigate the results of 3W-SIM system for SNR = 15 dB. We have reconstructed the 3D image of the same sample used for noiseless case (Fig. 40) from simulated 3W-SIM system images by using only 7 (3 images from one pattern orientation and 2 from each of the other two orientations) out of the 15 raw SIM images recorded for each axial plane. The results obtained at a different number of iterations are

shown in Fig. 42. The SSIM of the results obtained with 500 and 600 iterations are slightly worse than the one with 400 iterations, which indicates that 400 iterations is enough for this case. For noisy data, less number of iteration is expected [400 iterations, see Fig. 42(e)] compared to the noiseless data [1000 iterations, see Fig. 40(f)]. The result obtained with 400 iterations [Fig. 42(e)] is similar to the result obtained without data reduction after 200 iterations [Fig. 42(h)] qualitatively and quantitatively based on MSE and SSIM metrics reported in Fig. 42. These results indicate that 7 out 15 images can be used for 3D reconstruction for 3W-SIM system in noisy condition as well.

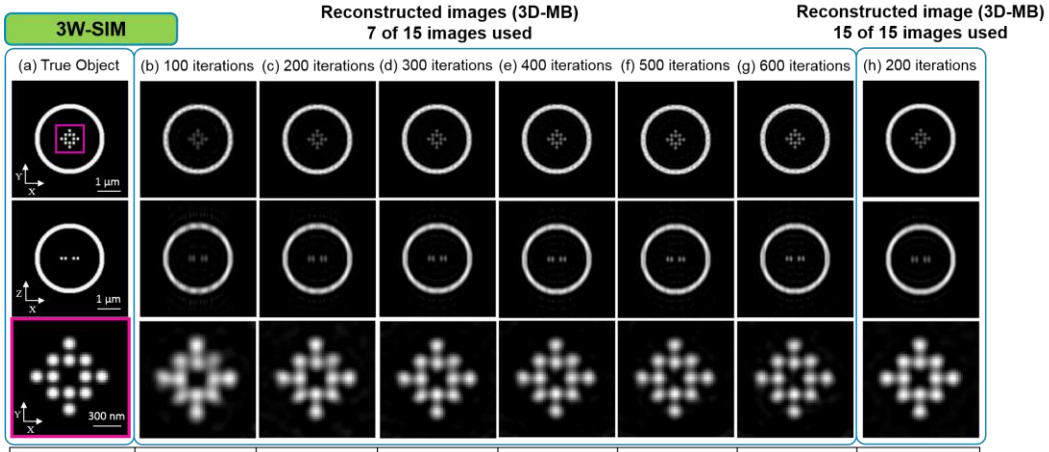

MSE	1.6e-3	1.3e-3	1.2e-3	1.2e-3	1.2e-3	1.2e-3	9.3e-4
SSIM	0.9344	0.9506	0.9536	0.9545	0.9542	0.9537	0.96

Fig. 42. Effect of data reduction (7 out of 15 raw 3W-SIM images used) and number of iterations used on the restoration obtained with the proposed model-based approach (3D-MB) for 3W-SIM using simulated noisy data (SNR = 15dB). Lateral view (top row), axial view (middle row) and zoomed view of the cropped square marked with a pink line in the top left image (bottom row) of the 3D: (a) true object; reconstructed image using 7 out of 15 raw 3W-SIM images with (b) 100 iterations, (c) 200 iterations, (d) 300 iterations, (e) 400 iterations, (f) 500 iterations, (g) 600 iterations and corresponding quantitative comparison using MSE and SSIM. The initial guess set equal to WF image provided by averaging 7 forward SIM images. Reconstructed image using 15 raw 3W-SIM images with 200 iterations (h) and corresponding MSE and SSIM. The initial guess set equal to WF image provided by averaging 15 forward SIM images. For the 3D-SIM system, the lateral modulation frequency was set at $u_m = 0.8u_c = 4.35\ \mu\text{m}^{-1}$ where $u_c = 5.44\ \mu\text{m}^{-1}$. Negative values in the restored images were set to zero. Images are displayed using a different intensity scale mapped to the grayscale to facilitate visualization of details in each image.

We have also reconstructed the 3D image of the same sample from simulated 3W-SIM system images by using only 5 (3 images from one pattern orientation and 1 from each of the other two orientations) out of the 15 raw SIM images recorded for each axial plane for SNR = 15 dB. The results obtained at a different number of iterations are shown in Fig. 42Fig. 43.

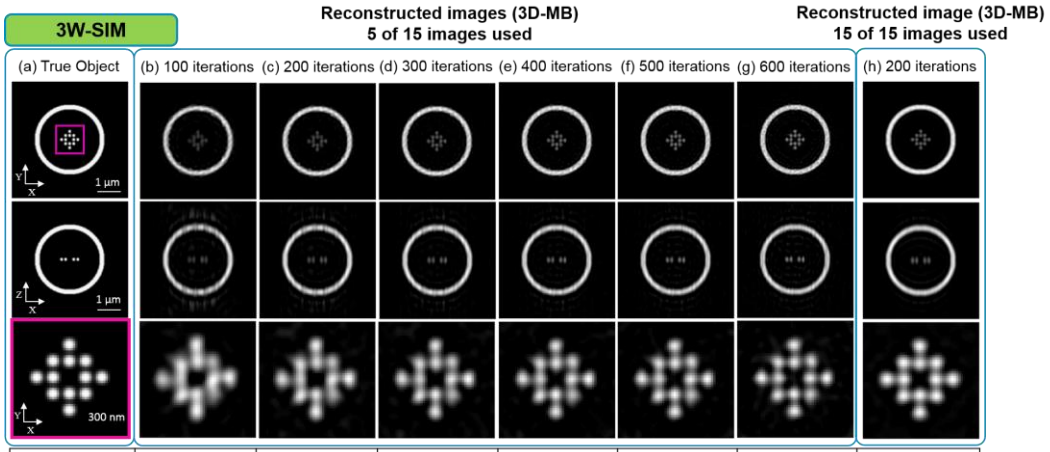

MSE	2.3e-3	1.6e-3	1.4e-3	1.3e-3	1.2e-3	1.4e-3	9.3e-4
SSIM	0.9058	0.9384	0.9471	0.9503	0.9509	0.9440	0.96

Fig. 43. Effect of data reduction (5 out of 15 raw 3W-SIM images used) and number of iterations used on the restoration obtained with the proposed model-based approach (3D-MB) for 3W-SIM using simulated noisy data (SNR = 15dB). Lateral view (top row), axial view (middle row) and zoomed view of the cropped square marked with a pink line in the top left image (bottom row) of the 3D: (a) true object; reconstructed image using 5 out of 15 raw 3W-SIM images with (b) 100 iterations, (c) 200 iterations, (d) 300 iterations, (e) 400 iterations, (f) 500 iterations, (g) 600 iterations and corresponding quantitative comparison using MSE and SSIM. The initial guess set equal to WF image provided by averaging 5 forward SIM images. Reconstructed image using 15 raw 3W-SIM images with 200 iterations (h) and corresponding MSE and SSIM. The initial guess set equal to WF image provided by averaging 15 forward SIM images. For the 3D-SIM system, the lateral modulation frequency was set at $u_m = 0.8u_c = 4.35\ \mu\text{m}^{-1}$ where $u_c = 5.44\ \mu\text{m}^{-1}$. Negative values in the restored images were set to zero. Images are displayed using a different intensity scale mapped to the grayscale to facilitate visualization of details in each image.

The MSE and SSIM of the result obtained with 600 iterations is slightly worse than the one with 500 iterations, which indicates that 500 iterations is enough for this case. For

noisy data, less number of iteration is expected [500 iterations, see Fig. 43(f)] compared to the noiseless data [1000 iterations, see Fig. 40(f)]. The result obtained with 500 iterations [Fig. 43 (f)] is similar to the result obtained without data reduction after 200 iterations [Fig. 43 (h)] qualitatively and quantitatively based on MSE and SSIM metrics reported in Fig. 42Fig. 43. These results indicate that 5 out 15 images can be used for 3D reconstruction for 3W-SIM system in noisy condition as well.

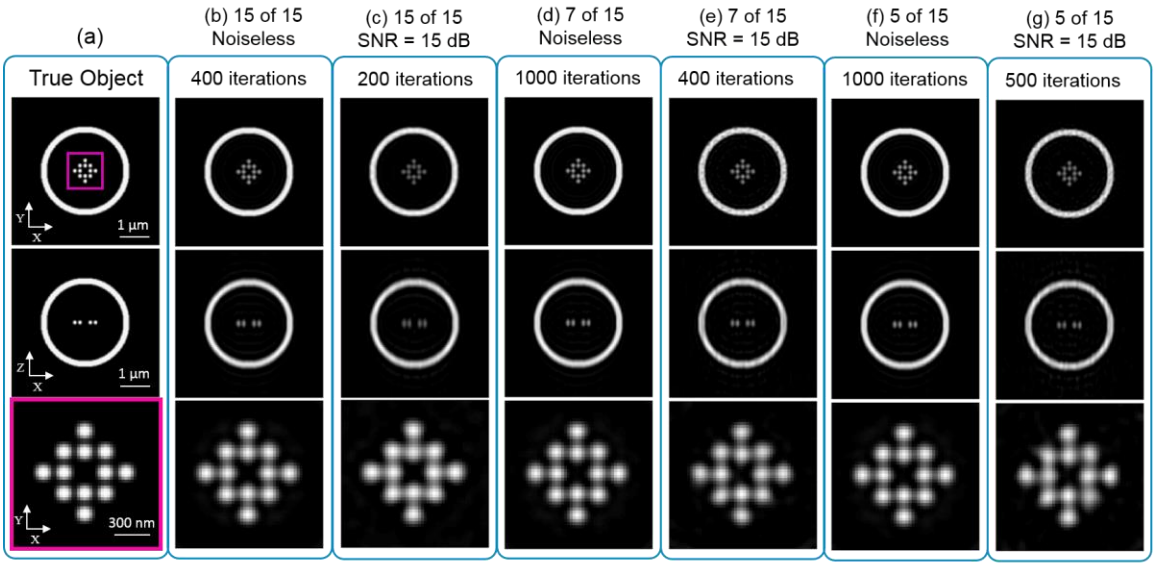

MSE	4.6e-4	9.3e-4	6.5e-4	1.2e-3	6.8e-4	1.2e-3
SSIM	0.98	0.96	0.98	0.95	0.97	0.95

Fig. 44. Effect of data reduction in the presence of noise (SNR = 15 dB) on the restoration obtained with the proposed model-based approach (3D-MB) for 3W-SIM. Lateral view (top row), axial view (middle row) and zoomed view of the cropped square marked with a pink line in the top left image (bottom row) of the 3D: (a) true object; reconstructed image using (b) 15 out of 15 raw 3W-SIM images with 400 iterations for noiseless case, (c) 15 out of 15 raw 3W-SIM images with 200 iterations for SNR = 15 dB case, (d) 7 out of 15 raw 3W-SIM images with 1000 iterations for noiseless case, (e) 7 out of 15 raw 3W-SIM images with 400 iterations for SNR = 15 dB case, (f) 5 out of 15 raw 3W-SIM images with 1000 iterations for noiseless case, (g) 5 out of 15 raw 3W-SIM images with 500 iterations for SNR = 15 dB case and corresponding quantitative comparison using MSE and SSIM. The initial guess set equal to WF image provided by averaging the number of forward SIM images used. For the 3D-SIM system, the lateral modulation frequency was set at $u_m = 0.8u_c = 4.35\ \mu\text{m}^{-1}$ where $u_c = 5.44\ \mu\text{m}^{-1}$. Negative values in the restored images were set to zero. Images are displayed using a different intensity scale mapped to the grayscale to facilitate visualization of details in each image.

The results of 3W-SIM systems including noise effect and data reduction are summarized in Fig. 44, which indicate that data redundancy in 3W-SIM allows reducing the number of forward images used for 3D reconstruction from 15 to 5 in both noiseless and noisy conditions.

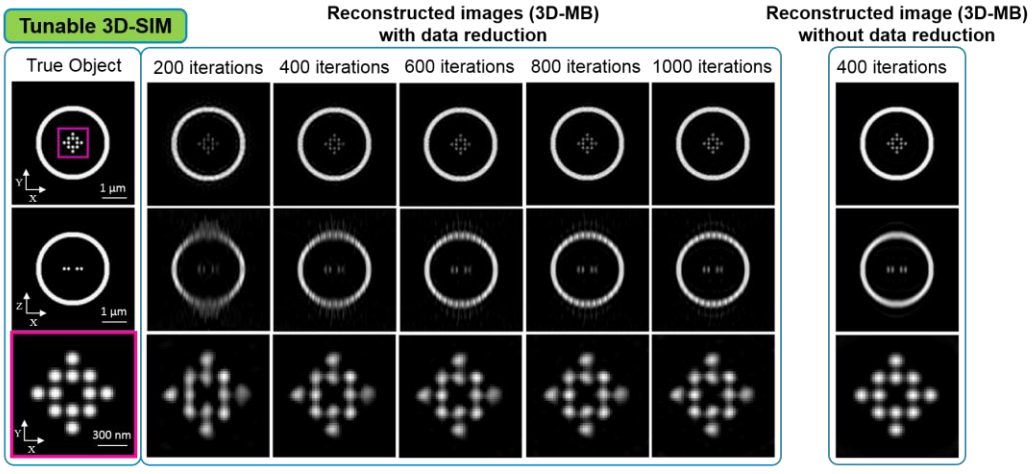

(g)

Number of Iteration	MSE	SSIM
200	3.4e-3	0.85
400	2.2e-3	0.91
600	1.9e-3	0.93
800	1.8e-3	0.93
1000	1.7e-3	0.93

(j)

Number of Iteration	MSE	SSIM
400	5.1e-4	0.98

Fig. 45. Effect of data reduction and number of iterations used on the restoration obtained with the proposed model-based approach (3D-MB) using simulated noiseless data from a tunable 3D-SIM system. Lateral view (top row), axial view (middle row) and zoomed view of the cropped square marked with a pink line in the top left image (bottom row) of the 3D: (a) true object; reconstructed image using 4 out of 9 raw 3W-SIM images with (b) 200 iterations, (c) 400 iterations, (d) 600 iterations, (e) 800 iterations, (f) 1000 iterations. Quantitative comparison using MSE and SSIM (g). Monotonically decreasing cost function [Eq. (8)] (h). The initial guess set equal to WF image provided by averaging 4 forward SIM images. Reconstructed image using 15 raw 3W-SIM images with 400 iterations (i) and corresponding MSE and SSIM (j). The initial guess set equal to WF image provided by averaging 9 forward SIM images. For the 3D-SIM system, the lateral modulation frequency was set at $u_m = 0.8u_c = 4.35\ \mu\text{m}^{-1}$ where $u_c = 5.44\ \mu\text{m}^{-1}$. Negative values in the restored images were set to zero. Images are displayed using a different intensity scale mapped to the grayscale to facilitate visualization of details in each image.

We have also reconstructed the 3D image of a sample from simulated images acquired with the tunable 3D-SIM system by using only 4 (2 images from one orientation and one from each of the other two orientations) out of 9 raw SIM images recorded at each axial plane. The results are shown in Fig. 45 for different number of iterations. The result with data reduction after 1000 iterations [Fig. 45(f)] is still far from the results without data reduction after 400 iterations [Fig. 45(i)] qualitatively and quantitatively based on the MSE and SSIM metrics [Fig. 45(g) and (j)].

We have increased the number of iterations when 4 forward images used in 3D reconstruction in tunable 3D-SIM from 1000 iterations to 2000 and 4000 iterations as shown in Fig. 46(c) and (d), respectively. There is slightly improvement in the restored image as reported by MSE and SSIM values in the table of Fig. 46, however there is still some artifact in the axial view of the restored images visible in middle row of Fig. 46(d). Therefore, it seems that increasing the number of iterations using 4 out of 9 forward images for 3D reconstruction in tunable 3D-SIM system cannot provide the same performance when 9 out of 9 forward images are used. This preliminary result indicates that more than 4 forward images might be needed for 3D reconstruction in the tunable 3D-SIM system. Towards this end, we have increased the number of forward images to 5 (3 images from one orientation and one from each of the other two orientations) and the results are shown in Fig. 46(e) and (f) for 1000 and 2000 number of iterations, respectively. There is slightly improvement in the restored image quantified by the MSE and SSIM values in the table of Fig. 46, however there is still some artifact in the axial view of the restored images visible in the middle row of Fig. 46(f). Investigation of the impact of the illumination design of

the tunable 3D-SIM system used here (i.e., the slit parameters N and x_0) on the observed artifact is suggested as a future work.

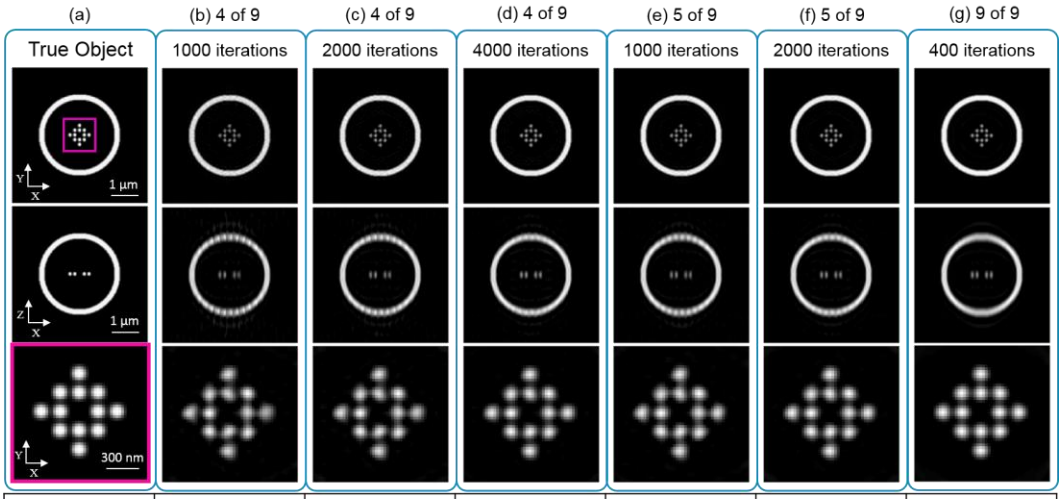

MSE	1.7e-3	1.4e-3	9.8e-4	1.2e-3	1.0e-3	5.1e-4
SSIM	0.93	0.94	0.96	0.95	0.96	0.98

Fig. 46. Effect of data reduction and number of iterations used on the restoration obtained with the proposed model-based approach (3D-MB) using simulated noiseless data from a tunable 3D-SIM system. Lateral view (top row), axial view (middle row) and zoomed view of the cropped square marked with a pink line in the top left image (bottom row) of the 3D: (a) true object; reconstructed image using (b) 4 out of 9 raw tunable 3D-SIM images with 1000 iterations, (c) 4 out of 9 raw 3W-SIM images with 2000 iterations, (d) 4 out of 9 raw 3W-SIM images with 4000 iterations, (e) 5 out of 9 raw 3W-SIM images with 1000 iterations, (f) 5 out of 9 raw 3W-SIM images with 2000 iterations, (g) 9 out of 9 raw 3W-SIM images with 400 iterations and corresponding quantitative comparison using MSE and SSIM. The initial guess set equal to WF image provided by averaging the number of forward SIM images used. For the 3D-SIM system, the lateral modulation frequency was set at $u_m = 0.8u_c = 4.35\ \mu\text{m}^{-1}$ where $u_c = 5.44\ \mu\text{m}^{-1}$. Negative values in the restored images were set to zero. Images are displayed using a different intensity scale mapped to the grayscale to facilitate visualization of details in each image.

5.5. Summary and Conclusion

We have shown proof-of-concept results from noiseless and noisy simulations that confirm the satisfactory performance of the proposed model-based restoration method based on the conjugate gradient decent approach by comparing the restoration with the true

underlying object. It is important to clarify that different noise models and optimization approaches can be used to solve this inverse imaging problem including constraints for regularization. However, the crucial point demonstrated here is the use of the correct imaging model. As expected, any model mismatch in a model-based reconstruction approach can cause artifacts in the restored images. Here we demonstrated that severe artifacts occur even in the case of a relatively thin object when the 3D model used in the restoration does not account for the axial scanning of the sample when processing data acquired from commercial microscopes (which utilize axial scanning). We have also shown a comparison between results from the model-based approach and the standard SIM reconstruction method based on the GWF, when the correct imaging model is used. Overall, the restoration accuracy of the proposed 3D-MB approach outperforms the one of the GWF. Although the 3D-MB iterative method has a longer computation time (one iteration takes as long as the GWF method and time scales linearly with the number of iterations used) it provides the flexibility of including a positivity constraint thereby avoiding unrealistic negative values produced by the GWF. Although the equations for the algorithm based on the positivity constraint were derived, investigation of the method using simulated data is left for future work. Additionally, the model-based framework enables data-acquisition reduction by taking advantage of redundancies in the forward images [70,74] as demonstrated here for two 3D-SIM systems using noiseless simulations and for 3W-SIM systems using noisy simulations and joint estimation of the SI pattern with the corresponding parameters as in the case of blind-SIM restoration [95,98,99].

6. CONCLUSION AND FUTURE DIRECTION

This dissertation presents an effort to investigate the performance of novel approaches employed in 2D-SIM and 3D-SIM systems. Four contributions of the dissertation are: (i) developing an image restoration method for tunable-frequency 2D-SIM to provide simultaneous OS and SR (Chapter 2); (ii) Numerical and experimental verification of the 3D SI patterns, the forward imaging model, and the achieved OS and SR capabilities through the reconstructed images of tunable-frequency 3D-SIM (Chapter 3); (iii) Engineering the design of a tunable 3D-SIM system to operate at the highest OS and SR capabilities based on the synthetic OTF (Chapter 4); and (iv) developing an image restoration method for SIM systems, in which the SI pattern is separable into axial and lateral functions, taking into account the axial scanning of the specimen during the data acquisition as in commercial microscopes (Chapter 5). Detailed discussion and conclusions reached from the investigation studies are included at the end of the respective chapters. This chapter summarizes the highlights of our findings presented in each of the individual chapters, and provides directions for future efforts that may further contribute to the improvement of the efforts presented in this dissertation.

In Chapter 2, a computational method that provides optical-sectioned images with super-resolution (OS-SR algorithm) is developed for a tunable-frequency 2D-SIM, which is implemented using a Fresnel biprism and a single spatially-incoherent linear source in an open setup. A key feature of this setup is that it produces a continuous variation of the pattern's frequency, up to the cutoff frequency of the imaging system. The proposed computational approach can be applied to any tunable-frequency 2D-SIM by recording

phase-shifted images from two independent modulation frequencies. The lower spatial modulation frequency provides OS capability by filling the missing cone and the other one produces SR performance by almost doubling the cutoff frequency of the conventional WF system. These two datasets are properly combined to provide simultaneous OS and SR in the reconstructed image. Although our OS-SR method is based on a 2D-SIM system it provides superior performance over single modulation-frequency 2D-SIM by providing simultaneous OS and SR information, which is the hallmark of 3D-SIM. Moreover, a computational approach is also proposed to reduce the residual fringes evident in the restored images from the Fresnel biprism-based incoherent tunable 2D-SIM system. This method can be applied to any SIM system with non-ideal sinusoidal pattern.

In Chapter 3, a novel tunable-frequency 3D-SIM system, implemented using a Fresnel biprism and multiple spatially-incoherent linear sources in an open setup, has been investigated numerically and experimentally. Forward imaging model is verified experimentally and two reconstruction methods have been used to evaluate the final images. In the investigated studies, the proposed tunable 3D-SIM system is shown to provide an increase in the lateral resolution limit by a factor of 1.8× compared to the native system and improved OS capability by a factor of 1.6× compared to the commercial ApoTome-SIM system. Nonetheless, the main hallmark of the proposed 3D-SIM system is that it requires fewer images for the final restoration than the 3W-SIM (which is the standard 3D-SIM system that has been commercialized by Zeiss in Zeiss Elyra), while the performance of both systems appears to be comparable based on the compact support of the synthetic OTF comparison and numerical results from reconstruction of simulated data.

In Chapter 4, the design of the system parameters in the tunable-frequency 3D-SIM is engineered to make the system operate at the highest axial SR and OS capability. One of the advantage of the implemented tunable-frequency 3D-SIM system in CIRL group is that both lateral and axial periodicity of the 3D pattern can be tuned independently, which is not the case of 3W-SIM system. This unique property allows us to engineer the synthetic OTF of the system for a desired imaging application. This is the first 3D-SIM setup that enables independent control of the achieved OS and SR capabilities. Although it is clear that the highest the u_m, the highest performance in lateral SR, it is verified that one can always design the slit-element, so that the tunable 3D-SIM system operates at the highest axial SR and OS capability. We believe that our system has the potential to have a high impact in biological imaging applications where the highest lateral modulation frequency cannot be used due to a reduction in the SI pattern's contrast. In those cases, our system is expected to enable the possibility to operate with the highest axial SR and OS capabilities even though the lateral SR has been reduced. Further studies with thicker samples and experimental data are needed to demonstrate this system capability.

In Chapter 5, a new 3D iterative model-based deconvolution method based on a model that takes into account the axial scanning of the specimen during the data acquisition as in commercial microscopes is proposed. The method minimizes the mean squared error using conjugate gradient descent. This method is applicable for restoration of data acquired with 2D-SIM and 3D-SIM systems, when the SI pattern is separable into axial and lateral functions. The novel contribution of the proposed approach is its use of the correct imaging model for 3D-SIM. As expected, any model mismatch in a model-based reconstruction approach can cause artifacts in the restored images. We have also shown a comparison

between results from the model-based approach and the standard SIM reconstruction method based on the GWF, when the correct imaging model is used. Overall, the restoration accuracy of the model-based approach outperforms the one of the GWF. Although the model-based iterative approach requires a longer computation time (two orders of magnitude slower than GWF) it provides robustness to noise and the flexibility of applying a positivity constraint thereby avoiding unrealistic negative values.

Additionally, the model-based framework enables joint estimation of the SI pattern and the corresponding parameters and data-acquisition reduction by taking advantage of redundancies in the forward images, which can be considered as future investigations. In Chapter 5, some preliminary results regarding possible data reduction in restoration are shown for both the 3W-SIM and the tunable 3D-SIM systems, which verify that the proposed method can be used with a smaller number of 3D forward images for noiseless and noisy reconstruction; however, more investigation with noisy simulations is needed for tunable 3D-SIM system.

References and Links

1. Max Born and Emil Wolf, *Principles of Optics* (1980).

2. A. Jablonski, "Efficiency of anti-Stokes fluorescence in dyese," Nature **131**(3319), 839 (1933).

3. M. Fernández-Suárez and A. Y. Ting, "Fluorescent probes for super-resolution imaging in living cells," Nat. Rev. Mol. Cell Biol. (2008).

4. L. Schermelleh, R. Heintzmann, and H. Leonhardt, "A guide to super-resolution fluorescence microscopy," J. Cell Biol. **190**(2), 165–175 (2010).

5. E. Betzig, E. Betzig, G. H. Patterson, G. H. Patterson, R. Sougrat, R. Sougrat, O. W. Lindwasser, S. Olenych, S. Olenych, J. S. Bonifacino, J. S. Bonifacino, M. W. Davidson, M. W. Davidson, J. Lippincott-Schwartz, H. F. Hess, and H. F. Hess, "Imaging intracellular fluorescent proteins at nanometer resolution," Science (80-.). **313**(5793), 1642–1645 (2006).

6. S. Hell and E. H. K. Stelzer, "Properties of a 4Pi confocal fluorescence microscope," J. Opt. Soc. Am. A **9**(12), 2159 (1992).

7. H. Gugel, J. Bewersdorf, S. Jakobs, J. Engelhardt, R. Storz, and S. W. Hell, "Cooperative 4Pi Excitation and Detection Yields Sevenfold Sharper Optical Sections in Live-Cell Microscopy," Biophys. J. **87**(6), 4146–4152 (2004).

8. M. J. Rust, M. Bates, and X. Zhuang, "Sub-diffraction-limit imaging by stochastic optical reconstruction microscopy (STORM)," Nat. Methods **3**(10), 793–796

(2006).

9. S. W. Hell and J. Wichmann, "Breaking the diffraction resolution limit by stimulated emission: stimulated-emission-depletion fluorescence microscopy," Opt. Lett. **19**(11), (1994).

10. M. A. A. Neil, R. Juskaitis, and T. Wilson, "Method of obtaining optical sectioning by using structured light in a conventional microscope.," Opt. Lett. **22**(24), 1905–1907 (1997).

11. R. Heintzmann and P. a Benedetti, "High-resolution image reconstruction in fluorescence microscopy with patterned excitation.," Appl. Opt. **45**(20), 5037–5045 (2006).

12. M. G. Gustafsson, "Surpassing the lateral resolution limit by a factor of two using structured illumination microscopy.," J. Microsc. **198**(Pt 2), 82–87 (2000).

13. M. G. L. Gustafsson, "Nonlinear structured-illumination microscopy: wide-field fluorescence imaging with theoretically unlimited resolution.," Proc. Natl. Acad. Sci. U. S. A. **102**(37), 13081–13086 (2005).

14. M. G. L. Gustafsson, L. Shao, P. M. Carlton, C. J. R. Wang, I. N. Golubovskaya, W. Z. Cande, D. A. Agard, and J. W. Sedat, "Three-dimensional resolution doubling in wide-field fluorescence microscopy by structured illumination.," Biophys. J. **94**(12), 4957–4970 (2008).

15. H. Shabani, A. Doblas, G. Saavedra, E. Sanchez-Ortiga, and C. Preza,

"Improvement of two-dimensional structured illumination microscopy with an incoherent illumination pattern of tunable frequency," Appl. Opt. **57**(7), B92 (2018).

16. A. Doblas, H. Shabani, G. Saavedra, and C. Preza, "Tunable-frequency three-dimensional structured illumination microscopy with reduced data-acquisition," Opt. Express **26**(23), 30476–30491 (2018).

17. C. J. R. Sheppard and S. Rehman, "Confocal Microscopy," in *Biomedical Optical Imaging Technologies* (Springer, 2013), pp. 213–231.

18. M. a a Neil, T. Wilson, and R. Juškaitis, "A light efficient optically sectioning microscope," J. Microsc. **189**(2), 114–117 (1998).

19. D. Karadaglić and T. Wilson, "Image formation in structured illumination wide-field fluorescence microscopy," Micron **39**(7), 808–818 (2008).

20. R. Heintzmann and C. G. Cremer, "Laterally modulated excitation microscopy: improvement of resolution by using a diffraction grating," BiOS Eur. **3568**, 185–196 (1999).

21. H. Shabani, A. Doblas, and C. Preza, "Simultaneous optical sectioning and super resolution in 2D-SIM using tunable structured illumination," OSA Tech. Dig. (online), COSI 2017 CW4B–4 (2017).

22. A. Doblas, G. Saavedra, M. Martinez-Corral, J. C. Barreiro, E. Sanchez-Ortiga, and A. Llavador, "Axial resonance of periodic patterns by using a Fresnel

biprism.," J. Opt. Soc. Am. A, **30**(1), 140–8 (2013).

23. M. Martínez-Corral and G. Saavedra, "Progress in Optics," in *The Resolution Challenge in 3D Optical Microscopy* (Elsevier, 2009), **53**, pp. 1–67.

24. T. Fukano and A. Miyawaki, "Whole-field fluorescence microscope with digital micromirror device: imaging of biological samples," Appl. Opt. **42**(19), 4119 (2003).

25. J.-Y. Lin, R.-P. Huang, P.-S. Tsai, and C.-H. Lee, "Wide-field super-resolution optical sectioning microscopy using a single spatial light modulator," J. Opt. A Pure Appl. Opt. **11**(1), 015301–015307 (2009).

26. P. F. Gardeazabal Rodriguez, P. Blandin, I. Maksimovic, E. Sepulveda, E. Muro, B. Dubertret, and V. Loriette, "High-resolution fluorescence microscopy using three-dimensional structured illumination," in *European Conference on Biomedical Optics. Optical Society of America* (2009), **7367**, p. 73670X–7.

27. B.-J. Chang, L.-J. Chou, Y.-C. Chang, and S.-Y. Chiang, "Isotropic image in structured illumination microscopy patterned with a spatial light modulator.," Opt. Express **17**(17), 14710–14721 (2009).

28. L. M. Hirvonen, K. Wicker, O. Mandula, and R. Heintzmann, "Structured illumination microscopy of a living cell.," Eur. Biophys. J. **38**(6), 807–12 (2009).

29. P. Kner, B. B. Chhun, E. R. Griffis, L. Winoto, and M. G. L. Gustafsson, "Super-resolution video microscopy of live cells by structured illumination," Nat. Methods

6(5), 339–342 (2009).

30. B. J. Chang, S. H. Lin, L. J. Chou, and S. Y. Chiang, "Subdiffraction scattered light imaging of gold nanoparticles using structured illumination," Opt. Lett. **36**(24), 4773–4775 (2011).

31. K. O'Holleran and M. Shaw, "Polarization effects on contrast in structured illumination microscopy," Opt. Lett. **37**(22), 4603 (2012).

32. R. Fiolka, L. Shao, E. H. Rego, M. W. Davidson, and M. G. L. Gustafsson, "Time-lapse two-color 3D imaging of live cells with doubled resolution using structured illumination," Natl. Acad. Sci. 5311–5315 (2012).

33. J. Choi and D. Kim, "Enhanced image reconstruction of three-dimensional fluorescent assays by subtractive structured-light illumination microscopy," J. Opt. Soc. Am. A **29**(10), 2165–2173 (2012).

34. H.-C. Huang, B.-J. Chang, L.-J. Chou, and S.-Y. Chiang, "Three-beam interference with circular polarization for structured illumination microscopy," Opt. Express **21**(20), 23963 (2013).

35. H.-W. Lu-Walther, M. Kielhorn, R. Förster, A. Jost, K. Wicker, and R. Heintzmann, "fastSIM: a practical implementation of fast structured illumination microscopy," Methods Appl. Fluoresc. **3**(1), 125005 (2015).

36. D. Lim, K. K. Chu, and J. Mertz, "Wide-field fluorescence sectioning with hybrid speckle and uniform-illumination microscopy," Opt. Lett. **33**(16), 1819–1821

(2008).

37. S. Santos, K. K. Chu, D. Lim, N. Bozinovic, T. N. Ford, C. Hourtoule, A. C. Bartoo, S. K. Singh, and J. Mertz, "Optically sectioned fluorescence endomicroscopy with hybrid-illumination imaging through a flexible fiber bundle," J. Biomed. Opt. **14**(3), 030502-3 (2009).

38. J. Mertz and J. Kim, "Scanning light-sheet microscopy in the whole mouse brain with HiLo background rejection," J. Biomed. Opt. **15**(1), 016027-7 (2010).

39. K. Patorski, M. Trusiak, and T. Tkaczyk, "Optically-sectioned two-shot structured illumination microscopy with Hilbert-Huang processing," Opt. Express **22**(8), 9517–9527 (2014).

40. K. O'Holleran and M. Shaw, "Optimized approaches for optical sectioning and resolution enhancement in 2D structured illumination microscopy," Biomed. Opt. Express **5**(8), 2580–2590 (2014).

41. P. Vermeulen, H. Zhan, F. Orieux, J. C. Olivo-Marin, Z. Lenkei, V. Loriette, and A. Fragola, "Out-of-focus background subtraction for fast structured illumination super-resolution microscopy of optically thick samples," J. Microsc. **259**(3), 257–268 (2015).

42. H. Shabani, A. Doblas, G. Saavedra, and C. Preza, "3D structured illumination microscopy using an incoherent illumination system based on a Fresnel biprism," SPIE BiOS **10499**, 1049903 (2018).

43. H. Shabani, A. Doblas, G. Saavedra, and C. Preza, "Preprocessing method to correct illumination pattern in sinusoidal-based structured illumination microscopy," in *SPIE BiOS* (2018).

44. H. Shabani, N. Patwary, A. Doblas, G. Saavedra, and C. Preza, "Comparison of two structured illumination techniques based on different 3D illumination patterns," SPIE BiOS **10070**, 1007013 (2017).

45. H. Shabani, A. Doblas, G. Saavedra, and C. Preza, "Optical transfer function engineering for a novel structured illumination microscope," Opt. Lett. **in press**, (2019).

46. H. Shabani, E. Sánchez-Ortiga, and C. Preza, "Investigating the performance of reconstruction methods used in structured illumination microscopy as a function of the illumination pattern's modulation frequency," SPIE BiOS **9713**(1), 971305 (2016).

47. H. Shabani, S. Labouesse, A. Sentenac, and C. Preza, "Three-dimensional deconvolution based on axial-scanning model for structured illumination microscopy," 2019 IEEE 16th Int. Symp. Biomed. Imaging **Accepeted**, (2019).

48. F. A. Jenkins and H. E. White, *Fundamental of Optics* (McGraw-Hill, 1957).

49. R. W. Wood, *Physical Optics* (Nabu Press, 2010).

50. E. Sánchez-Ortiga, A. Doblas, G. Saavedra, and M. Martínez-Corral, "Novel proposals in widefield 3D microscopy," Proc. SPIE **7690**, 769005–7 (2010).

51. D. Lim, K. K. Chu, and J. Mertz, "Wide-field fluorescence sectioning with hybrid speckle and uniform-illumination microscopy," Opt. Lett. **33**(16), 1819–1821 (2008).

52. S. Santos, K. K. Chu, D. Lim, N. Bozinovic, T. N. Ford, C. Hourtoule, A. C. Bartoo, S. K. Singh, and J. Mertz, "Optically Sectioned Fluorescence Endomicroscopy with Hybrid-Illumination Imaging through a Flexible Fiber Bundle," Adv. Imaging **14**(June 2009), NWC3 (2009).

53. J. Mertz and J. Kim, "Scanning light-sheet microscopy in the whole mouse brain with HiLo background rejection," J. Biomed. Opt. **15**(1), 016027 (2010).

54. K. Patorski, M. Trusiak, and T. Tkaczyk, "Optically-sectioned two-shot structured illumination microscopy with Hilbert-Huang processing," Opt. Express **22**(8), 9517 (2014).

55. K. O'Holleran and M. Shaw, "Optimized approaches for optical sectioning and resolution enhancement in 2D structured illumination microscopy," Biomed. Opt. Express **5**(8), 2580 (2014).

56. A. Doblas and C. Preza, "Incoherent-based tunable frequency structured illumination microscopy," IS Conf. 2017 OSA Tech. Dig. Ser. (Optical Soc. Am. ITh4 (2017).

57. A. Doblas, H. Shabani, G. Saavedra, and C. Preza, "Comparison of 3D structured patterns with tunable frequency for use in structured illumination microscopy," Proc. SPIE **10070**, 100700H–8 (2017).

58. M. Abramowitz and I. A. Stegun, *Handbook of Mathematical Functions with Formulas, Graphs, and Mathematical Tables* (1972).

59. L. H. Schaefer and D. Schuster, "“Method and device for reconstructing images,” U.S. patent 8,041,142," (2011).

60. N. Patwary, S. V. King, G. Saavedra, and C. Preza, "Reducing effects of aberration in 3D fluorescence imaging using wavefront coding with a radially symmetric phase mask," Opt. Express **24**(12), 12905–12921 (2016).

61. C. J. R. Wang, P. M. Carlton, I. N. Golubovskaya, and W. Z. Cande, "Interlock formation and coiling of meiotic chromosome axes during synapsis," Genetics **183**(3), 905–15 (2009).

62. K. F. Sonnen, L. Schermelleh, H. Leonhardt, and E. A. Nigg, "3D-structured illumination microscopy provides novel insight into architecture of human centrosomes," Biol. Open **1**(10), 965–76 (2012).

63. V. O. Chagin, C. S. Casas-Delucchi, M. Reinhart, L. Schermelleh, Y. Markaki, A. Maiser, J. J. Bolius, A. Bensimon, M. Fillies, P. Domaing, Y. M. Rozanov, H. Leonhardt, and M. C. Cardoso, "4D Visualization of replication foci in mammalian cells corresponding to individual replicons," Nat. Commun. **7**, 11231 (2016).

64. A. C. N. Brown, S. Oddos, I. M. Dobbie, J. M. Alakoskela, R. M. Parton, P. Eissmann, M. A. A. Neil, C. Dunsby, P. M. W. French, I. Davis, and D. M. Davis, "Remodelling of cortical actin where lytic granules dock at Natural Killer cell immune synapses revealed by super-resolution microscopy," PLoS Biol. **9**(9),

e1001152 (2011).

65. V. C. Cogger, G. P. McNerney, T. Nyunt, L. D. DeLeve, P. McCourt, B. Smedsrød, D. G. Le Couteur, and T. R. Huser, "Three-dimensional structured illumination microscopy of liver sinusoidal endothelial cell fenestrations," J. Struct. Biol. **171**(3), 382–8 (2010).

66. V. W. Rowlett and W. Margolin, "3D-SIM Super-resolution of FtsZ and its membrane tethers in Escherichia coli cells," Biophys. J. **107**(8), L17–L20 (2014).

67. C. Lesterlin, G. Ball, L. Schermelleh, and D. J. Sherratt, "RecA bundles mediate homology pairing between distant sisters during DNA break repair," Nature **506**, 249–253 (2014).

68. J. Tilsner, O. Linnik, M. Louveaux, I. M. Roberts, S. N. Chapman, and K. J. Oparka, "Replication and trafficking of a plant virus are coupled at the entrances of plasmodesmata," J. Cell Biol. **201**(7), 981–95 (2013).

69. R. Heintzmann, "Saturated patterned excitation microscopy with two-dimensional excitation patterns," Micron **34**(6–7), 283–291 (2003).

70. F. Orieux, E. Sepulveda, V. Loriette, B. Dubertret, and J. C. Olivo-Marin, "Bayesian estimation for optimized structured illumination microscopy," IEEE Trans. Image Process. **21**(2), 601–614 (2012).

71. S. Dong, J. Liao, K. Guo, L. Bian, J. Suo, and G. Zheng, "Resolution doubling with a reduced number of image acquisitions," **6**(8), 455–460 (2015).

72. J. Boulanger, N. Pustelnik, L. Condat, L. Sengmanivong, and T. Piolot, "Nonsmooth convex optimization for structured illumination microscopy image reconstruction," Inverse Probl. **34**, 095004 (2018).

73. A. Lal, X. Huang, and P. Xi, "A frequency domain reconstruction of SIM image using four raw images," Opt. Heal. Care Biomed. Opt. VII **10024**, 1002411 (2016).

74. F. Orieux, V. Loriette, J.-C. Olivo-Marin, E. Sepulveda, and A. Fragola, "Fast myopic 2D-SIM Super Resolution Microscopy with Joint Modulation Pattern Estimation," Inverse Probl. **33**(12), 1–22 (2017).

75. J. W. Goodman, *Introduction to Fourier Optics* (McGraw-Hill, 1966).

76. G. Saavedra, I. Escobar, R. Martínez-Cuenca, E. Sánchez-Ortiga, and M. Martínez-Corral, "Reduction of spherical-aberration impact in microscopy by wavefront coding," Opt. Express **17**(16), 13810 (2009).

77. M. Bertero, P. Boccacci, G. Desidera, and G. Vicidomini, "Image deblurring with Poisson data: from cells to galaxies," Inverse Probl. **25**(12), 123006 (2009).

78. S. A. Shroff, J. R. Fienup, and D. R. Williams, "Phase-shift estimation in sinusoidally illuminated images for lateral superresolution," J. Opt. Soc. Am. A **26**(2), 413 (2009).

79. N. Patwary, A. Doblas, and C. Preza, "Image restoration approach to address reduced modulation contrast in structured illumination microscopy," Biomed. Opt. Express **9**(4), 1630–1647 (2018).

80. C. Karras, M. Smedh, R. Förster, H. Deschout, and R. Heintzmann, "Successful optimization of reconstruction parameters in structured illumination microscopy – a practical guide," bioRxiv **402115**, 1–13 (2018).

81. E. Hecht, *Optics* (Pearson, 2016).

82. E. G. Paek, J. Y. Choe, T. K. Oh, J. H. Hong, and T. Y. Chang, "Nonmechanical image rotation with an acousto-optic dove prism.," Opt. Lett. **11**, 1195–1997 (1997).

83. L. Matthias F., J. Schaffer, and B. Goetze, "Structure brings clarity: structured illumination microscopy in cell biology," Biotechnol. J. **4**(6), 858–865 (2009).

84. D. Débarre, E. J. Botcherby, M. J. Booth, and T. Wilson, "Adaptive optics for structured illumination microscopy," Opt. Express **16**(13), 9290–9305 (2008).

85. I. Escobar, E. Sanchez-Ortiga, G. Saavedra, and M. Martinez-Corral, "New Analytical Tools for Evaluation of Spherical Aberration in Optical Microscopy," in *Optical Fluorescence Microscopy : From the Spectral to the Nano Dimension* (Springer, 2011), pp. 85–99.

86. O. Mandula, M. Kielhorn, K. Wicker, G. Krampert, I. Kleppe, and R. Heintzmann, "Line scan - structured illumination microscopy super-resolution imaging in thick fluorescent samples," Opt. Express **20**(22), 24167–24174 (2012).

87. N. Hagen, L. Gao, and T. S. Tkaczyk, "Quantitative sectioning and noise analysis for structured illumination microscopy: errata," Opt. Express **20**(5), 5343 (2012).

88. D. L. Snyder, R. L. White, and A. M. Hammoud, "Image recovery from data acquired with a charge-coupled-device camera," J. Opt. Soc. Am. A **10**(5), 1014 (1993).

89. S. Abrahamsson, J. Chen, B. Hajj, S. Stallinga, A. Y. Katsov, J. Wisniewski, G. Mizuguchi, P. Soule, F. Mueller, C. D. Darzacq, X. Darzacq, C. Wu, C. I. Bargmann, D. A. Agard, M. Dahan, and M. G. L. Gustafsson, "Fast multicolor 3D imaging using aberration-corrected multifocus microscopy," Nat. Methods **10**, 60–63 (2013).

90. Q. Ma, B. Khademhosseinieh, E. Huang, H. Qian, and M. A. Bakowski, "Three-dimensional fluorescent microscopy via simultaneous illumination and detection at multiple planes," Sci. Rep. **6**, 31445 (2016).

91. M. Gustafsson, D. a. Agard, and J. W. Sedat, "Doubling the lateral resolution of wide-field fluorescence microscopy using structured illumination," SPIE BiOS **3919**, 141–150 (2000).

92. E. Mudry, K. Belkebir, J. Girard, J. Savatier, E. Le Moal, C. Nicoletti, M. Allain, and A. Sentenac, "Structured illumination microscopy using unknown speckle patterns," Nat. Photonics **6**(5), 312–315 (2012).

93. T. Lukeš, P. Křížek, Z. Švindrych, J. Benda, M. Ovesný, K. Fliegel, M. Klíma, and G. M. Hagen, "Three-dimensional super-resolution structured illumination microscopy with maximum a posteriori probability image estimation," Opt. Express **22**(24), 29805 (2014).

94. J. Boulanger, N. Pustelnik, and L. Condat, "Non-smooth convex optimization for an efficient reconstruction in structured illumination microscopy," 2014 IEEE 11th Int. Symp. Biomed. Imaging **3**(1), 995–998 (2014).

95. A. Jost, E. Tolstik, P. Feldmann, K. Wicker, A. Sentenac, and R. Heintzmann, "Optical Sectioning and High Resolution in Single-Slice Structured Illumination Microscopy by Thick Slice Blind-SIM Reconstruction.," PLoS One **10**(7), e0132174 (2015).

96. N. Chakrova, B. Rieger, and S. Stallinga, "Deconvolution methods for structured illumination microscopy," J. Opt. Soc. Am. A **33**(7), (2016).

97. A. Negash, S. Labouesse, A. Sentenac, H. Giovannini, M. Allain, R. Heintzmann, P. C. Chaumet, and N. Sandeau, "Separate deconvolution : for three-dimensional speckle imaging fluorescence microscopy," Imaging Appl. Opt. 2016 MTh1H.2 (2016).

98. S. Labouesse, A. Negash, P. Liu, A. Sentenac, and M. Allain, "Joint reconstruction strategy for structured illumination microscopy with unknown illuminations," IEEE Trans. Image Process. **26**(5), 2480–2493 (2017).

99. S. Labouesse, A. Negash, J. Idier, S. Bourguignon, and T. Mangeat, "Fast reconstruction in blind fluorescence structured illumination microscopy," Imaging Appl. Opt. MM3C.2 (2017).

100. K. Chu, P. J. McMillan, Z. J. Smith, J. Yin, J. Atkins, P. Goodwin, S. Wachsmann-Hogiu, and S. Lane, "Image reconstruction for structured-illumination microscopy

with low signal level," Opt. Express **22**(7), 8687 (2014).

101. N. Sandeau, R. Heintzmann, K. Wicker, R. Ayuk, H. Giovannini, A. Jost, E. Mudry, J. Girard, T. Mangeat, and N. Sandeau, "Structured illumination fluorescence microscopy with distorted excitations using a filtered blind-SIM algorithm Structured illumination fluorescence microscopy with distorted excitations using a filtered blind-SIM algorithm," (April), (2014).

102. L. Yeh, L. Tian, and L. Waller, "Structured illumination microscopy with unknown patterns and a statistical prior," (2017).

103. E. Soubies and M. Unser, "Computational Super-Sectioning for Single-Slice Structured-Illumination Microscopy," IEEE Trans. Comput. Imaging **PP**(c), 1 (2018).

104. A. Sentenac, K. Belkebir, H. Giovannini, and P. C. Chaumet, "High-resolution total-internal-reflection fluorescence microscopy using periodically nanostructured glass slides," J. Opt. Soc. Am. **26**(12), 2550–2557 (2009).

105. E. Polak and G. Ribiere, "Note sur la convergence de directions conjugu´ee," Rev. Fr. Informat Rech. Oper. **16**, 35–43 (1969).

106. Z. Wang and A. C. Bovik, "Mean squared error: Love it or leave it? A new look at signal fidelity measures," IEEE Signal Process. Mag. **26**(January), 98–117 (2009).

107. L. H. Schaefer, D. Schuster, and J. Schaffer, "Structured illumination microscopy: artifact analysis and reduction utilizing a parameter optimization approach," J.

Microsc. **216**(2), 165–174 (2004).

108. B. M. Hanser, M. G. L. Gustafsson, D. a Agard, and J. W. Sedat, "Phase retrieval for high-numerical-aperture optical systems.," Opt. Lett. **28**(10), 801–803 (2003).

Appendix A: Removing residual fringes in 2D-SIM

This section describes the proposed approach to remove the residual fringes in the restored images for the tunable-frequency 2D-SIM based on the Fresnel biprism, which has been used in chapter 2, in more details with some additional experimental result [43].

From Eq. (7) in Section 2.3 of Chapter 2, it is clear that the SI pattern created by the biprism cannot be described by a pure sinusoidal function as shown in the top panel of Fig. 47(a), because the fringes are distorted by an upper and lower envelopes, which are the effect of three functions described by Eqs. (8)-(10) due to the biprism's edge. To investigate further the effect of the edge, we have studied these three functions in more detail. In Fig. 47(b) and (c), we plot the lateral profile of the two functions, $\mathrm{env}(\boldsymbol{x}, z;\eta)$ and $\vartheta_C(\boldsymbol{x}, z;\eta)$, respectively. One can visualize the high similarity between these two functions by comparing these two figures. In fact, to quantify their similarity we have computed the correlation coefficient and the mean squared error (MSE) value between $\mathrm{env}(\boldsymbol{x}, z;\eta)$ and $\vartheta_C(\boldsymbol{x}, z;\eta)$. These values are equal to 0.99 and 3.4e-2, respectively. Therefore, we can conclude that the two functions can be considered approximately equal i.e., $\mathrm{env}(\boldsymbol{x}, z;\eta) \cong \vartheta_C(\boldsymbol{x}, z;\eta)$. On the other hand, the third term in Eq. (7), $\vartheta_S(\boldsymbol{x}, z;\eta)\sin\left(2\pi a(\eta)x/\lambda f_{L1}\right)$, was found to be negligible as the correlation and MSE between the evaluations of Eq. (7) with and without this term [Fig. 47 (d) and (e)] are equal to 0.99 and 6.4e-2, respectively. Therefore, Eq. (7) can be simplified by the following:

$$I(\boldsymbol{x}, z;\eta) \cong \mathrm{env}(\boldsymbol{x}, z;\eta)\left[1+\cos\left(2\pi\frac{a(\eta)}{\lambda f_{L1}}x\right)\right]. \tag{1A}$$

As shown in bottom panel of Fig. 47(a), which represents the Fourier transform of Eq. (7), the envelope function $\text{env}(\boldsymbol{x}, z; \eta)$ adds some extra frequencies around the modulation frequency of the pattern. Due to the presence of these spatial frequencies, the SI pattern generated by the Fresnel biprism cannot be approximated as a pure sinusoidal. It is important to highlight that if the structured pattern follows a pure sinusoid, then its Fourier transform is represented by three impulse responses in theory. However, Fourier transform of the pure sinusoid shown in bottom panel of Fig. 47(a) has finite width because of the finite size of the pattern.

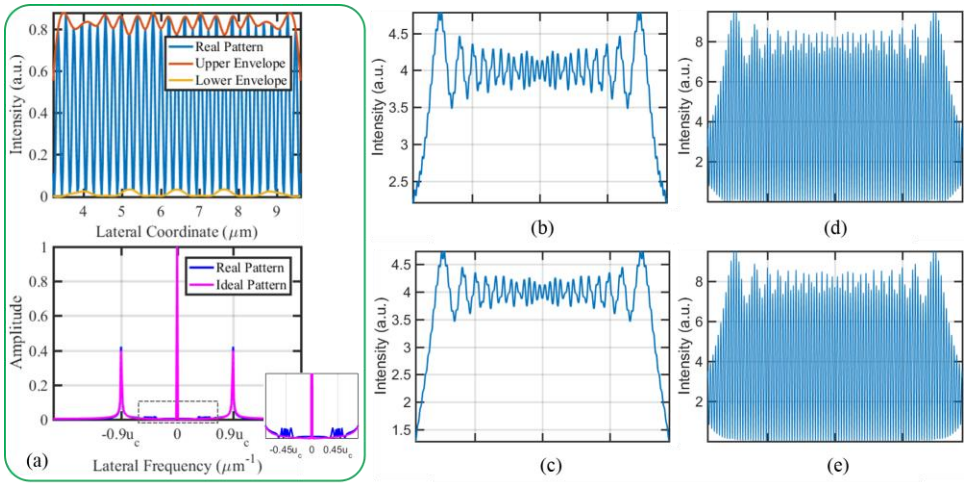

Fig. 47. Illumination pattern generated by the Fresnel biprism for a modulation frequency equal to $u_m = 0.9u_c$: (a) pattern and the corresponding lower and upper envelopes in space domain (top panel), and pattern in the frequency domain compared with the ideal sinusoidal pattern (bottom panel), where the inset shows a zoomed version of the frequency content of the envelopes marked with the dashed rectangle. (b) Lateral profile of the function in Eq. (2); (c) lateral profile of the function in Eq. (3); (d) and (e) Evaluations of Eq. (1) with and without the third term, respectively. The cutoff frequency (u_c) is 5.4 μm^{-1} with the emission wavelength at λ = 515 nm and the imaging lens' numerical aperture (NA) equal to 1.4.

Equations (7) or (1A) show that the SI pattern generated by the biprism using the incoherent tunable-frequency 2D-SIM contains some additional frequencies around the

modulation frequency of the pattern [as shown in Fig. 47(a) for the SI pattern] due to the diffraction effects introduced by the biprism's edge. Because of these frequencies, the SIM pattern cannot be described by a pure sinusoidal [Eq. (1A)] and, therefore, in the reconstruction step [14,44], there would be some mismatch between the SI pattern created by the biprism and the pure sinusoidal model assumed by the restoration method. To visualize this issue, we simulated the effect of these envelopes by comparing the forward and restored images of a 6-μm spherical bead with an ideal (a pure sinusoidal function) and the real [Eq. (7)] SI patterns. It is observable from Fig. 49(b) that there is a residual fringes' pattern in the restored image from the data with the real pattern, as expected. This residual pattern is also shown in the experimental data from the pollen grain in Fig. 50(b).

The proposed approach to reduce the effect of the envelope consists of two parts [see the block diagram in Fig. 48]. First a low-pass filter whose cutoff frequency is equal to 75% of the modulation frequency (u_m) is applied to the background of the raw forward images or to calibration data (such as, the image of a flat layer of fluorescence acquired with the same imaging conditions) to extract the frequency information of the envelopes in the real pattern. Then, the effect of the upper and lower envelopes in the forward SIM images is removed by point-wise dividing each raw image by the computed envelopes. To avoid division by zero we have used a small additive constant in the denominator. The forward images can be restored using the regular SIM reconstruction method proposed by Gustafsson et al. [14]. Second, due to the experimental mismatch in the phase of the SI pattern and unequal intensities in the phase-shifted raw images [107], residual fringes, whose frequencies appear in the vicinity of the modulation frequency, may be visible in

the restored images. Therefore, a designed notch filter, as expressed in Eq. (2A), is applied to the Fourier transform of the restored image to eliminate those frequencies.

$$H_{notch}(u,v) = 1 - \left[e^{-\left[(u-u_m)^2+v^2\right]/2\sigma^2} + e^{-\left[(u+u_m)^2+v^2\right]/2\sigma^2} \right] \tag{2A}$$

where (u,v) are the transverse frequency coordinates, u_m is the modulation frequency, and σ is the standard deviation of the Gaussian function. The value of σ is chosen carefully (i.e. $\sigma \leq 0.05$) so that the object spectrum is minimally affected.

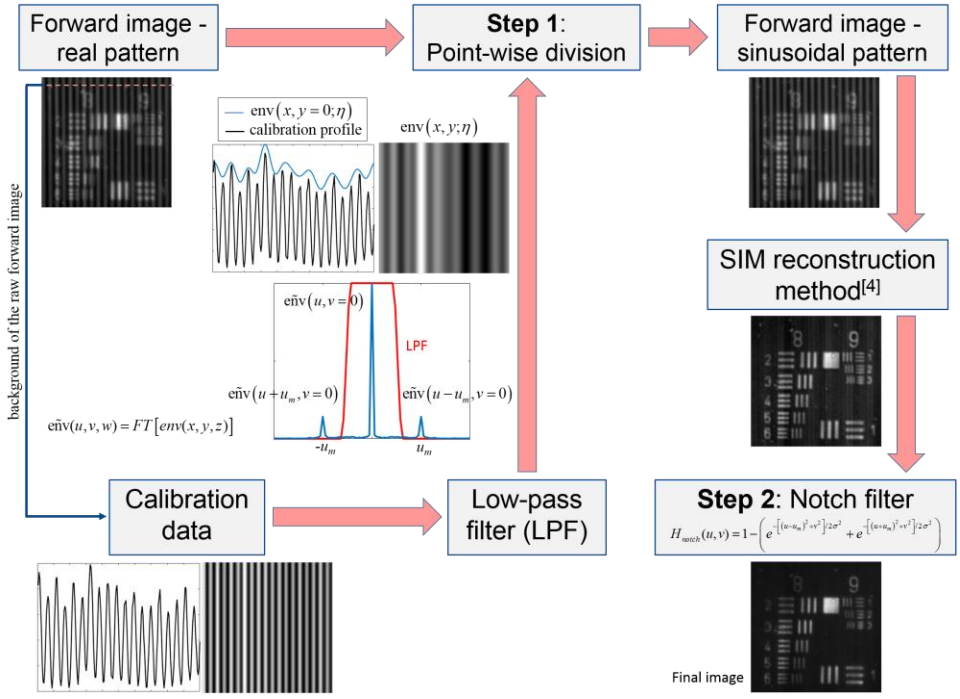

Fig. 48. Block diagram describing the envelope correction method proposed to reduce the residual fringes in tunable SIM based on the Fresnel biprism.

To evaluate the proposed approach, the simulated object of a 6-µm spherical bead and an experimental transverse section from a pollen grain sample (Item #304264, Carolina®, Burlington, North Carolina) have been used. The parameters used for the microscope in the simulation and experiment are: excitation wavelength of λ_{ex} = 488 nm, emission

wavelength at λ_{em} = 515 nm, and imaging lens' numerical aperture, NA = 0.5 (therefore, the cutoff frequency is equal to $u_c = \frac{2\text{NA}}{\lambda} = 1.9\ \mu\text{m}^{-1}$). The objective lens' PSF was calculated based on the Fourier optics formulation [108]. Three forward images corresponding to three different illumination phases were used with modulation frequency equal to $u_m = 0.5u_c$ (in the simulation) and $u_m = 0.1u_c$ and $u_m = 0.3u_c$ (in the experiment).

The simulated result is shown in Fig. 49. The proposed approach is able to reduce the residual pattern as shown in Fig. 49(c). Moreover, Fig. 49(d) shows the normalized intensity profile along the center of the restored bead images in bottom panel of Fig. 49(a) and (b) and Fig. 49(c) for a quantitative comparison and the verification of the envelope correction method. Comparing the profile shows that there is a 74% reduction in the residual pattern, which means that the contrast of the residual fringes is reduced from 0.12 to 0.03 when the proposed method is used.

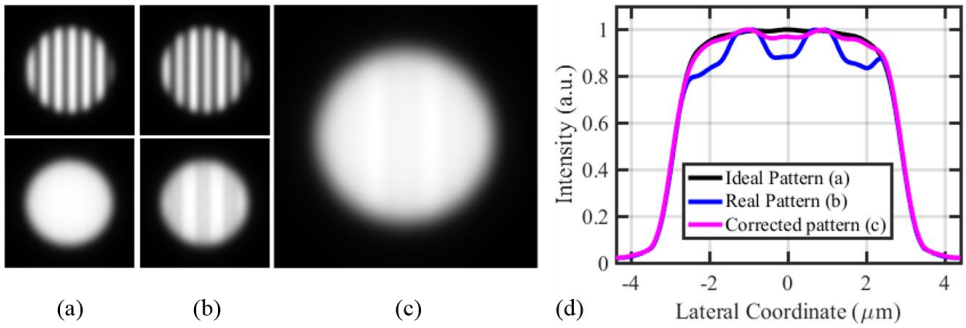

Fig. 49. Qualitative evaluation of the proposed envelope correction method to address the real SI pattern in tunable 2D-SIM based on the Fresnel biprism for simulated object (6-μm spherical bead). Lateral view from the 3D: (a) forward image (top row) and reconstructed image (bottom row) with ideal sinusoidal pattern; (b) forward image with real pattern (top row) and its reconstruction with ideal sinusoidal pattern (bottom row); (c) reconstructed image after envelope correction applied to (b). (d) Quantitative comparison of images restored from ideal and real pattern SIM data assuming an ideal sinusoidal pattern, with and without envelope correction.

The experimental results obtained from the pollen grain are shown in Fig. 50 for two different modulation frequencies ($u_m = 0.1u_c$ and $u_m = 0.3u_c$). The two steps of the proposed approach, described in Fig. 48, are applied sequentially to the experimental data to show the effectiveness of each step. It is clear that the proposed method is able to reduce the residual pattern independent of the modulation frequency with the use of appropriate filter discussed in Section 3 as shown in Fig. 50(d). It is worth to mention that by increasing the modulation frequency from $0.1u_c$ to $0.3u_c$, the optical sectioning capability improves as more information has been added in the missing cone area. Therefore, the out of focus information, affecting the intensities in the center part of the pollen grain is reduced when better optical sectioning is achieved as in the images shown in Fig. 50 (bottom row).

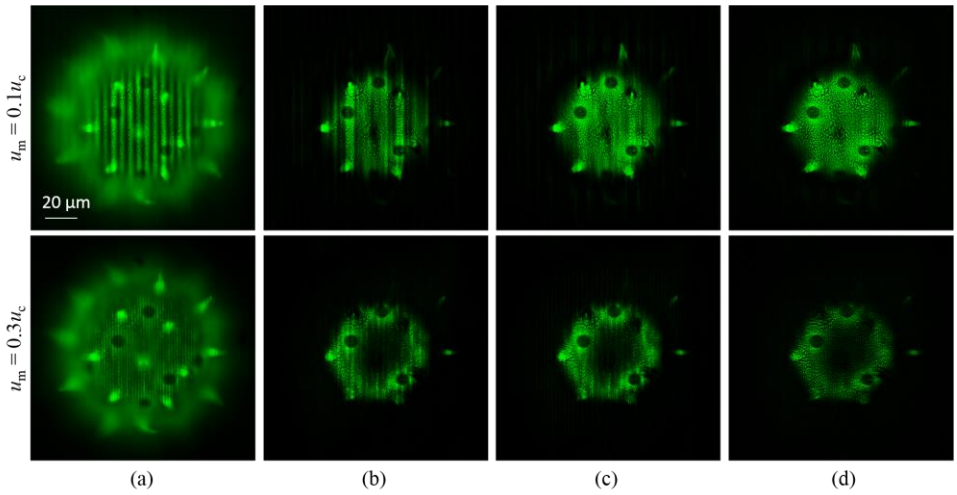

Fig. 50. Qualitative evaluation of the proposed envelope correction method to address the real SI pattern in tunable 2D-SIM based on the Fresnel biprism for the experimental data of a pollen grain for two different modulation frequencies: $u_m = 0.1u_c$ (top row) and $u_m = 0.3u_c$ (bottom row). (a) Raw experimental images with the real SI pattern. Reconstructed images: (b) before envelope correction; (c) after applying the first step of the proposed approach for the envelope correction to (b); (d) after applying the first and second steps of the proposed approach for the envelope correction to (b).

The proposed approach reduces the effect of the envelope of the real pattern (caused by the edge of the Fresnel biprism) on the restoration, and it was shown to reduce residual fringe pattern artifacts in restored images from simulated and experimental data. The simulation result shows a 74% reduction in the residual pattern when the proposed method is used.

Appendix B: Details of noise investigation in synthetic OTF

To study the effect of the noise on the performance of 3D-SIM systems in Chapter 4, we have generated noisy synthetic OTFs as follows:

1. The image of a sub-resolved bead, which represents the WFM point spread function (PSF), was scaled to mimic a specific photon count and it was used to generate noisy image corrupted with Poisson noise.

2. Going to frequency domain by taking the FT of the noisy WF PSF, and then taking the absolute value to generate the noisy WF MTF.

3. Repeat steps 1 and 2 for 100 times and take the average over the 100 realizations of noisy WF MTF.

4. Generating the 3D synthetic OTF for both 3D-SIM systems.

Then, we calculate the effective axial and lateral cutoff frequencies based on the axial and lateral profiles, respectively, as follows and reported in Chapter 4:

a) Measure the threshold (plateau) as the mean value beyond the effective noiseless cutoff frequency.

b) Determine the frequency in the noiseless MTF that its corresponding value is equal to the measured threshold (plateau).

c) Record this frequency as a cutoff frequency.

Moreover, another metric (zeroth order moment) other than the effective lateral and axial cutoff frequencies has been calculated as follows and reported in Fig. 51:

a) Measure the threshold (plateau) as the mean value beyond the effective noiseless cutoff frequency.

b) Subtracting the measured threshold (plateau) from the whole profile and set the negative values equal to zero.

c) Measure the zeroth order moment as the area under the curve of each lateral and axial profile.

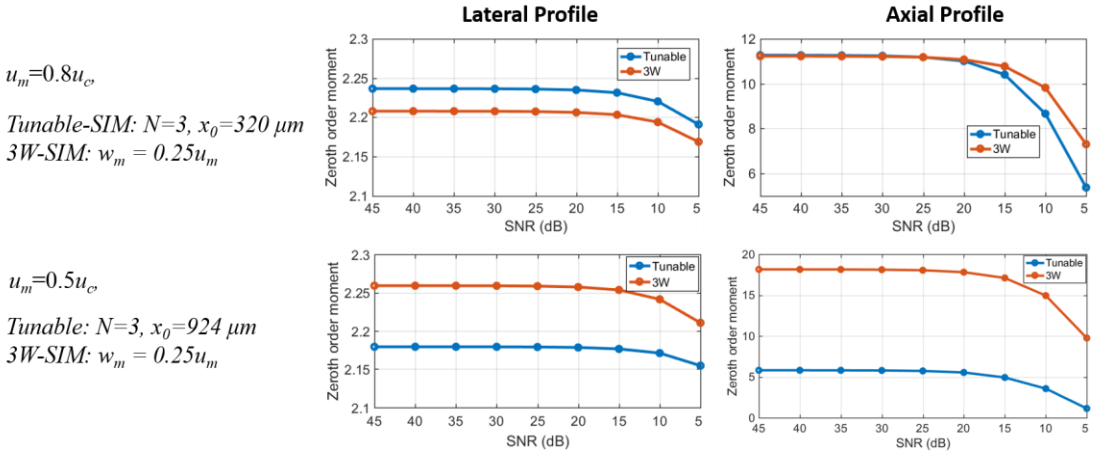

Fig. 51. Zeroth order moment of two 3D-SIM systems under noisy conditions.

Appendix C: Generalized Weiner filter approach in 3D-SIM

The generalized wiener filter (GWF) approach is a non-iterative reconstruction approach based on 4 steps: decomposition, deconvolution, shifting and combination. This method uses the correct imaging model (i.e., a model that takes into account how the data is acquired). To provide a better understanding of GWF approach, we analyze the forward imaging process of 3D-SIM implementation (either the 3W-SIM [14] and tunable 3D-SIM systems [16]) by taking the FT of Eq. (7) in Chapter 5 to obtain:

$$G(\boldsymbol{u},w)=\sum_{k=-\frac{C-1}{2}}^{+\frac{C-1}{2}}\left[O(\boldsymbol{u},w)\otimes_3 J_k(\boldsymbol{u})\right]\left[H(\boldsymbol{u},w)\otimes_3 I_k(w)\right], \tag{C1}$$

where C indicates the number of components, which is equal to 5 and 3 the 3W-SIM [14] and tunable 3D-SIM systems [16], respectively. For 3W-SIM, by taking the FT of Eq. (14) in Chapter 1 (one single orientation has been considered, $\theta=0$, as the process is the same for other orientations),we will have:

$$\begin{aligned} &J_k(u)=1, && I_k(w)=1, && k=0.\\ &J_k(u)=\frac{2}{3}e^{ik\frac{\varphi}{2}}\delta\left(u-k\frac{u_m}{2}\right), && I_k(w)=\delta(w-w_m)+\delta(w+w_m), && k=\pm 1.\\ &J_k(u)=\frac{1}{3}e^{ik\frac{\varphi}{2}}\delta\left(u-k\frac{u_m}{2}\right), && I_k(w)=1, && k=\pm 2. \end{aligned} \tag{C2}$$

And for tunable 3D-SIM we have:

$$\begin{aligned} &J_k(u)=1, && I_k(w)=1, && k=0.\\ &J_k(u)=\frac{1}{2}e^{ik\varphi}\delta(u-ku_m), && I_k(w)=V(w), && k=\pm 1. \end{aligned} \tag{C3}$$

Then, Eq. (C1) for 3W-SIM would change to:

$$G(\boldsymbol{u},w)=D_0(\boldsymbol{u},w)+\frac{2\mathrm{e}^{\mathrm{i}\frac{\varphi}{2}}}{3}D_{+1}(\boldsymbol{u},w)+\frac{2\mathrm{e}^{-\mathrm{i}\frac{\varphi}{2}}}{3}D_{-1}(\boldsymbol{u},w)+\frac{\mathrm{e}^{\mathrm{i}\varphi}}{3}D_{+2}(\boldsymbol{u},w)+\frac{\mathrm{e}^{-\mathrm{i}\varphi}}{3}D_{-2}(\boldsymbol{u},w) \tag{C4}$$

where,

$$D_k(\boldsymbol{u},w)=O(u-k\frac{u_m}{2},v,w)\,H_k(\boldsymbol{u},w),\qquad k=0,\pm1,\pm2. \tag{C5}$$

and,

$$H_k(\boldsymbol{u},w)=\begin{cases}H(\boldsymbol{u},w) & k=0\\ H(\boldsymbol{u},w-w_m)+H(\boldsymbol{u},w+w_m) & k=\pm1\\ H(\boldsymbol{u},w) & k=\pm2\end{cases} \tag{C6}$$

And, Eq. (C1) for tunable 3D-SIM would change to:

$$G(\boldsymbol{u},w)=D_0(\boldsymbol{u},w)+\frac{\mathrm{e}^{\mathrm{i}\varphi}}{2}D_{+1}(\boldsymbol{u},w)+\frac{\mathrm{e}^{-\mathrm{i}\varphi}}{2}D_{-1}(\boldsymbol{u},w) \tag{C7}$$

where,

$$D_k(\boldsymbol{u},w)=O(u-ku_m,v,w)\,H_k(\boldsymbol{u},w),\qquad k=0,\pm1. \tag{C8}$$

and,

$$H_k(\boldsymbol{u},w)=\begin{cases}H(\boldsymbol{u},w) & k=0\\ H(\boldsymbol{u},w)\otimes_3 V(w) & k=\pm1\end{cases} \tag{C9}$$

Therefore, there are 5 and 3 unknown components, $D_k(\boldsymbol{u},w)$, where $k=0,...,\pm\frac{C-1}{2}$, in 3W-SIM and tunable 3D-SIM systems, respectively. By capturing 5 raw images with 5 different phases ($\varphi_1,\varphi_2,\varphi_3,\varphi_4,\varphi_5$) in 3W-SIM, we will have:

$$\begin{bmatrix} G_1(\boldsymbol{u},w) \\ G_2(\boldsymbol{u},w) \\ G_3(\boldsymbol{u},w) \\ G_4(\boldsymbol{u},w) \\ G_5(\boldsymbol{u},w) \end{bmatrix} = \mathbf{M} \begin{bmatrix} D_0(\boldsymbol{u},w) \\ D_{+1}(\boldsymbol{u},w) \\ D_{-1}(\boldsymbol{u},w) \\ D_{+2}(\boldsymbol{u},w) \\ D_{-2}(\boldsymbol{u},w) \end{bmatrix}, \quad \mathbf{M} = \begin{bmatrix} 1 & \frac{2}{3}e^{i\frac{\varphi_1}{2}} & \frac{2}{3}e^{-i\frac{\varphi_1}{2}} & \frac{e^{i\varphi_1}}{3} & \frac{e^{-i\varphi_1}}{3} \\ 1 & \frac{2}{3}e^{i\frac{\varphi_2}{2}} & \frac{2}{3}e^{-i\frac{\varphi_2}{2}} & \frac{e^{i\varphi_2}}{3} & \frac{e^{-i\varphi_2}}{3} \\ 1 & \frac{2}{3}e^{i\frac{\varphi_3}{2}} & \frac{2}{3}e^{-i\frac{\varphi_3}{2}} & \frac{e^{i\varphi_3}}{3} & \frac{e^{-i\varphi_3}}{3} \\ 1 & \frac{2}{3}e^{i\frac{\varphi_4}{2}} & \frac{2}{3}e^{-i\frac{\varphi_4}{2}} & \frac{e^{i\varphi_4}}{3} & \frac{e^{-i\varphi_4}}{3} \\ 1 & \frac{2}{3}e^{i\frac{\varphi_5}{2}} & \frac{2}{3}e^{-i\frac{\varphi_5}{2}} & \frac{e^{i\varphi_5}}{3} & \frac{e^{-i\varphi_5}}{3} \end{bmatrix}. \tag{C10}$$

And by capturing 3 raw images with 3 different phases ($\varphi_1,\varphi_2,\varphi_3$) in tunable 3D-SIM, we will have:

$$\begin{bmatrix} G_1(\boldsymbol{u},w) \\ G_2(\boldsymbol{u},w) \\ G_3(\boldsymbol{u},w) \end{bmatrix} = \mathbf{M} \begin{bmatrix} D_0(\boldsymbol{u},w) \\ D_{+1}(\boldsymbol{u},w) \\ D_{-1}(\boldsymbol{u},w) \end{bmatrix}, \quad \mathbf{M} = \begin{bmatrix} 1 & \frac{1}{2}e^{i\varphi_1} & \frac{1}{2}e^{-i\varphi_1} \\ 1 & \frac{1}{2}e^{i\varphi_2} & \frac{1}{2}e^{-i\varphi_2} \\ 1 & \frac{1}{2}e^{i\varphi_3} & \frac{1}{2}e^{-i\varphi_3} \end{bmatrix}. \tag{C11}$$

Now 4 steps of GWF are as follows:

1. Decomposition of unknown components by matrix inversion method:

$$\begin{bmatrix} D_0(\boldsymbol{u},w) \\ \vdots \\ D_{-k}(\boldsymbol{u},w) \end{bmatrix} = \mathbf{M}^{-1} \begin{bmatrix} G_1(\boldsymbol{u},w) \\ \vdots \\ G_C(\boldsymbol{u},w) \end{bmatrix}. \tag{C12}$$

2. Each decomposed component, $D_k(\boldsymbol{u}, w)$, is separately deconvovd by a generalized Wiener filter as follows for 3W-SIM:

$$\hat{D}_k(\boldsymbol{u}, w) = \frac{D_k(\boldsymbol{u}, w) H_k^*(\boldsymbol{u}, w)}{\sum_{k'} \left| H_{k'}(u + k' \frac{u_m}{2} - k \frac{u_m}{2}, v, w) \right|^2 + \beta^2} A(u - k \frac{u_m}{2}, v, w), \quad k = 0, \pm 1, \pm 2. \tag{C13}$$

And tunable 3D-SIM:

$$\hat{D}_k(\boldsymbol{u}, w) = \frac{D_k(\boldsymbol{u}, w) H_k^*(\boldsymbol{u}, w)}{\sum_{k'} \left| H_{k'}(u + k' u_m - k u_m, v, w) \right|^2 + \beta^2} A(u - k u_m, v, w), \quad k = 0, \pm 1. \tag{C14}$$

3. Each deconvolved component, $\hat{D}_k(\boldsymbol{u}, w)$, is padded with zeros to provide space for shifting information, and then transferred to real space, $\hat{d}_k(\boldsymbol{x}, z)$, and then shifted to the correct location by multiplying by the complex phase (which correspond to shift in the frequency domain)

4. Finally, combing the shifted deconvolved component: for 3W-SIM:

$$\begin{aligned} \hat{O}(\boldsymbol{x}, z) = \hat{d}_0(\boldsymbol{x}, z) + e^{-i2\pi \frac{u_m}{2} x} \hat{d}_{+1}(\boldsymbol{x}, z) + e^{+i2\pi \frac{u_m}{2} x} \hat{d}_{-1}(\boldsymbol{x}, z) \\ + e^{-i2\pi u_m x} \hat{d}_{+2}(\boldsymbol{x}, z) + e^{+i2\pi u_m x} \hat{d}_{-2}(\boldsymbol{x}, z) \end{aligned} \tag{C15}$$

And tunable 3D-SIM:

$$\hat{O}(\boldsymbol{x}, z) = \hat{d}_0(\boldsymbol{x}, z) + e^{-i2\pi u_m x} \hat{d}_{+1}(\boldsymbol{x}, z) + e^{+i2\pi u_m x} \hat{d}_{-1}(\boldsymbol{x}, z) \tag{C16}$$

Appendix D: Mathematical derivation of cost function gradient and gradient decent step used in the proposed method

The gradient of the cost function, Eq. (8), with respect to the density of fluorophores, $o(\boldsymbol{x},z)$:

$$\nabla = \frac{\partial F\left(o\right)}{\partial o} = \frac{\partial \sum_{l=1}^{L} \left\| g_l^{mes}(\boldsymbol{x},z) - g_l(\boldsymbol{x},z) \right\|^2}{\partial o},$$

$$\nabla = -2\sum_{l=1}^{L} \left(g_l^{mes}(\boldsymbol{x},z) - g_l(\boldsymbol{x},z) \right) \frac{\partial g_l(\boldsymbol{x},z)}{\partial o},$$

$$\nabla = -2\sum_{l=1}^{L} \left(g_l^{mes}(\boldsymbol{x},z) - g_l(\boldsymbol{x},z) \right) \frac{\partial \left[\sum_k \left[o\left(\boldsymbol{x},z\right) j_{k;l}\left(\boldsymbol{x}\right) \right] \otimes_3 \left[h\left(\boldsymbol{x},z\right) i_k\left(z\right) \right] \right]}{\partial o},$$

$$\nabla = -2\sum_{l=1}^{L} \sum_k \frac{\partial \left[o\left(\boldsymbol{x},z\right) j_{k;l}\left(\boldsymbol{x}\right) \right]}{\partial o} \left\{ \left[g_l^{mes}(\boldsymbol{x},z) - g_l(\boldsymbol{x},z) \right] \otimes_3 \left[h\left(\boldsymbol{x},z\right) i_k\left(z\right) \right]^* \right\},$$

$$\nabla = -2\sum_{l=1}^{L} \sum_k j_{k;l}\left(\boldsymbol{x}\right) \left\{ \left[g_l^{mes}(\boldsymbol{x},z) - g_l(\boldsymbol{x},z) \right] \otimes_3 \left[h\left(\boldsymbol{x},z\right) i_k\left(z\right) \right]^* \right\}.$$

The scalar step α is determined by taking the gradient of the cost function, Eq. (13), with respect to α:

$$\nabla_\alpha = \frac{\partial f(\alpha)}{\partial \alpha},$$

$$\nabla_\alpha = -2\sum_{l=1}^{L}\left(g_l^{mes}(\boldsymbol{x},z) - g_l(\boldsymbol{x},z)\right)\frac{\partial g_l(\boldsymbol{x},z)}{\partial \alpha},$$

where $$g_l(\boldsymbol{x},z) = \sum_k \left[\left\{o(\boldsymbol{x},z) + \alpha d\right\} j_{k;l}(\boldsymbol{x})\right] \otimes_3 \left[h(\boldsymbol{x},z) i_k(z)\right],$$

$$\nabla_\alpha = -2\sum_{l=1}^{L}\sum_k dj_{k;l}(\boldsymbol{x})\left\{\left(g_l^{mes}(\boldsymbol{x},z) - g_l(\boldsymbol{x},z)\right) \otimes_3 \left[h(\boldsymbol{x},z) i_k(z)\right]^*\right\},$$

$$\nabla_\alpha = -2\sum_{l=1}^{L}\sum_k dj_{k;l}\left\{\left(g_l^{mes} - \sum_k \left[\left\{o + \alpha d\right\} j_{k;l}\right] \otimes_3 \left[hi_k\right]\right) \otimes_3 \left[hi_k\right]^*\right\},$$

$$\nabla_\alpha = -2\sum_{l=1}^{L}\sum_k dj_{k;l}\left\{\left(g_l^{mes} - \sum_k \left[oj_{k;l}\right] \otimes_3 \left[hi_k\right]\right) \otimes_3 \left[hi_k\right]^*\right\},$$

$$+2\sum_{l=1}^{L}\sum_k dj_{k;l}\left\{\left(\sum_k \left[\alpha dj_{k;l}\right] \otimes_3 \left[hi_k\right]\right) \otimes_3 \left[hi_k\right]^*\right\},$$

$$\nabla_\alpha = d\nabla + 2\sum_{l=1}^{L}\sum_k dj_{k;l}\left\{\sum_k \left[\alpha dj_{k;l}\right] \otimes_3 \left[hi_k\right]^2\right\}.$$

Then by solving $\nabla_\alpha = 0$,

$$\alpha = \frac{d\nabla}{d\left(2\sum_{l=1}^{L}\sum_k j_{k;l}\left\{\sum_k \left[dj_{k;l}\right] \otimes_3 \left[hi_k\right]^2\right\}\right)}.$$

The gradient of the cost function, Eq. (8), with respect to the square root of the density of fluorophores, $\xi(\boldsymbol{x},z)$:

$$\nabla_{\xi}=\frac{\partial F\left(\xi^{2}\right)}{\partial\xi}=\frac{\partial\sum_{l=1}^{L}\left\|g_{l}^{mes}(\boldsymbol{x},z)-g_{l}(\boldsymbol{x},z)\right\|^{2}}{\partial\xi}$$

where $\quad g_{l}(\boldsymbol{x},z)=\sum_{k}\left[\xi^{2}(\boldsymbol{x},z)\,j_{k;l}\left(\boldsymbol{x}\right)\right]\otimes_{3}\left[h\left(\boldsymbol{x},z\right)i_{k}\left(z\right)\right],$

$$\nabla_{\xi}=-2\sum_{l=1}^{L}\left[g_{l}^{mes}(\boldsymbol{x},z)-g_{l}(\boldsymbol{x},z)\right]\frac{\partial g_{l}(\boldsymbol{x},z)}{\partial\xi}$$

$$\nabla_{\xi}=-2\sum_{l=1}^{L}\left[g_{l}^{mes}(\boldsymbol{x},z)-g_{l}(\boldsymbol{x},z)\right]\frac{\partial\left[\sum_{k}\left[\xi^{2}\left(\boldsymbol{x},z\right)j_{k;l}\left(\boldsymbol{x}\right)\right]\otimes_{3}\left[h\left(\boldsymbol{x},z\right)i_{k}\left(z\right)\right]\right]}{\partial\xi}$$

$$\nabla_{\xi}=-2\sum_{l=1}^{L}\sum_{k}\frac{\partial\left[\xi^{2}\left(\boldsymbol{x},z\right)j_{k;l}\left(\boldsymbol{x}\right)\right]}{\partial\xi}\left\{\left[g_{l}^{mes}(\boldsymbol{x},z)-g_{l}(\boldsymbol{x},z)\right]\otimes_{3}\left[h\left(\boldsymbol{x},z\right)i_{k}\left(z\right)\right]^{*}\right\}$$

$$\nabla_{\xi}=-4\sum_{l=1}^{L}\sum_{k}\xi\left(\boldsymbol{x},z\right)j_{k;l}\left(\boldsymbol{x}\right)\left\{\left[g_{l}^{mes}(\boldsymbol{x},z)-g_{l}(\boldsymbol{x},z)\right]\otimes_{3}\left[h\left(\boldsymbol{x},z\right)i_{k}\left(z\right)\right]^{*}\right\}$$

The scalar step α when positvity constriant is considered is determined by taking the gradient of the cost function, Eq. (15), with respect to α:

$$\nabla_\alpha = \frac{\partial f(\alpha)}{\partial \alpha},$$

$$\nabla_\alpha = -2\sum_{l=1}^{L}\left[g_l^{mes}(\boldsymbol{x},z) - g_l(\boldsymbol{x},z)\right]\frac{\partial g_l(\boldsymbol{x},z)}{\partial \alpha},$$

where $$g_l(\boldsymbol{x},z) = \sum_k \left[\left[\xi(\boldsymbol{x},z) + \alpha d\right]^2 j_{k;l}(\boldsymbol{x})\right] \otimes_3 \left[h(\boldsymbol{x},z) i_k(z)\right],$$

$$g_l(\boldsymbol{x},z) = \sum_k \left[\xi^2 j_{k;l}(\boldsymbol{x}) + \alpha^2 d^2 j_{k;l}(\boldsymbol{x}) + 2\alpha d\xi j_{k;l}(\boldsymbol{x})\right] \otimes_3 \left[h(\boldsymbol{x},z) i_k(z)\right],$$

$$\nabla_\alpha = -2\sum_{l=1}^{L}\left[g_l^{mes}(\boldsymbol{x},z) - g_l(\boldsymbol{x},z)\right]\frac{\partial\left\{\sum_k \left[\alpha^2 d^2 j_{k;l}(\boldsymbol{x})\right] \otimes_3 \left[h(\boldsymbol{x},z) i_k(z)\right]\right\}}{\partial \alpha}$$

$$-2\sum_{l=1}^{L}\left[g_l^{mes}(\boldsymbol{x},z) - g_l(\boldsymbol{x},z)\right]\frac{\partial\left\{\sum_k \left[2\alpha d\xi j_{k;l}(\boldsymbol{x})\right] \otimes_3 \left[h(\boldsymbol{x},z) i_k(z)\right]\right\}}{\partial \alpha},$$

$$\nabla_\alpha = -2\sum_{l=1}^{L}\sum_k \frac{\partial\left[\alpha^2 d^2 j_{k;l}(\boldsymbol{x})\right]}{\partial \alpha}\left\{\left[g_l^{mes}(\boldsymbol{x},z) - g_l(\boldsymbol{x},z)\right] \otimes_3 \left[h(\boldsymbol{x},z) i_k(z)\right]^*\right\}$$

$$-2\sum_{l=1}^{L}\sum_k \frac{\partial\left[2\alpha d\xi j_{k;l}(\boldsymbol{x})\right]}{\partial \alpha}\left\{\left[g_l^{mes}(\boldsymbol{x},z) - g_l(\boldsymbol{x},z)\right] \otimes_3 \left[h(\boldsymbol{x},z) i_k(z)\right]^*\right\},$$

$$\nabla_\alpha = -4\sum_{l=1}^{L}\sum_k \alpha d^2 j_{k;l}(\boldsymbol{x})\left\{\left[g_l^{mes}(\boldsymbol{x},z) - g_l(\boldsymbol{x},z)\right] \otimes_3 \left[h(\boldsymbol{x},z) i_k(z)\right]^*\right\}$$

$$-4\sum_{l=1}^{L}\sum_k d\xi j_{k;l}(\boldsymbol{x})\left\{\left[g_l^{mes}(\boldsymbol{x},z) - g_l(\boldsymbol{x},z)\right] \otimes_3 \left[h(\boldsymbol{x},z) i_k(z)\right]^*\right\},$$

$$\nabla_{\alpha} = -4\sum_{l=1}^{L}\sum_{k}\alpha d^2 j_{k;l}(\boldsymbol{x})\left\{ g_l^{mes}(\boldsymbol{x},z)\otimes_3\left[h(\boldsymbol{x},z)i_k(z)\right]^* - \sum_{k'}\left[\xi^2(\boldsymbol{x},z)\, j_{k';l}(\boldsymbol{x})\right]\otimes_3\left[h(\boldsymbol{x},z)i_{k'}(z)\right]^2\right\}$$
$$+4\sum_{l=1}^{L}\sum_{k}\alpha d^2 j_{k;l}(\boldsymbol{x})\left\{\sum_{k'}\left[\alpha^2 d^2 j_{k';l}(\boldsymbol{x})\right]\otimes_3\left[h(\boldsymbol{x},z)i_{k'}(z)\right]^2\right\}$$
$$+4\sum_{l=1}^{L}\sum_{k}\alpha d^2 j_{k;l}(\boldsymbol{x})\left\{\sum_{k'}\left[\xi\alpha d j_{k';l}(\boldsymbol{x})\right]\otimes_3\left[h(\boldsymbol{x},z)i_{k'}(z)\right]^2\right\}$$
$$-4\sum_{l=1}^{L}\sum_{k}d\xi\, j_{k;l}(\boldsymbol{x})\left\{ g_l^{mes}(\boldsymbol{x},z)\otimes_3\left[h(\boldsymbol{x},z)i_k(z)\right]^* - \sum_{k'}\left[\xi^2(\boldsymbol{x},z)\, j_{k';l}(\boldsymbol{x})\right]\otimes_3\left[h(\boldsymbol{x},z)i_{k'}(z)\right]^2\right\}$$
$$+4\sum_{l=1}^{L}\sum_{k}d\xi\, j_{k;l}(\boldsymbol{x})\left\{\sum_{k'}\left[\alpha^2 d^2 j_{k';l}(\boldsymbol{x})\right]\otimes_3\left[h(\boldsymbol{x},z)i_{k'}(z)\right]^2\right\}$$
$$+4\sum_{l=1}^{L}\sum_{k}d\xi\, j_{k;l}(\boldsymbol{x})\left\{\sum_{k'}\left[\xi\alpha d j_{k';l}(\boldsymbol{x})\right]\otimes_3\left[h(\boldsymbol{x},z)i_{k'}(z)\right]^2\right\},$$

$$\nabla_{\alpha} = -4\alpha d^2\sum_{l=1}^{L}\sum_{k} j_{k;l}(\boldsymbol{x})\left\{ g_l^{mes}(\boldsymbol{x},z)\otimes_3\left[h(\boldsymbol{x},z)i_k(z)\right]^* - \sum_{k'}\left[\xi^2(\boldsymbol{x},z)\, j_{k';l}(\boldsymbol{x})\right]\otimes_3\left[h(\boldsymbol{x},z)i_{k'}(z)\right]^2\right\}$$
$$+4\alpha^3 d^2\sum_{l=1}^{L}\sum_{k} j_{k;l}(\boldsymbol{x})\left\{\sum_{k'}\left[d^2 j_{k';l}(\boldsymbol{x})\right]\otimes_3\left[h(\boldsymbol{x},z)i_{k'}(z)\right]^2\right\}$$
$$+4\alpha^2 d^2\sum_{l=1}^{L}\sum_{k} j_{k;l}(\boldsymbol{x})\left\{\sum_{k'}\left[\xi d j_{k';l}(\boldsymbol{x})\right]\otimes_3\left[h(\boldsymbol{x},z)i_{k'}(z)\right]^2\right\}$$
$$+d\nabla_{\xi}$$
$$+4\alpha^2 d\xi\sum_{l=1}^{L}\sum_{k} j_{k;l}(\boldsymbol{x})\left\{\sum_{k'}\left[d^2 j_{k';l}(\boldsymbol{x})\right]\otimes_3\left[h(\boldsymbol{x},z)i_{k'}(z)\right]^2\right\}$$
$$+4\alpha d\xi\sum_{l=1}^{L}\sum_{k} j_{k;l}(\boldsymbol{x})\left\{\sum_{k'}\left[\xi d j_{k';l}(\boldsymbol{x})\right]\otimes_3\left[h(\boldsymbol{x},z)i_{k'}(z)\right]^2\right\},$$

By using three auxiliary variables:

$$A = 4\sum_{l=1}^{L}\sum_{k} j_{k;l}(\boldsymbol{x})\left[g_l^{mes}(\boldsymbol{x},z)\otimes_3\left[h(\boldsymbol{x},z)i_k(z)\right]^* - \sum_{k'}\left[\xi^2 j_{k';l}(\boldsymbol{x})\right]\otimes_3\left[h(\boldsymbol{x},z)i_{k'}(z)\right]^2\right],$$
$$B = 4\sum_{l=1}^{L}\sum_{k} j_{k;l}(\boldsymbol{x})\left[\sum_{k'}\left[d_n^2 j_{k';l}(\boldsymbol{x})\right]\otimes_3\left[h(\boldsymbol{x},z)i_{k'}(z)\right]^2\right],$$
$$C = 4\sum_{l=1}^{L}\sum_{k} j_{k;l}(\boldsymbol{x})\left[\sum_{k'}\left[\xi d_n j_{k';l}(\boldsymbol{x})\right]\otimes_3\left[h(\boldsymbol{x},z)i_{k'}(z)\right]^2\right].$$

∇_α would be:

$$\nabla_\alpha = -\alpha d^2 A + \alpha^3 d^2 B + \alpha^2 d^2 C + d\nabla_\xi + \alpha^2 d\xi B + \alpha d\xi C,$$

Then by solving $\nabla_\alpha = 0$, we have a forth order polynomial function with respect to α as follows:

$$\alpha^3 d^2 B + \alpha^2 \left(d^2 C + d\xi B \right) + \alpha \left(-d^2 A + d\xi C \right) + d\nabla_\xi = 0.$$

We minimized this forth order polynomial function with respect to α_n by determining analytically an admissible solution for α_n from the four roots using the *roots* built-in Matlab function.